

**UNCLASSIFIED**

---

---

**AD\_295 831**

*Reproduced  
by the*

**ARMED SERVICES TECHNICAL INFORMATION AGENCY  
ARLINGTON HALL STATION  
ARLINGTON 12, VIRGINIA**



---

---

**UNCLASSIFIED**

NOTICE: When government or other drawings, specifications or other data are used for any purpose other than in connection with a definitely related government procurement operation, the U. S. Government thereby incurs no responsibility, nor any obligation whatsoever; and the fact that the Government may have formulated, furnished, or in any way supplied the said drawings, specifications, or other data is not to be regarded by implication or otherwise as in any manner licensing the holder or any other person or corporation, or conveying any rights or permission to manufacture, use or sell any patented invention that may in any way be related thereto.

295831

CATALOGED BY ASTIA  
AD No.

295 831



**RESEARCH IN FERROMAGNETICS  
ANNUAL REPORT No. 570-A4**

for the period  
September 1, 1961  
to August 31, 1962

Contract  
Nonr-2676(00)  
Nr 048-137

Submitted  
to  
Information System Branch  
Office of Naval Research

by the Research Division  
of

***LFE ELECTRONICS***

A DIVISION OF LABORATORY FOR ELECTRONICS, INC.  
BOSTON 15, MASSACHUSETTS

570-A4

**RESEARCH IN FERROMAGNETICS  
ANNUAL REPORT**

for the period  
September 1, 1961  
to August 31, 1962

Contract  
Nonr -2676(00)  
Nr 048-137

Submitted  
to  
Information System Branch  
Office of Naval Research

by the Research Division  
of

**IFE ELECTRONICS**

a division of

**LABORATORY FOR ELECTRONICS, INC.  
Boston, Massachusetts**

Research in Ferromagnetics  
With Applications to New Storage Devices  
Annual Report No. 570-A4

This is the Fourth Annual Report for ONR Contract Nonr -2676(00), Nr 048-137. The research is being done by the Solid State Electronics Laboratory in the Research Division of LFE Electronics. This ONR Project is part of an integrated research program in Ferromagnetic Thin Films. The total program has LFE as well as Government support.

Personnel:

The ONR Project is under the direction of H. W. Fuller. R. Hornreich was assigned to the ONR Project through the reporting period and is the principal contributor to this report. Contributions were also made by H. Rubinstein, L. R. Lakin, and T. McCormack.

Staff of the Solid State Electronics Laboratory

Harrison W. Fuller, Director, Solid State Electronics Laboratory  
Harvey Rubinstein, Senior Scientist  
Robert F. Adamsky, Senior Physical Chemist  
Abraham Anouchi, Electronic Engineer  
Constance Bailey, Chemical Technician  
Robert L. Berghold, Photographic Technician  
Robert W. Dobbins, Vacuum Technician  
Howland I. Foster, Engineering Assistant  
Steven Gellatly, Machinist  
Richard M. Hornreich, Physicist  
Lynda R. Lakin, Physicist  
Max Lidman, Vacuum Technician  
Thomas L. McCormack, Senior Electronics Engineer  
William Plansky, Physicist  
Kenneth Quimby, Materials Specialist  
Ronald Randlett, Engineering Assistant  
Alan H. Rice, Physicist  
David A. Rigney, Physical Metallurgist  
Andrew F. Sears, Chemist  
Louis C. Segal, Vacuum Technician  
Robert J. Spain, Physicist  
Donald L. Sullivan, Senior Electronics Engineer  
Ronald J. Webber, Technician

## ABSTRACT

The magnetic studies reported herein result from an investigation of the domain wall motion required in a class of devices represented by the single-film, multi-bit storage device. Chapter I is concerned with the velocity of a domain wall in a thin magnetic film. The wall is considered as being driven by a linear current ramp applied to a tapered strip conductor. A macroscopic theory of wall motion is presented in terms of two film parameters, the wall coercive force and the wall mobility. A transient in the wall velocity is shown to exist and its effect on device design is discussed. Experimental data is presented for a range of current ramp rates. Chapter II is concerned with magnetization configurations at edges in thin films. It is a continuation of the results presented in Chapter II of Annual Report 570-A3. A new configuration consisting of a curling magnetization distribution in a tapered edge film is introduced. This configuration is treated theoretically and the results are correlated with those found previously. The chapter concludes with a theoretical prediction of which magnetization configuration is energetically preferred at a film edge as a function of film thickness and edge taper angle. Chapter III deals with the preparation and study of electron microscope specimens. A technique is discussed that allows the direct study of film edges in the electron microscope. This technique involves the stripping of films off glass substrates. In order to do this the substrate must be covered with a soluble compound before film deposition takes place. Preliminary results showing the effect of this technique on film properties are given. Chapter IV describes a modification of the electron microscope to permit the application of controlled magnetic fields to specimens under study. Two coils, each consisting of two turns, are placed at right angles to each other inside the microscope specimen chamber. The coil design is given and the theoretical magnetic field expression is derived. The desired driving current functions are given as is the ultimate design of the power supply. Chapter V discusses the general problem of switching in thin magnetic films when the switching field is oblique to the film's easy direction. A theoretical switching model is proposed that consists of a combination of rotational and sequential switching processes. In terms of basic film and applied field parameters, the model gives the field magnitudes at which various segments of the switching process will occur. Also given are the equilibrium states between the rotational and sequential segments of the switching process. Alternative sequential processes are discussed and the theoretical expectation of each occurring is given. Experimental

data confirming various aspects of the theoretical model is presented. This data is taken using the hysteresis curve tracer and also using powder pattern techniques. The theoretical model provides a basis for the explanation of variations in switching modes from film to film, and gives a key to the relation between these modes and basic film parameters.

## TABLE OF CONTENTS

	Page
<b>CHAPTER 1. VELOCITY OF DOMAIN WALLS IN THIN FILMS</b>	
1.1 Introduction	1-1
1.2 Theory of Domain Wall Velocity	1-1
1.3 Experimental Studies of Domain Wall Motion	1-9
1.4 Conclusions	1-10
Bibliography	1-12
<b>CHAPTER 2. MAGNETIZATION CONFIGURATIONS AT EDGES IN THIN FILMS</b>	
2.1 Introduction	2-1
2.2 The "Tapered Edge Curling" Configuration	2-1
2.3 Summary	2-9
Bibliography	2-11
<b>CHAPTER 3. ELECTRON MICROSCOPE STUDIES</b>	
3.1 Introduction	3-1
3.2 Preparation of Films for Electron Microscope	3-1
3.3 Micrographs of Film Edges	3-7
3.4 Conclusions	3-13
Bibliography	3-14
<b>CHAPTER 4. MAGNETIC FIELD APPARATUS FOR ELECTRON MICROSCOPE</b>	
4.1 Introduction	4-1
4.2 Field Generating Coils	4-1
4.2.1 Theory of Coil Design	4-1
4.2.2 Description of Coils and Assembly	4-4
4.3 Current Supply for Field Generating Coils	4-9
4.3.1 Specifications	4-9
4.3.2 Circuit Design	4-9
4.3.3 Circuit Operation	4-12
4.4 Conclusions	4-12
Bibliography	4-14

## CHAPTER 5. PARTIAL SWITCHING IN THIN FILMS

5.1	Introduction	5-1
5.2	Theoretical	5-1
5.2.1	Rotational Model	5-1
5.2.2	Modification of Rotational Model	5-6
5.2.3	Demagnetizing Field Calculations	5-8
5.2.3.1	Infinite Sheet of Charge	5-10
5.2.3.2	Lines of Charge	5-10
5.2.4	Calculation of Energy of Partially Switched Configuration	5-13
5.2.4.1	Basic Relations	5-13
5.2.4.2	Wall Energy Calculations	5-13
5.2.4.3	Anisotropy Energy Calculations	5-15
5.2.4.4	Demagnetizing Energy Calculations	5-15
5.2.4.5	Switching Field Energy Calculations	5-16
5.2.4.6	Summation of Energy Terms	5-16
5.2.5	Deduction of Parameters from Partial Switching Model	5-17
5.2.5.1	Calculation of Equilibrium Magnetization Angles	
5.2.5.2	Calculation of Rotational Field Necessary to Switch $\phi_2$ State	
5.2.6	The Sequential Switching Process	
5.3	Experimental	
5.3.1	Analysis of Switching Signal Data	
5.3.2	Analysis of Bitter Patterns	
5.4	Conclusions	
	Appendix	
	Bibliography	

## List of Illustrations

<u>Chapter 1</u>		<u>Page</u>
1-1a	Film Location on Tapered Conducting Strip.	1-2
1-1b	Current Ramp Input Signal.	1-2
1-2	Wall Position-Time Ratio, $x/t$ , vs. Time	1-5
1-3	Wall Velocity vs. Time.	1-6
1-4a	Current Input Signal for Domain Storage, Writing Operation.	1-8
1-4b	Idealized Domain Storage Geometry.	1-8
1-5	Wall Velocity vs. Ramp Rate.	1-11
 <u>Chapter 2</u>		
2-1	The "Abrupt Edge" Configuration.	2-2
2-2	The "Tapered Edge" Configuration.	2-2
2-3	The 90° "Curling" Configuration.	2-3
2-4	The "Closure Domain" Configuration.	2-3
2-5	Possible "Tapered Edge Curling" Configuration.	2-4
2-6	Possible "Tapered Edge Curling" Configuration.	2-4
2-7	Normalized Energies of Various Edge Configurations vs. Film Thickness.	2-8
2-8	Theoretically Expected Edge Configuration as a Function of Film Thickness and Edge Taper Angle.	2-10
 <u>Chapter 3</u>		
3-1	Domain Walls Extending Beyond Apparent Film Edge.	3-2
3-2	Domain Walls Extending Beyond Apparent Film Edge.	3-3

3-3	Modified Deposition System for Victawet Undercoating Studies.	3-5
3-4	Resistance Heated Tungsten Boat used for Victawet Evaporation.	3-6
3-5a	Mask Position During Victawet Evaporation.	3-9
3-5b	Mask Position During Magnetic Film Evaporation.	3-10
3-6a	Switching Signal of Victawet Undercoated Film - Easy Axis Switching.	3-11
3-6b	Switching Signal of Victawet Undercoated Film - Hard Axis Switching.	3-11
3-7	Electron Micrograph of Film Segment Floated off Victawet-Coated Substrate.	3-12

#### Chapter 4

4-1	Cross-Section Geometry of Field-Generating Coil.	4-2
4-2a	Mechanical Drawing of Half of Coil Form.	4-5
4-2b	Mechanical Drawing of Half of Coil Form.	4-6
4-3	Segments of Bakelite Coil Form - Unassembled.	4-7
4-4	Assembled Coil Form.	4-8
4-5	Schematic Diagram of Current Supply for Field-Generating Coils.	4-10
4-6a	Dual Amplifier Output - Circular Erase Mode.	4-13
4-6b	Dual Amplifier Output - Circular Erase Mode.	4-13

## Chapter 5

5-1	Idealized Rotational-Sequential Hysteresis Loop.	5-2
5-2	The Partially Switched State.	5-2
5-3	Sequential Switching of Partially Switched State by Motion of Partial Switching Walls.	5-3
5-4	Sequential Switching of Partially Switched State by Easy Direction Wall Motion.	5-3
5-5	The Rotational Model.	5-5
5-6	Idealized Variation of the Direction of the Easy Axis.	5-5
5-7	Magnitude of Rotation Switching Field as a Function of the Angle Between the Field and the Local Easy Axis.	5-7
5-8	Demagnetizing Field Model.	5-9
5-9a	Model for Calculation of Field of Infinite Sheet of Charge.	5-11
5-9b	Model for Calculation of Field of Infinite Alternately Charged, Lines of Charge.	5-11
5-10	Model of Partially Switched Configuration.	5-14
5-11	Possible Equilibrium Values of the Magnetization Angles, $\phi_1$ and $\phi_2$ .	5-22
5-12	Partially Switched Wall Angle, $\psi$ , vs. Applied Field Angle, $\theta$ Also $(\psi - \theta)$ vs. $\theta$ .	5-25
5-13	Theoretical Wall Motion Coercive Forces of Partially Switched and Easy Direction Wall vs. Applied Field Angle.	5-27
5-14	Switching Signal Output of Specimen for Various Applied Field Angles.	5-29

5-15	Switching Signal Output of Specimen for Various Applied Field Angles .	5-30
5-16	Switching Signal Output of Specimen for Various Applied Field Angles .	5-31
5-17	Switching Signal Output of Specimen for Various Applied Field Angles .	5-32
5-18	Example of the Partially Switched State, Dark Field Illumination .	5-35
5-19	Example of Motion of Paired Partially Switched Walls, Dark Field Illumination .	5-36
5-20	Example of Motion of Paired Partially Switched Walls, Phase Contrast Illumination .	5-37
5-21	Example of Easy Direction Wall Motion, Dark Field Illumination .	5-38
5-22	Model for Calculation of Field of Infinite, Alternately Charged, Paired Lines of Charge .	

# 1. VELOCITY OF DOMAIN WALLS IN THIN FILMS

## 1.1 Introduction

Many properties of thin magnetic films may be studied by observing domain walls in motion. In conducting such a study, it is useful to have a theoretical basis for relating the wall velocity to the film and applied-field parameters. On a microscopic basis, such a theory would deal with: the structure of a moving wall, the eddy currents produced by the wall motion, the effect of imperfections on the local magnetization distribution, etc. This type of theory would be exceedingly difficult to construct.

In this chapter, a macroscopic theory of wall motion will be presented. Interactions between a domain wall and the rest of the film will be taken into account by using two lumped parameters, the wall coercive force and the wall mobility.

The transient and steady-state solutions of the resulting differential equation will be given and their effect on device design discussed. Experimental evidence supporting the steady-state solution will be shown. From such data the coercive force and mobility constants may be determined.

## 1.2 Theory of Domain Wall Velocity

In designing a device utilizing domain wall motion it is important to know the relation between the wall velocity and the wall driving function. The usual method of moving a domain wall is to apply a linear current ramp to a tapered strip<sup>(1)</sup>. For this case, the velocity  $V_w$  of a domain wall is given by<sup>(2)</sup>

$$V_w = \frac{dx}{dt} = R \left( \frac{\alpha \gamma t}{x} - H_C \right), \quad (1-1)$$

where  $R$  is the wall mobility constant,  $\alpha$  is a function of the taper angle of the conducting strip,<sup>(3)</sup>  $\gamma$  is the current ramp rate, and  $H_C$  is the wall coercive force. As shown in Fig. 1-1,  $x$  is the distance from the wall to the taper apex and the time  $t$  is measured from the start of the current ramp.

Setting  $u = x/t$ , Eq. 1-1 becomes

$$\frac{dt}{t} = \frac{-u \, du}{u^2 + H_C R u - R \alpha \gamma} \quad (1-2)$$

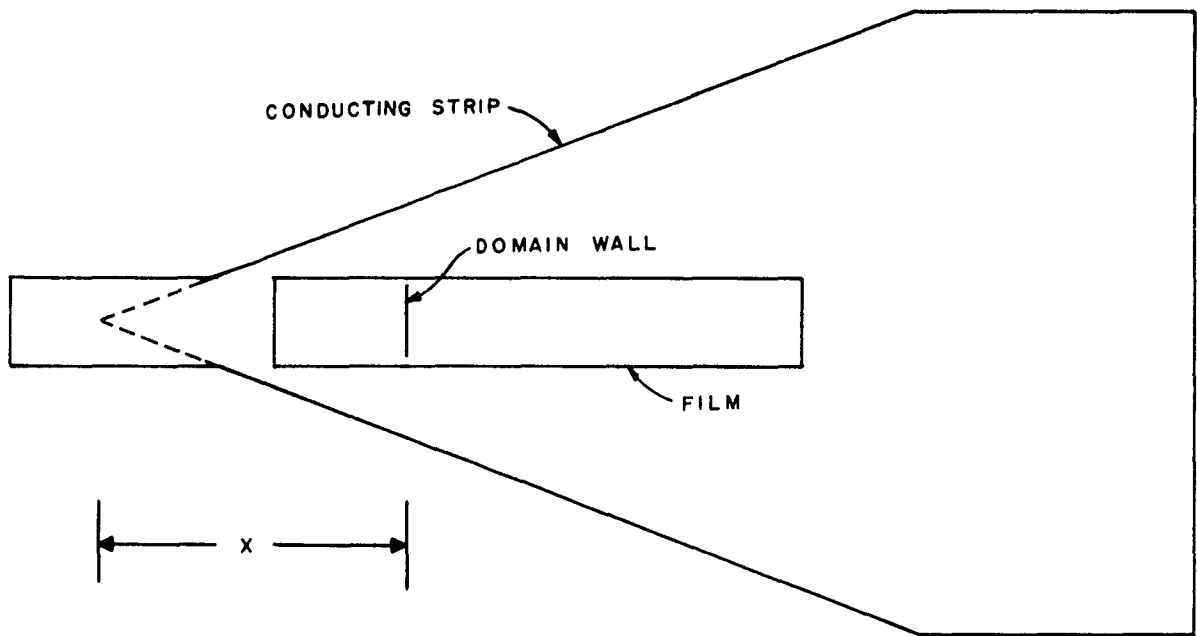


Figure 1-la. Film Location on Tapered Conducting Strip.

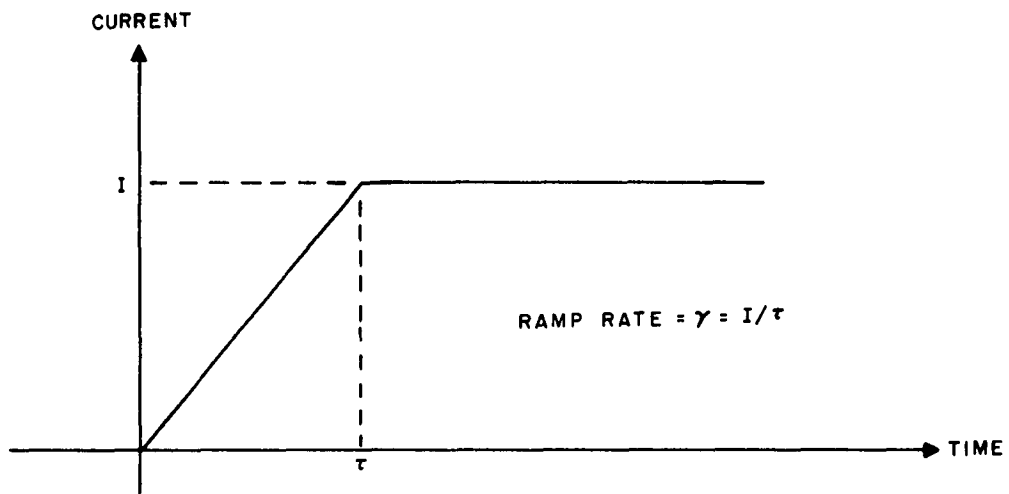


Figure 1-lb. Current Ramp Input Signal.

Integration of Eq. 1-2 yields

$$t [u^2 + H_c R u - R \alpha \gamma]^{1/2} = C \left[ \frac{2u + H_c R - \sqrt{4R\alpha\gamma + H_c^2 R^2}}{2u + H_c R + \sqrt{4R\alpha\gamma + H_c^2 R^2}} \right]^a \quad (1-3a)$$

$$\text{where } a = \frac{H_c R}{2 \sqrt{4R\alpha\gamma + H_c^2 R^2}} \quad (1-3b)$$

and C is the constant of integration.

Equation 1-1 may be solved for u, giving

$$u = \frac{R\alpha\gamma}{V_w + H_c R} \quad (1-4)$$

Substituting Eq. 1-4 into Eq. 1-3 yields  $V_w$  as an implicit function of time:

$$t \left[ \frac{R^2 \alpha^2 \gamma^2}{(V_w + H_c R)^2} + \frac{H_c R^2 \alpha \gamma}{(V_w + H_c R)} - R \alpha \gamma \right]^{1/2} = C \left[ \frac{2R\alpha\gamma/(V_w + H_c R) + H_c R - \sqrt{4R\alpha\gamma + H_c^2 R^2}}{2R\alpha\gamma/(V_w + H_c R) + H_c R + \sqrt{4R\alpha\gamma + H_c^2 R^2}} \right]^a \quad (1-5)$$

The steady-state solution of Eq. 1-1 is easily found by setting  $V_w = u$  in Eq. 1-4 and solving. This yields

$$(V_w)_{s.s} = \frac{1}{2} (\sqrt{4R\alpha\gamma + H_c^2 R^2} - H_c R) \quad (1-6)$$

Assuming a domain wall initially at rest at  $t = 0$  at a position  $x = x_0$ , it is of interest to find the transient involved before the wall velocity reaches its steady-state value. To obtain a representative transient curve, the following values will be used:

$$\text{Taper angle} = 30^\circ \text{ or } \alpha = 1.2 \frac{\text{oe. - cm}}{\text{amp.}},$$

$$\text{Ramp rate } \gamma = 10^4 \frac{\text{amp}}{\text{sec}},$$

$$\text{Coercive force } H_c = 1.5 \text{ oe},$$

$$\text{Wall mobility } R = \frac{1}{3} \times 10^5 \frac{\text{cm}}{\text{sec - oe}}.$$

Introducing these parameter values into Eq. 1-6 yields

$$(V_w)_{s.s.} = u(t = \infty) = u_{\infty} = 7 \times 10^3 \text{ cm/sec.} \quad (1-7)$$

Due to the non-zero coercive force the domain wall remains at  $x = x_0$  until some time  $t = t_0$  is reached. Thus

$$V_w(t = t_0) = 0. \quad (1-8)$$

Letting  $u_0 = x_0/t_0$  and substituting Eq. 1-8 into Eq. 1-1 yields

$$u_0 = \alpha \gamma / H_c = 8 \times 10^3 \text{ cm/sec.} \quad (1-9)$$

It is apparent that as  $t$  goes from  $t_0$  to infinity,  $u$  goes from  $8 \times 10^3$  to  $7 \times 10^3$  cm/sec.

Equation 1-3 may be simplified by calculating the following quantities. Setting

$$a = \frac{H_c R}{2\sqrt{4R\alpha\gamma + H_c^2 R^2}} = 0.39, \quad (1-10)$$

$$u_1 = \frac{1}{2} (\sqrt{4R\alpha\gamma + H_c^2 R^2} - H_c R) = 7 \times 10^3 \text{ cm/sec.}, \quad (1-11)$$

and

$$u_2 = \frac{1}{2} (\sqrt{4R\alpha\gamma + H_c^2 R^2} + H_c R) = 57 \times 10^3 \text{ cm/sec.} \quad (1-12)$$

Equation 1-3 may be rewritten in the form

$$[u - u_1]^{\frac{1}{2} - a} [u - u_2]^{\frac{1}{2} + a} = C/t. \quad (1-13)$$

Setting  $u = u_0$  at  $t = t_0$  in Eq. 1-13 yields

$$C = (41 \times 10^3) t_0 = (5.1) x_0. \quad (1-14)$$

The curve of  $V_w$  versus time can now be determined. It is easiest to do this in two steps. First, using Eq. 1-13,  $t$  may be found for various values of  $u$  between  $8 \times 10^3$  and  $7 \times 10^3$  cm/sec. The resulting curve is shown in Fig. 1-2. Now, using Eq. 1-4,  $V_w$  may be found as a function of  $u$  and, by using Fig. 1-2, as a function of  $t$ . The result is shown in Fig. 1-3.

Figure 1-2 shows clearly that a domain wall subjected to a drive field increasing linearly with time will not reach its steady-state velocity

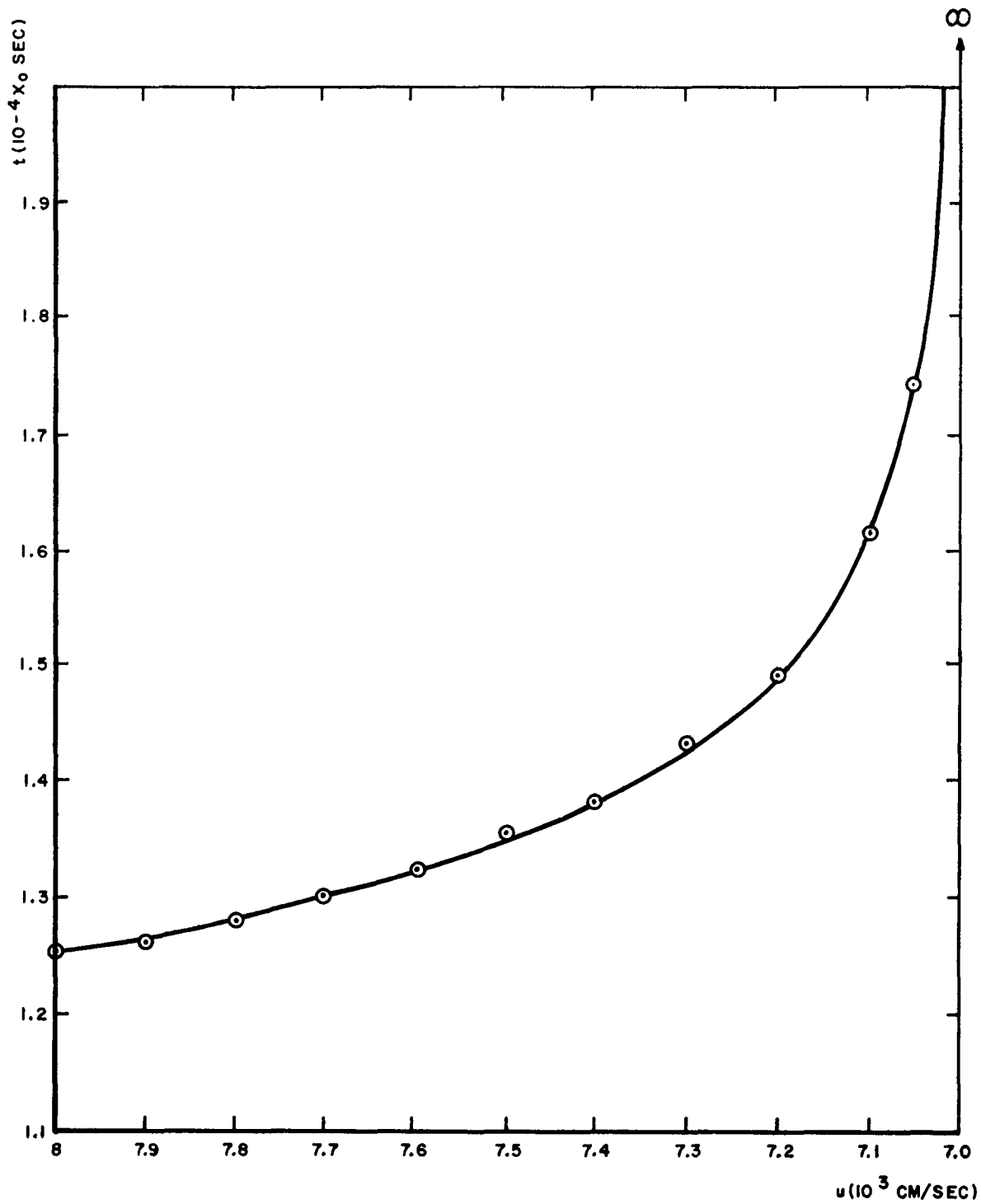


Figure 1-2. Wall Position-Time Ratio,  $x/t$ , vs. Time.

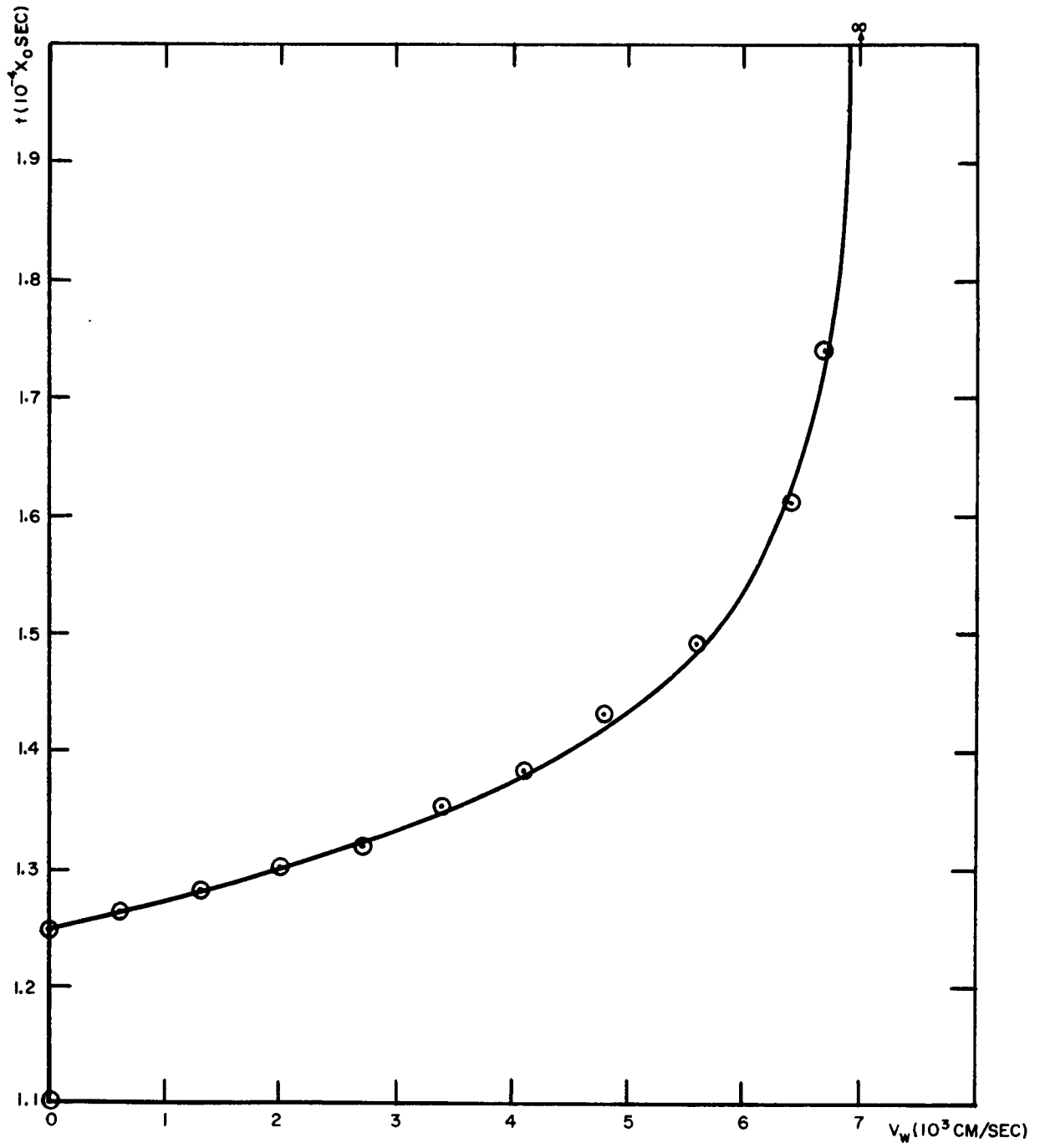


Figure 1-3. Wall Velocity vs. Time.

instantaneously. Perhaps more important from a device viewpoint, the time constant of the transient depends on the initial position of the wall. Physically, this means that the ramp duration necessary to move a wall a given distance depends on the initial position of the wall. This is due to the fact that a wall must absorb energy from the ramp field in order to move. The rate at which the wall can absorb this energy depends on the field gradient in which it rests. For a linearly tapered current strip, this gradient is non-uniform. Thus velocity transient time is a function of initial wall position.

The problem is complicated by the fact that stopping a moving wall also involves some transient time. This renders more complex the distance-pulse duration relation.

The usual signal used to place domain walls is shown in Fig. 1-4a. A simple analysis based on an instantaneous steady-state wall velocity would yield the equally spaced domain wall pattern of Fig. 1-4b. The result in Fig. 1-4b, however, should be modified in accordance with the transient analysis presented here. If the wall storage density is high enough, a logic element expecting to read output pulses that are all strictly an integral multiple of some fundamental time unit might not be able to unambiguously readout every output pulse for an actual non-uniform domain wall spacing. This point must be considered and can be taken into account when considered devices utilizing domain wall information storage.

The assumptions implicit in taking Eq. 1-1 as the wall velocity equation may be tested by measuring the steady-state wall velocity ( $V_w$ ) s.s., as given in Eq. 1-6, as a function of  $\gamma$ , the current ramp rate. For high and low values of  $\gamma$ , Eq. 1-6 can be resolved into two asymptotic forms. These are

$$(a) \quad \gamma \gg H_c^2 R/4\alpha; (V_w)_a = (\alpha R)^{\frac{1}{2}} \gamma^{\frac{1}{2}}, \quad (1-15a)$$

$$(b) \quad \gamma \ll H_c^2 R/4\alpha; (V_w)_b = (\alpha/H_c) \gamma. \quad (1-15b)$$

By using these asymptotic equations with appropriate parameters, experimental values of domain wall velocity as a function of current ramp rate may be compared with theory.

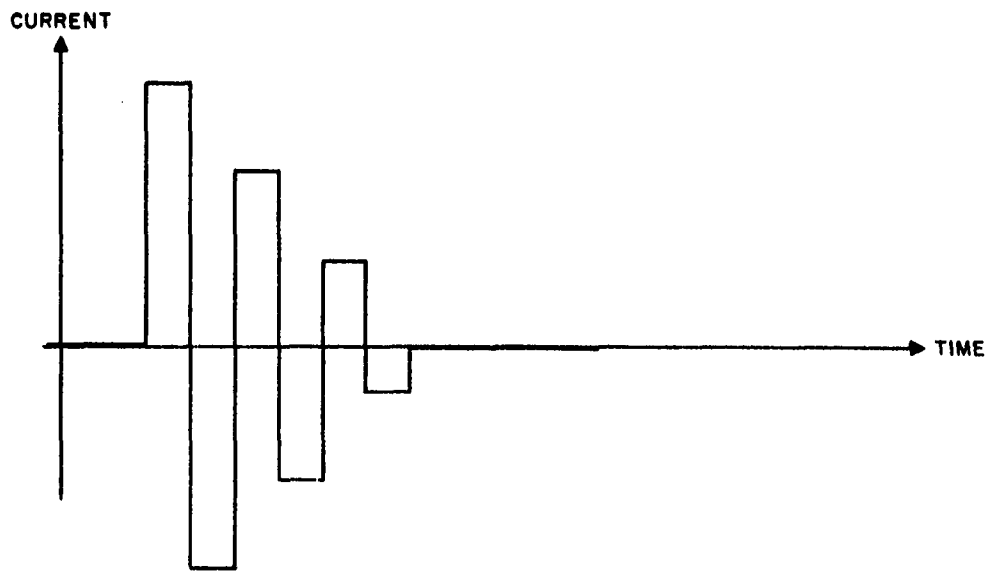


Figure 1-4a. Current Input Signal for Domain Storage, Writing Operation.

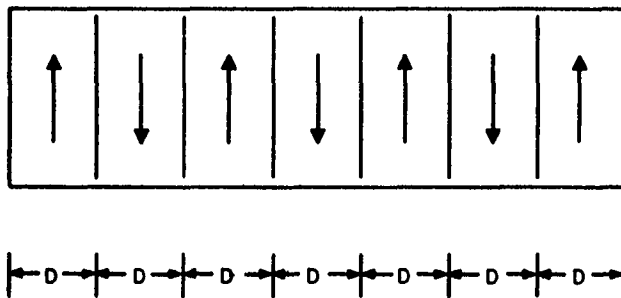


Figure 1-4b. Idealized Domain Storage Geometry. (Arrows Indicate Magnetization Direction)

### 1.3 Experimental Studies of Domain Wall Motion

A study of the velocity of domain walls was made possible by the development of magnetic films in which single walls could be moved without the nucleation and growth of extraneous domains. The magnetization at the edges of these films assumes a 90° "curling" configuration upon easy axis saturation.<sup>(4)</sup> Since any switching signal is due to the motion of one unique wall, the steady-state wall velocity may be measured by noting the time duration of the signal and the distance the wall moves during this time interval. For the time intervals used, the transient effect may be neglected.

To obtain an idea of the range of ramp rate necessary to achieve results comparable with theory, the "cross-over" value of ramp rate will be found. This is done by equating  $(V_w)_a = (V_w)_b$  in Eq. 1-15. This yields, for the parameter values used earlier,

$$\gamma_c = \frac{H_c^2 R}{\alpha} = 6.3 \times 10^4 \text{ amp/sec.} \quad (1-16)$$

Experimental data was taken over the range  $\gamma = 0.2 \times 10^4$  to  $\gamma = 50 \times 10^4$  amp/sec. In taking data, two different sensory techniques were used. These were (a), sensing the motion of the wall by means of an electrical voltage signal induced in a reading coil,<sup>(5)</sup> and (b) sensing the motion of the wall by means of a photocell and polarizers, utilizing the Kerr effect.<sup>(6)</sup>

For lower values of  $\gamma$  the electrical output signal is not of sufficient amplitude to enable one to distinguish it unambiguously from the background noise level. At higher values of  $\gamma$  the output of the photocell is ambiguous as the frequencies of the integrated signal produced by the photocell and those of the background noise coincide. Thus experimental data was taken using the optical sensor from  $\gamma = 0.2 \times 10^4$  to  $\gamma = 5 \times 10^4$  amp/sec, and using the electrical sensor from  $\gamma = 1 \times 10^4$  to  $\gamma = 50 \times 10^4$  amp/sec. There is some difficulty in measuring unambiguously the time duration of the optical output signal. The limiting values of time duration for each ramp rate were obtained by repeated measurements when the optical pickup was used.

The films used in this experiment were those exhibiting the "curling edge" configuration.<sup>(4)</sup> Using these films it is possible to move one domain wall along the film without extraneous walls nucleating ahead of the main domain wall. Thus the experimental data is comparable with that found theoretically for the use of a single domain wall.

Several films were examined using the process described above. A typical result is shown in Fig. 1-5. The domain wall velocity is plotted as a function of current ramp rate using log-log coordinates. Also shown in Fig. 1-5 are the asymptotes to the curve of slope 1 and 1/2 respectively. From these asymptotes the values of the wall coercive force,  $H_c$ , and the wall mobility,  $R$ , may be calculated. For the data shown in Fig. 1-5 the results are  $H_c = 1.9$  oe, and  $R = 6 \times 10^3$  cm/sec - oe.

#### 1.4 Conclusions

The expression for domain wall velocity given by Eq. (1) appears to accurately represent the motion of domain walls in a field generated by a current ramp. For  $\gamma \ll H_c^2 R/4\alpha$  the wall velocity is proportional to the ramp rate and inversely proportional to the wall coercive force. The wall velocity is independent of the wall mobility. For  $\gamma \gg H_c^2 R/4\alpha$  the wall velocity is proportional to the one-half power of the ramp rate-mobility product and is independent of the coercive force.

This type of behavior indicates that at lower values of wall velocities the limiting factor is microscopic film imperfections. These imperfections appear on a gross basis as the wall coercive force. At higher wall velocities the limiting factor becomes induced electromagnetic fields due to the rapid rate of magnetization switching. These induced fields, by Lenz's law, act such as oppose the fields inducing them and thus to limit the wall velocity. If Eq. 1-1 is taken as representing the steady-state behavior of a domain wall it follows that the transient behavior described in Section 1 must also occur. Due to the short time intervals and low signal levels evidence involved no direct experimental evidence of this transient effect has been found. The available equipment (6) would have to be modified to obtain higher ramp rates in order for the transient to be measured directly.

In designing any device based on the motion of domain walls, the effect of the velocity transient must be taken into account. Theories based on a linear ramp duration - distance wall moves relationship are incorrect. The correction for velocity transient time is especially critical if high wall packing densities are being considered. This is due to the dependance of the velocity transient upon initial wall position.

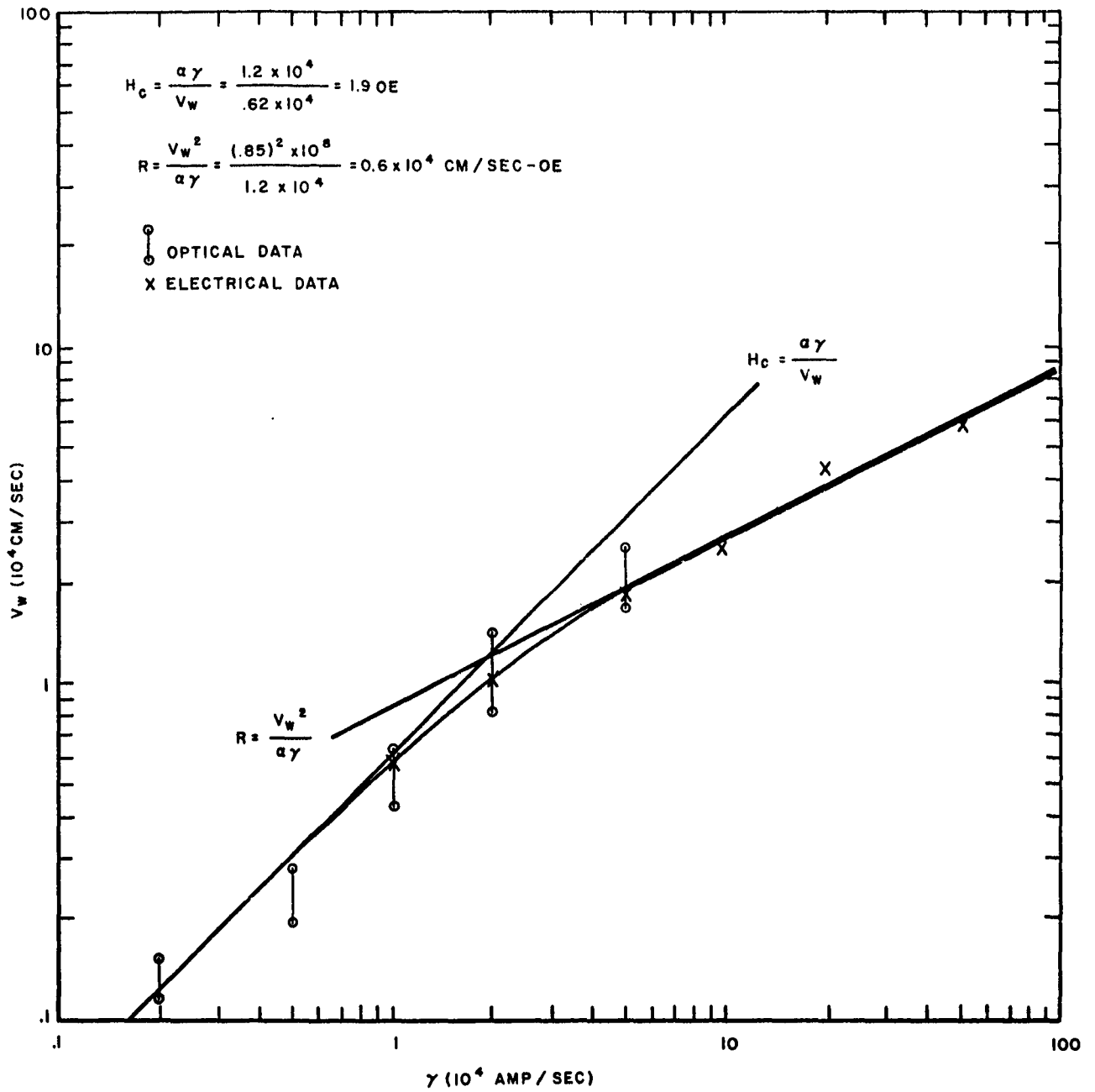


Figure 1-5. Wall Velocity vs. Ramp Rate.

### Bibliography

1. LFE Annual Report #570-A2, page 1-2.
2. Ibid page 15, Eq. 2.
3. Ibid page 15, Eq. 5.
4. LFE Annual Report #570-A3, page 2-9 to 2-13, page 2-28 to 2-39.
5. Ibid page 1-3 to 1-6.
6. Ibid page 3-5 to 3-12.

## 2. MAGNETIZATION CONFIGURATIONS AT EDGES IN THIN FILMS

### 2.1 Introduction

In Chapter II of Annual Report 570-A3 four types of magnetization distributions at film edges were considered. These were: an "abrupt edge" configuration, a "tapered edge" configuration, a "curling" configuration, and a "closure domain" configuration. The configurations are illustrated in Figs. 2-1 through 2-4.

In this chapter a new configuration, called the "tapered edge curling" configuration, is introduced and analyzed theoretically. In conclusion, a summary of the new results together with those from Report 570-A3 are given. The theoretically expected magnetization distribution at an edge is discussed as a function of film thickness and edge taper angle.

### 2.2 The "Tapered Edge Curling" Configuration

There are two possible ways in which a 90° curling configuration may appear in a tapered edge film. One of these is shown in Fig. 2-5. The energy of this configuration is equal to that of the 90° curling configuration<sup>(1)</sup> plus an additional term due to the anisotropy energy of the tapered region.

The additional energy  $E'_k$  per unit film length in the hard direction is

$$E'_k = 2K \left( \frac{1}{2} T^2 \cot \phi \right) = K T^2 \cot \phi , \quad (2-1)$$

where  $K$  is the anisotropy constant,  $T$  is the film thickness, and  $\phi$  is the edge taper angle. Since all other energy terms are of the order of  $M^2 T^2$ , where  $M$  is the magnetization, and since  $K/M^2 \ll 1$ , the  $E'_k$  energy term may be neglected.

Thus the energy of this configuration is essentially that of the 90° curling configuration in a non-tapered edge film.

The other possible "tapered edge curling" configuration is shown in Fig. 2-6. This configuration combines the distributed magnetization divergence of the "curling" configuration with the tilted planes of equal charge density common to a "tapered edge" film.

It is apparent that an additional exchange energy term must be included in the energy of this configuration due to the magnetization rotation perpendicular to the film plane in the region of curling.

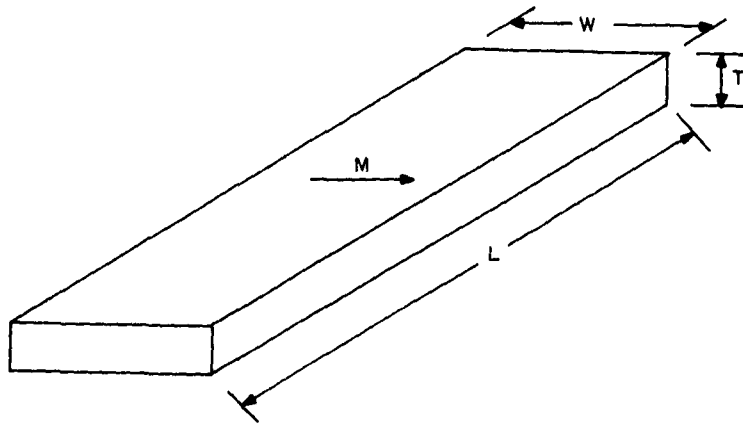


Figure 2-1. The "Abrupt Edge" Configuration.

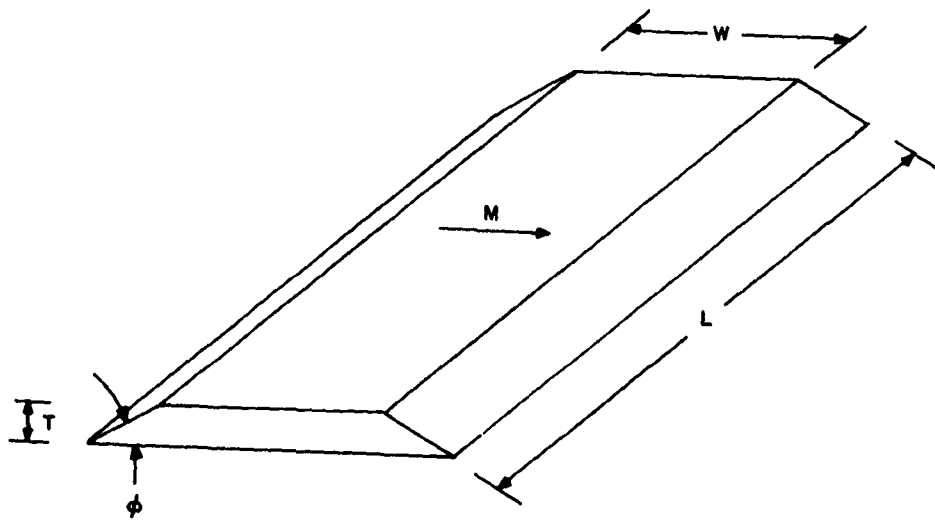


Figure 2-2. The "Tapered Edge" Configuration.

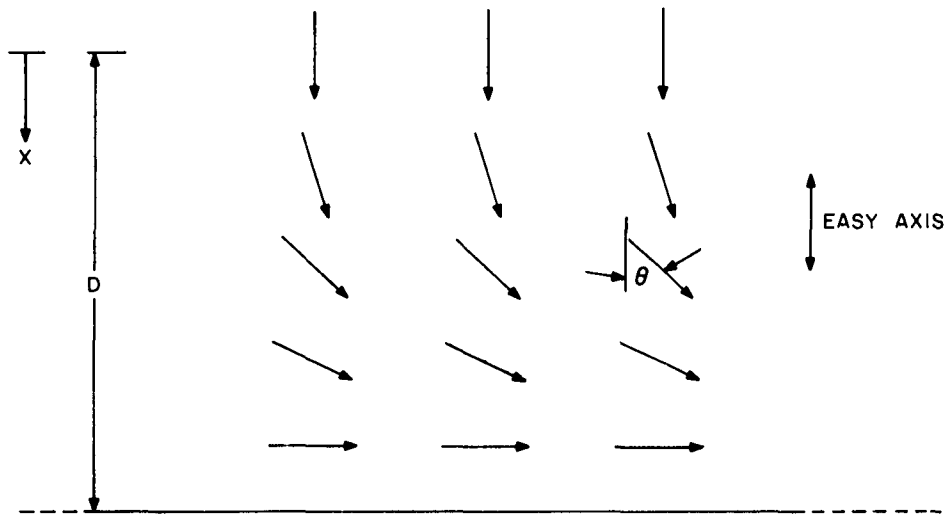


Figure 2-3. The 90° "Curling" Configuration.  
 (Arrows Indicate Magnetization Direction)

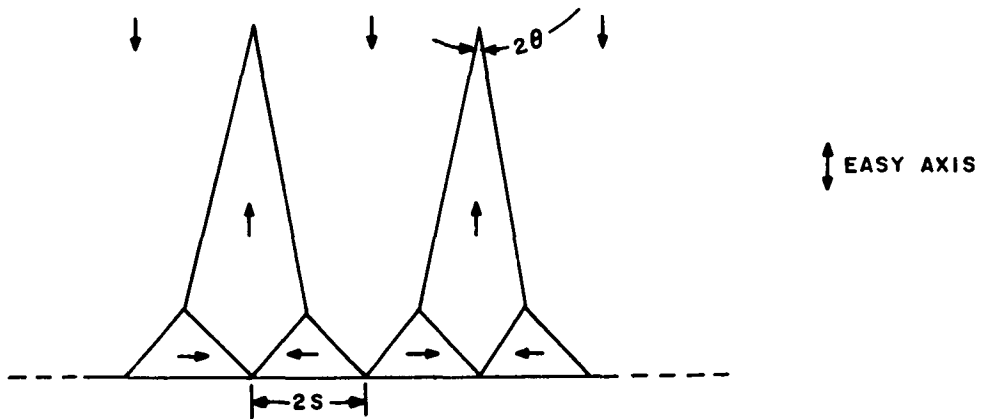


Figure 2-4. The "Closure Domain" Configuration.  
 (Arrows Indicate Magnetization Direction)

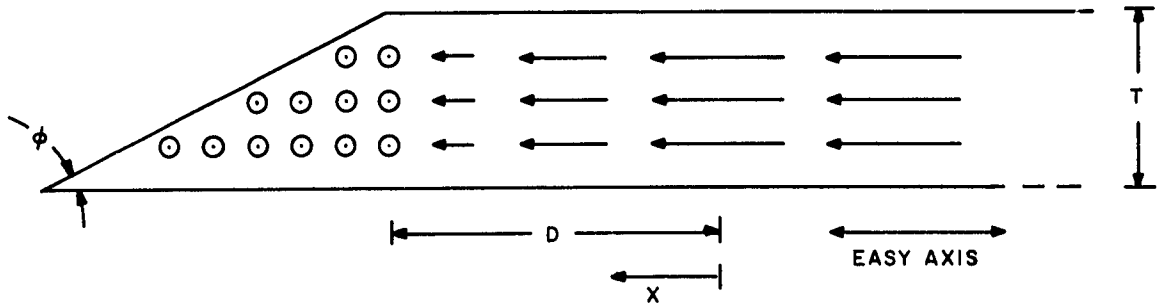


Figure 2-5. Possible "Tapered Edge Curling" Configuration.  
 (Arrows Indicate X Component of the Magnetization)

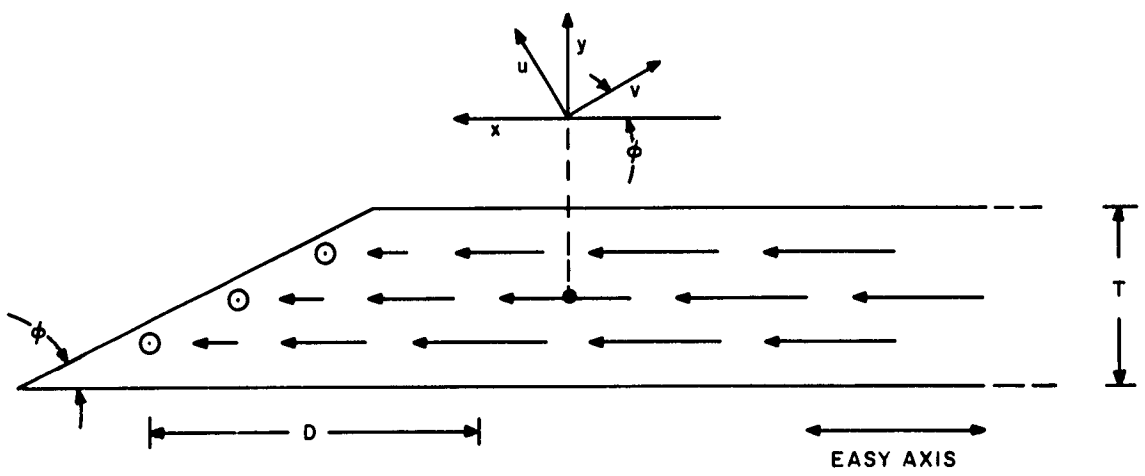


Figure 2-6. Possible "Tapered Edge Curling" Configuration.  
 (Arrows Indicate X Component of the Magnetization)

To compute the new exchange energy term, it is necessary to know how  $\theta$ , the angle between the magnetization and the easy axis, varies as a function of the x and y coordinates. The coordinate system is shown in Fig. 2-6. It will be assumed that

$$\theta = \cos^{-1} \left[ 1 - \frac{(x + y \cot \phi)^2}{D^2} \right], \quad (2-2)$$

is a reasonable approximation to this distribution. Here D is the distance over which the curling takes place.  $E_x$ , the exchange energy per unit length of film given previously<sup>(2)</sup> must now be modified to take into account the angular dependence of  $\theta$  upon  $\phi$  given by Eq. 2-2. Changing to the (u, v) coordinates of Fig. 2-6 enables Eq. 2-2 to be written as

$$\theta = \cos^{-1} \left[ 1 - \frac{u^2}{(D \sin \phi)^2} \right]. \quad (2-3)$$

The exchange energy,  $E_x$ , is given by

$$E_x = 2A \frac{T}{\sin \phi} \int_0^{D \sin \phi} \left( \frac{d\theta}{du} \right)^2 du, \quad (2-4)$$

where A is the exchange constant.

Upon integration Eq. 2-4 becomes

$$E_x = 4 \sqrt{2} \frac{AT}{D \sin^2 \phi} \left[ \tanh^{-1} \frac{1}{\sqrt{2}} \right] = (5.0) AT/D \sin^2 \phi. \quad (2-5)$$

The anisotropy energy may also be found from Eq. 2-2. However, inspection of Fig. 2-6 makes it apparent that the result is independent of  $\phi$ . Therefore, the anisotropy energy per unit length,  $E_k$ , is simply<sup>(2)</sup>

$$E_k = \frac{14}{15} KTD. \quad (2-6)$$

The calculation of the demagnetization energy is extremely difficult and will not be attempted here. Instead an analogy will be drawn between the "abrupt edge" and "tapered edge" results on the one hand and the "curling" and "tapered edge curling" results on the other.

From previous results<sup>(3, 4)</sup> the following analogy may be drawn:

$$\begin{aligned} \text{"Abrupt Edge"} &\longleftrightarrow \text{"Tapered Edge"} & (2-7) \\ 3 + 2 \ell n w &\longleftrightarrow 5 + 2 \ell n (w \sin \phi) + 4 \sin \phi - 6 \sin^2 \phi . \end{aligned}$$

Keeping the coefficient ratios for equivalent terms the same as in Eq. 2-7, the following analogy will be drawn between the "curling" and "tapered edge curling" results.

$$\begin{aligned} \text{"Curling"} &\longleftrightarrow \text{"Tapered Edge Curling"} & (2-8) \\ \frac{29}{6} + 2 \ell n \frac{w}{d} &\longleftrightarrow \frac{145}{18} + 2 \ell n (w \sin \phi / d) + \frac{58}{9} \sin \phi - \frac{29}{3} \sin^2 \phi . \end{aligned}$$

In Eqs. 2-7 and 2-8,  $w$  is the normalized film width,  $W/T$ , and  $d$  is the normalized curling distance,  $D/T$ . While the coefficients of the "tapered edge curling" expression given by Eq. 2-8 are probably incorrect, it is felt that the functional form is correct enough to yield results of the right order of magnitude.

The total energy per unit length  $E_{tp}$ , of the "tapered edge curling" configuration can now be written as

$$\begin{aligned} E_{tp} = M^2 T^2 & \left[ \frac{145}{18} + 2 \ell n (w \sin \phi / d) + \frac{58}{9} \sin \phi - \frac{29}{3} \sin^2 \phi \right] \\ & + \frac{14}{15} K T^2 d + \frac{(5.0) A}{d \sin^2 \phi} . \end{aligned} \quad (2-9)$$

It is now desired to minimize  $E_{tp}$  with respect to taper angle  $\phi$  and normalized curling distance  $d$ :

$$\begin{aligned} \partial E_{tp} / \partial \phi = M^2 T^2 & \left[ \frac{2}{\sin \phi} + \frac{58}{9} - \frac{58}{3} \sin \phi \right] \cos \phi \\ & - \frac{10A}{d} \frac{\cos \phi}{\sin^3 \phi} = 0 , \end{aligned} \quad (2-10)$$

$$\partial E_{tp} / \partial d = M^2 T^2 \left[ \frac{-2}{d} + \frac{14}{15} K T^2 - \frac{(5.0) A}{d^2 \sin^2 \phi} \right] = 0 . \quad (2-11)$$

Since the taper angles of most films are extremely small, the solution of Eqs. 2-10 and 2-11 of particular interest is when  $\phi \ll 1$ . For this case, Eq. 2-10 may be reduced to

$$M^2 T^2 \left[ \frac{2}{\sin \phi_0} \right] - \frac{10A}{d \sin^3 \phi_0} = 0 . \quad (2-12)$$

The solution of Eq. 2-12 is

$$\sin^2 \phi_o = 5 A / M^2 T^2 d \quad . \quad (2-13)$$

Substituting Eq. 2-13 into Eq. 2-11 and solving for d yields

$$d = \frac{45}{14} M^2 / K \quad . \quad (2-14)$$

Substituting Eq. 2-14 into Eq. 2-13 yields

$$\sin^2 \phi_o = 14 AK / 9 M^4 T^2 \quad . \quad (2-15)$$

As a check on the initial assumption that  $\phi_o \ll 1$ , the following values will be used in Eq. 2-15

$$\begin{aligned} A &= 10^{-6} \text{ erg/cm,} \\ K &= 10^3 \text{ erg/cm}^3, \\ M &= 700 \text{ e.m.u.,} \\ T &= 1000 \text{ \AA.} \end{aligned} \quad (2-16)$$

Upon substituting these values into Eq. 2-15, it is found that

$$\phi_o \approx \sin \phi_o = 8 \times 10^{-3} \text{ rad.,} \quad (2-17)$$

which satisfies the original assumption.

Substituting Eqs. 2-14 and 2-15 into Eq. 2-9 and dropping lower order terms yields

$$E_{tp} = M^2 T^2 \left[ 12 + \ln \left( \frac{14K \sqrt{14AK}}{135 M^4 T} \right) \right] \quad . \quad (2-18)$$

It is of interest to compare this energy with that of the "90° curling" configuration,  $E_p$ , and that of the "closure domain" configuration,  $E_c$ , as a function of film thickness. These energies, normalized to the "abrupt edge" energy,  $E_a$ , are shown in Fig. 2-7.

The results of Fig. 2-7 show that the "tapered edge curling" configuration has, for the correct taper angle, a lower energy than the "closure domain" configuration over a large range of film thickness. It appears, therefore, that films thicker than the 500 Å maximum previously predicted<sup>(6)</sup> may be deposited wherein the "closure domain" configuration will not appear.

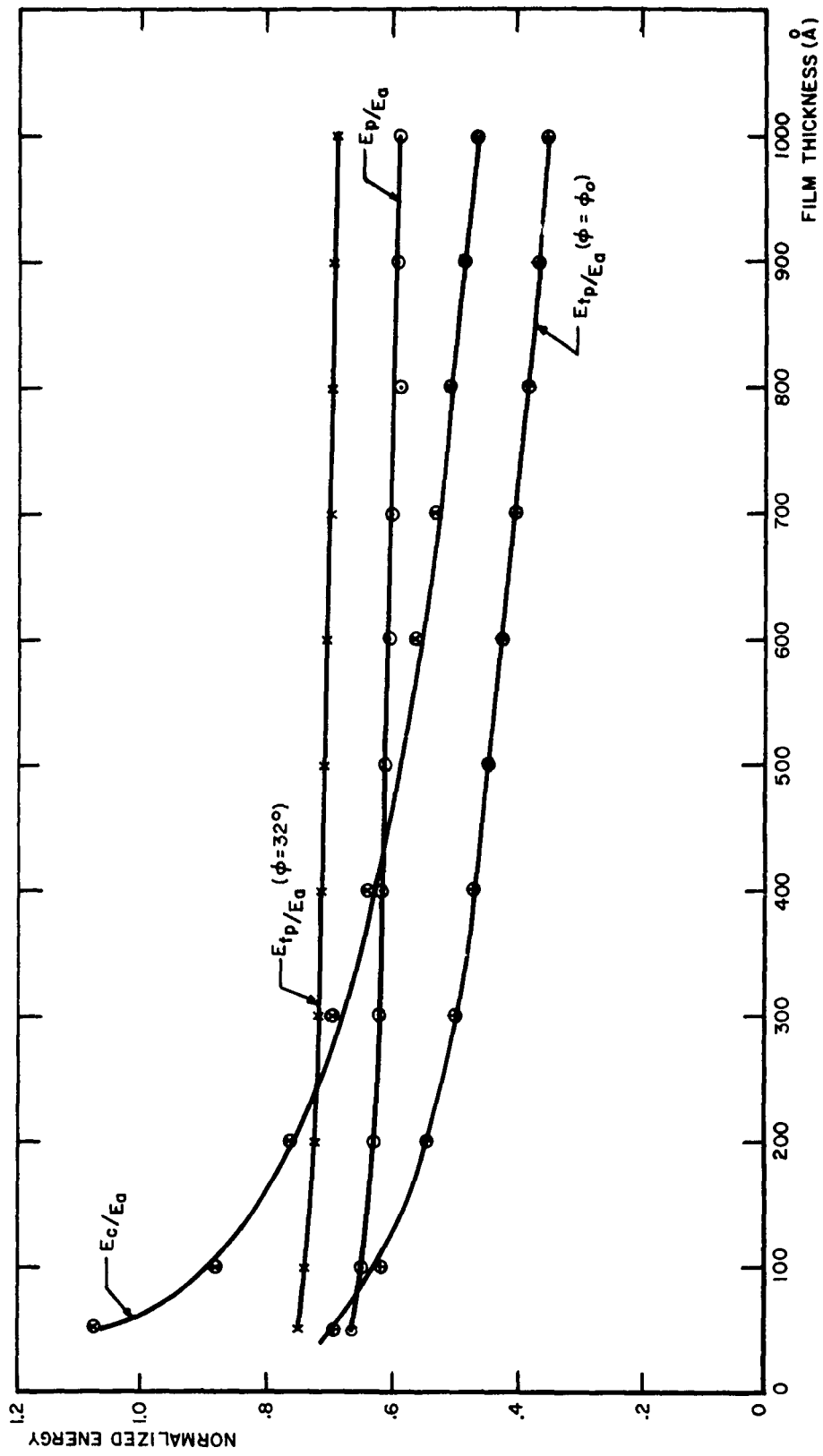


Figure 2-7. Normalized Energies of Various Edge Configurations vs. Film Thickness.

Certain other extrema may be found from Eq. 2-10. One of these is

$$\cos \phi = 0, \phi = 90^\circ . \quad (2-19)$$

Another is found by assuming  $\sin \phi$  to be relatively large. For the parameter values of Eq. 2-16,  $M^2 T^2 \sim 5 \times 10^{-5}$  and  $10 A/d \sim 5 \times 10^{-9}$ . Thus, for a value of  $\sin \phi$  of the order of 0.1, the exchange term may be neglected. This leaves

$$\frac{2}{\sin \phi} + \frac{58}{9} - \frac{58}{3} \sin \phi = 0 . \quad (2-20)$$

The solution of Eq. 2-20 is

$$\sin \phi = 0.53, \phi = 32^\circ , \quad (2-21)$$

which satisfies the original assumption.

The results of Eqs. 2-19 and 2-21 indicate that  $E_{tp}$  has a relative maximum at  $\phi = 32^\circ$  and a relative minimum at  $\phi = 90^\circ$ . Since  $E_{tp}$  increases for  $\phi < \phi_0$ , it can be concluded that if  $E_{tp}(\phi = 32^\circ)$  is greater than  $E_c$ , there exists a taper angle-thickness range about  $\phi_0$  as given by Eq. 15 in which  $E_{tp} < E_c$ . That  $E_{tp}(\phi = 32^\circ)$  is greater than  $E_c$  over the thickness range of interest ( $T > 450 \text{ \AA}$ ) is shown in Fig. 2-7. Note that at  $\phi = 32^\circ$ ,  $d = (15 M^2/7K)$ .<sup>(5)</sup>

### 2.3 Summary

The complete results of Chapter II, Report 570-A3, and the new results presented here are shown in Fig. 2-8. In this diagram the energetically-preferred edge configuration is presented as a function of film thickness and edge-taper angle. These results predict the theoretical possibility of having films thicker than 500 Å that will not have "closure domain" edge configurations. The only requirement to avoid "closure domains" is to deposit the films within the range of taper angle indicated in Fig. 2-8.

Some experiments have been performed in an attempt to observe the absence of "closure domains" in films thicker than 600 Å. These have met with limited success. This may be partly attributed to the difficulty of depositing films with the correct taper-angle film-thickness relationship. Some tapered-edge films of thickness 1500 Å have been deposited, however, that show an absence of the usual "closure domain" pattern. While too few successes have been obtained to consider the theoretical results as confirmed, they are sufficient to indicate a real possibility of obtaining relatively thick films in which controlled domain wall information storage<sup>(7)</sup> is feasible.

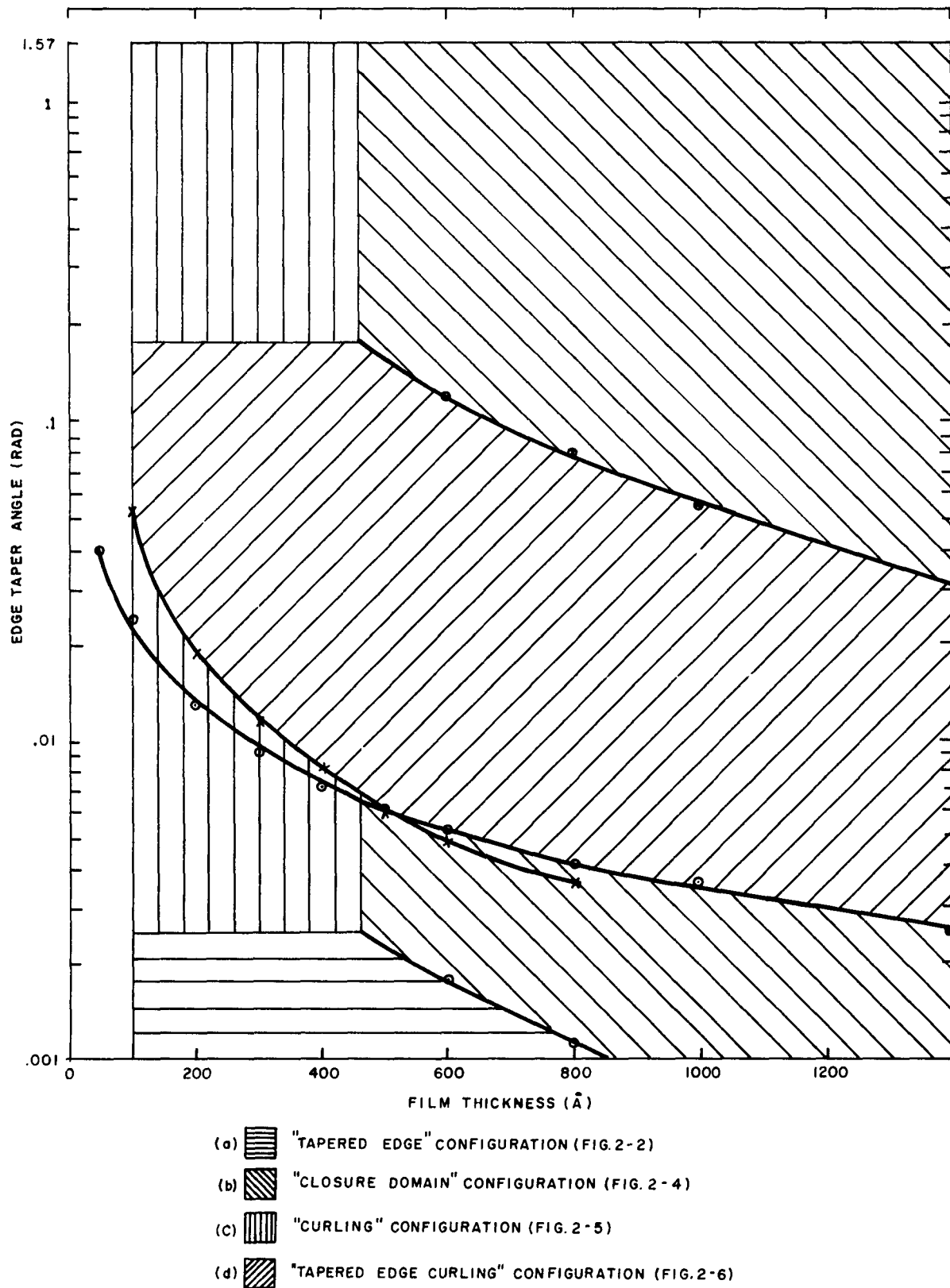


Figure 2-8. Theoretically Expected Edge Configuration as a Function of Film Thickness and Edge Taper Angle

## Bibliography

- 1) Report No. 570-A3: pg. 2-12, Eq. (2-3).
- 2) Ibid: pg 2-9.
- 3) Ibid: pg 2-3, Eq. (2-1).
- 4) Ibid: pg 2-7, Eq. (2-2).
- 5) Ibid: pg 2-12.
- 6) Ibid: pg 2-21; pg 2-22, Fig. 2-12.
- 7) H. W. Fuller and H. Rubinstein "Large Capacity Memory Techniques for Computing Systems", edited by M. C. Yovitz (Macmillan Company, New York 1962) pg 163-176.

### 3. ELECTRON MICROSCOPE STUDIES

#### 3.1 Introduction

In order to study directly the magnetization distribution at film edges it was decided to prepare specimens appropriate for examination in the electron microscope. The first method of preparation was to evaporate films directly onto carbon-covered specimen grids. This method was unsuccessful and it was decided to develop a technique for stripping a film from a glass substrate. After various modifications, it was possible to prepare useful electron microscope specimens by this technique. A stripping technique of preparing specimens has the considerable advantage of permitting macroscopic examination of film properties before the film is removed from the substrate.

#### 3.2 Preparation of Films for Electron Microscope

3.2.1 Direct Deposition on Specimen Grids. The first method used to prepare specimens for use in the electron microscope was to deposit films directly onto carbon-covered specimen grids. The direction of the original orienting field was marked on the grids by masking a section of the grid with a straight edge perpendicular to the easy direction. The melt composition used was 80% Ni - 17% Fe - 3% Co. The substrate temperature was 100 - 200°C and film thickness ranged from 200 to 500 Å.

The films prepared by this technique were found to be unsatisfactory. Their coercive forces were generally over 6 oe indicating poor film quality. In addition, an extremely long edge taper was obtained. As shown in Figs. 3-1 and 3-2, domain walls can be observed up to 100 μ past the apparent film edge. These walls have a very high coercive force and cannot be removed satisfactorily. For these reasons, it was decided to try other techniques for the preparation of electron microscope specimens.

3.2.2 Methods of Stripping of Films from Substrates. In developing a technique for removing a film from its glass substrate, it was found to be practically impossible to carry out the removal without severe damage to the film. This was especially true when the substrates were heated during deposition to improve film properties. To reduce film damage, it was decided to coat the substrate with a dissolvable substance before film deposition.

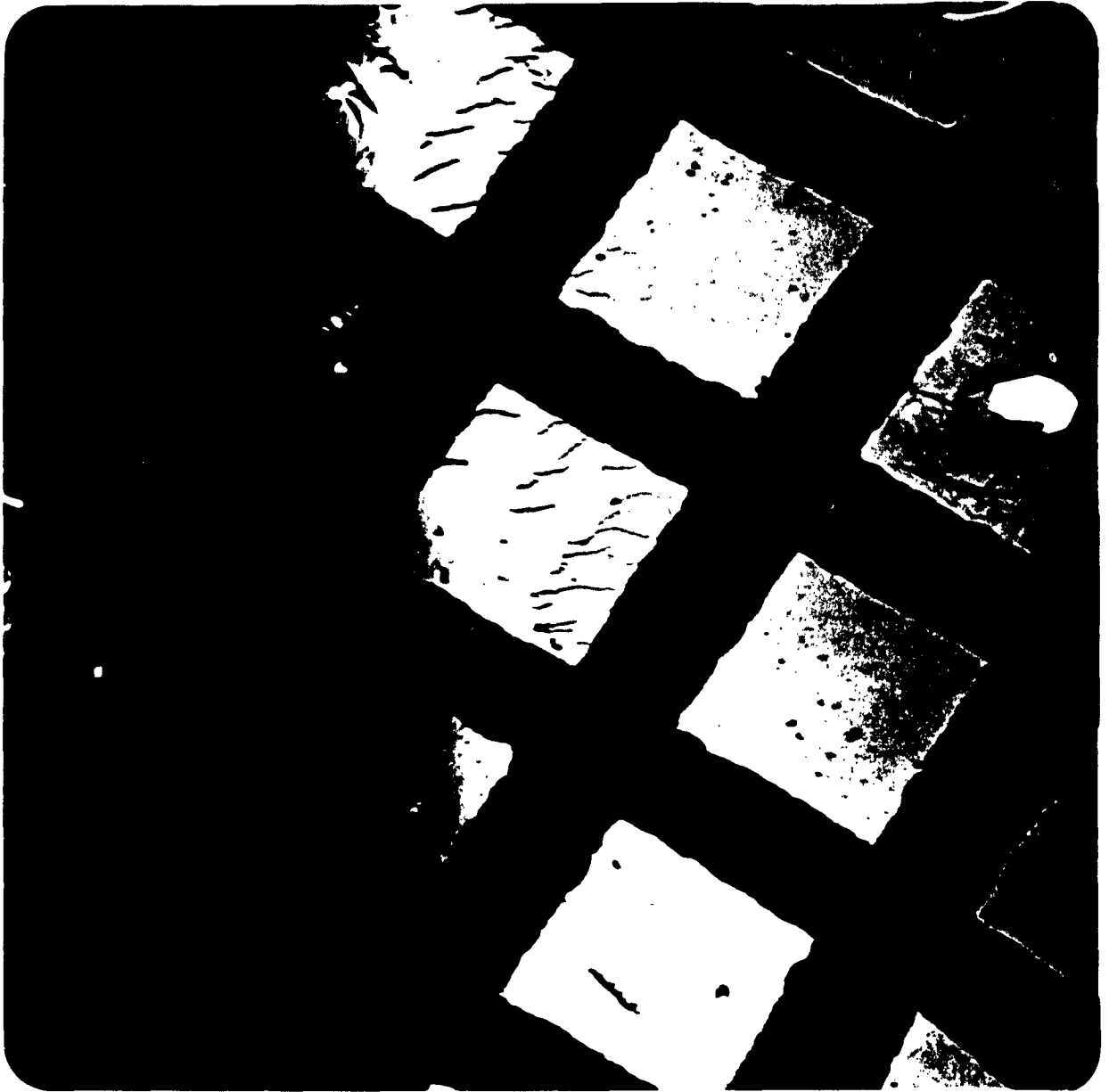


Figure 3-1. Domain Walls Extending Beyond Apparent Film Edge. (200 Mesh-Grid)

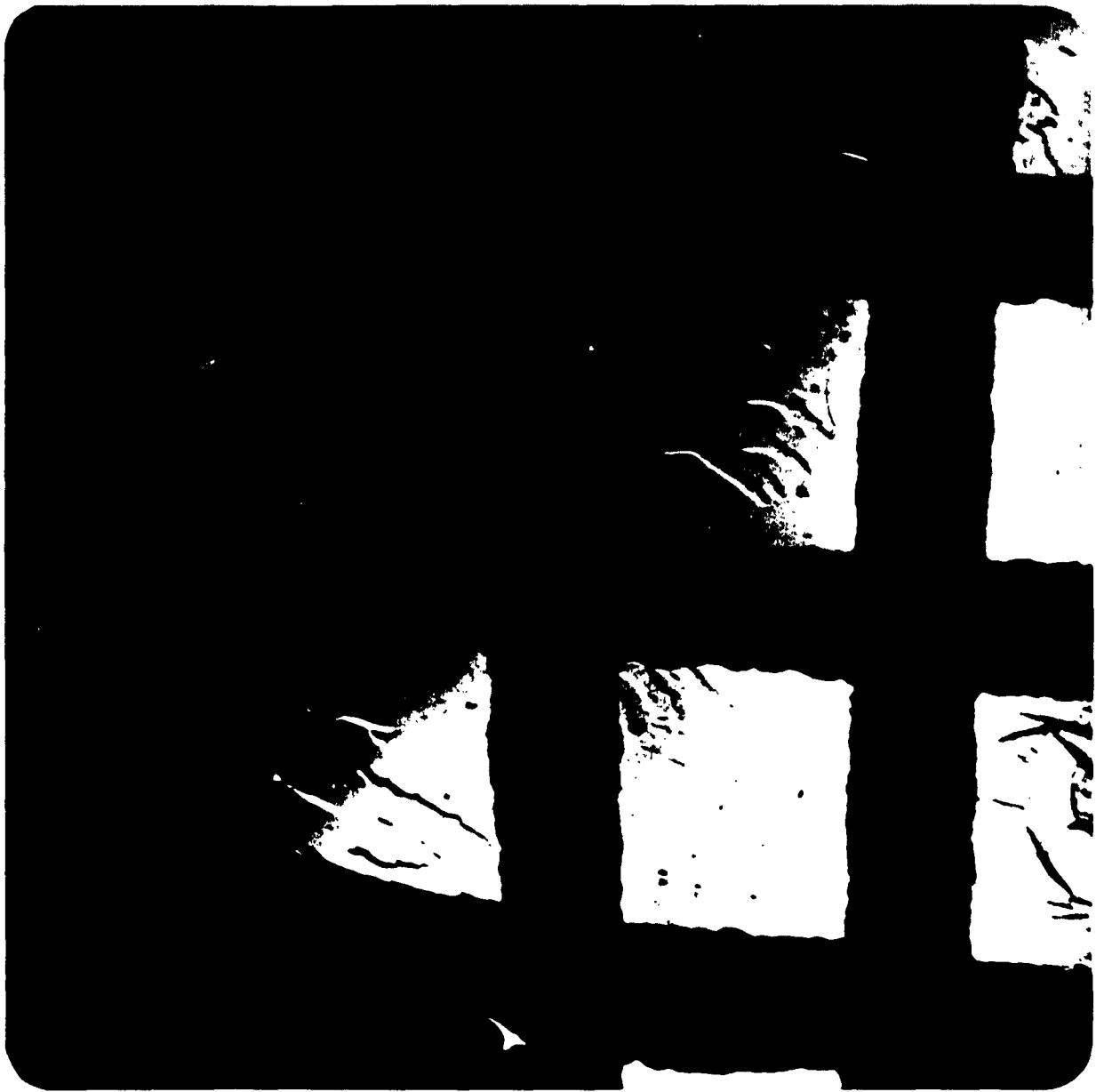


Figure 3-2. Domain Walls Extending Beyond Apparent Film Edge. (200 Mesh-Grid)

The first substance used was Formvar which dissolves in ethylene dichloride. This was unsuccessful as the films tended to flake into particles too small for practical use during the stripping operation.

Next the Ernest Fulham product, Victawet, was tried. Victawet dissolves quite readily in water. With it as an undercoating, a film can be easily floated off intact from its substrate. Particles of film can then be easily broken off and floated onto carbon-covered specimen grids for study in the electron microscope.

**3.2.3 Film Preparation on Victawet Coated Substrates.** The first method used to prepare films on Victawet coated substrates was as follows:

(a) Victawet was deposited onto suitably prepared 1"-square glass substrates in the Hi-Vac system. The evaporation was from a tungsten boat heated by passing a current through it. Boat temperature reached 500°C during this process. The substrate was at room temperature during Victawet deposition.

(b) The Victawet-overcoated substrate was transferred to the CEC system where magnetic film deposition was performed. It was found that a substrate temperature of over 100°C resulted in a degradation of film properties. Experiments carried out in air showed that Victawet developed a tacky surface when heated above 100°C. It was thus felt that the exposure of the Victawet coated substrate to air during transfer from the Hi-Vac to the CEC system was responsible for the degradation of film properties at substrate temperatures greater than 100°C.

To test this hypothesis the transfer time between systems was allowed to vary from a few seconds to over 24 hours. A definite relation was established between this transfer or air exposure time and resulting film quality (e.g., coercive force, dispersion). Best results were obtained when air exposure was reduced to the absolute minimum necessary for substrate transfer between systems.

In order to eliminate exposure to air entirely the CEC system was modified to allow deposition of both Victawet and film material without admitting air to the system. The modified system is shown in Figs. 3-3 and 3-4. The tungsten boat used for Victawet evaporation was placed on top of the shutter covering the magnetic alloy crucible. This eliminates any possibility of angle-of-incidence effects for either material.

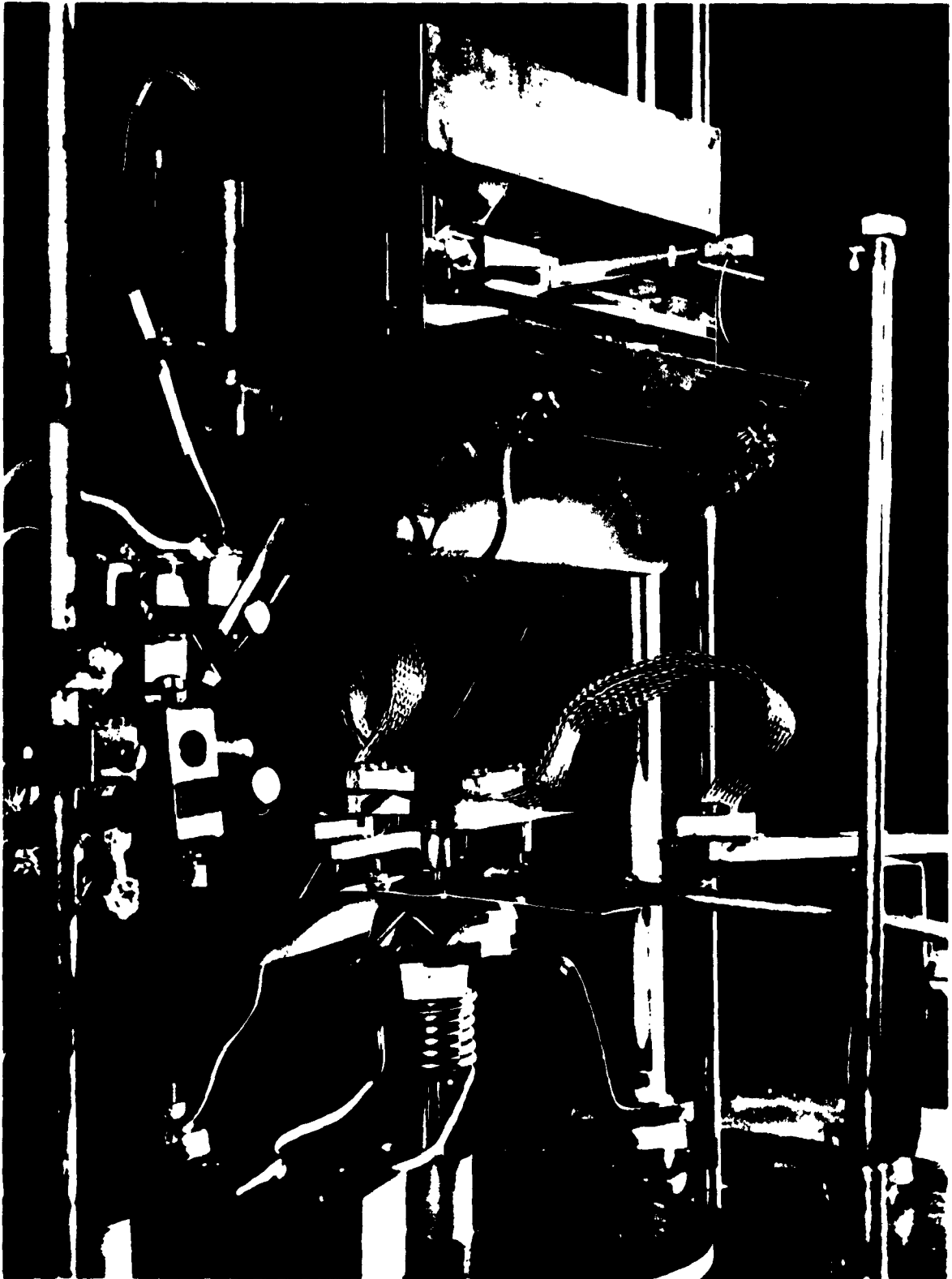


Figure 3-3. Modified Deposition System for Victawet Undercoating Studies.

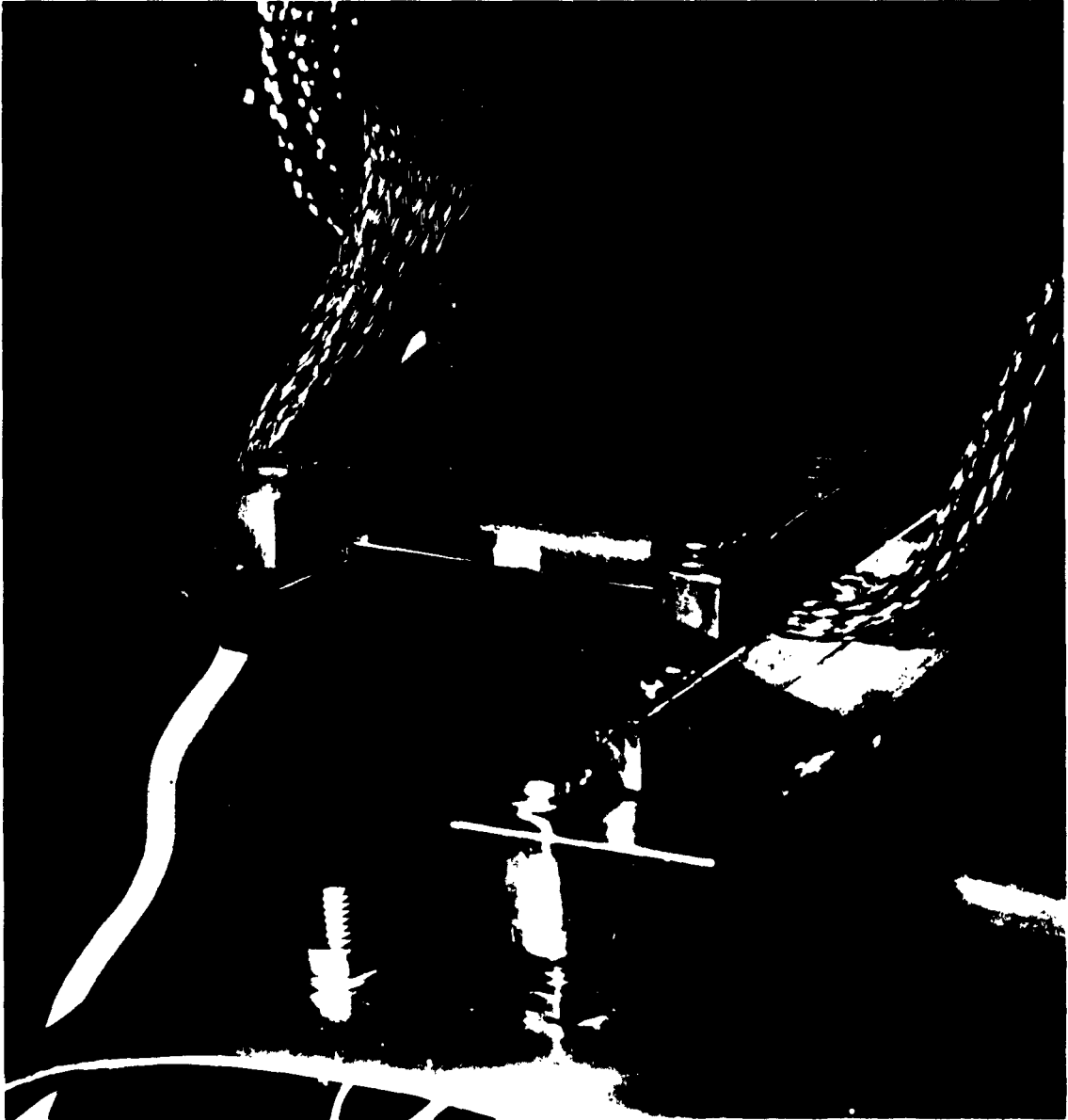


Figure 3-4. Resistance Heated Tungsten Boat used for Victawet Evaporation.

Since exposure of the victawet-coated substrate to air was now eliminated, it was hoped that an increase in substrate temperature would lead to films with properties similar to those obtained by direct deposition on glass substrates. More specifically, films with an  $H_c$  of 1.5 to 3 oe, an  $H_k$  of 3 to 5 oe, and a dispersion of under  $1^\circ$ , as measured on the hysteresis curve tracer<sup>(1)</sup> were sought, simultaneously with the ability to remove the films from their substrates. A high substrate temperature causes evaporation of the Victawet from the substrate before the film can be deposited. It was hoped, however, that a substrate temperature approaching  $250^\circ\text{C}$  (used for best results with non-coated glass substrates) would be attainable.

A summary of the experimental results obtained is given in Table 3-1. Best results were obtained by using a substrate temperature of  $20 - 25^\circ\text{C}$  during Victawet deposition and one of  $200 - 225^\circ\text{C}$  during film deposition. A deposition rate of  $20 - 40 \text{ \AA}/\text{sec}$  gave best results. At temperatures higher than  $225^\circ\text{C}$  the films could not be floated off. Specimens prepared at these optimum conditions compared favorably with the best films deposited directly on glass substrates.

It was found that if the Victawet and the film were deposited through the same mask, the film could not be floated off regardless of other preparation parameters. It was felt that this was due to the film edges passing beyond the Victawet and touching the glass directly. This problem was solved by using the movable mask of Fig. 3-5. The Victawet was deposited through the  $1/4''$  wide slot shown in Fig. 3-5a while the film was deposited through the  $1/8''$  wide slot shown in Fig. 3-5b. With this technique, films float easily off the substrates if other preparation parameters are correctly chosen.

The properties of Film #790A are shown in Fig. 3-6. Figure 3-6a shows the switching output signal ( $\dot{B} - H$  curve) in the easy direction while Fig. 3-6b shows the same function in the hard direction.

### 3.3 Micrographs of Film Edges

In Figs. 3-1 and 3-2 the type of edges obtained by direct evaporation on carbon-covered specimen grids is shown. An example of the sharp edges possible by using a specimen prepared by the Victawet process is shown in Fig. 3-7. Using electron microscope specimens with these types of edges, a detailed study of magnetization distributions at film edges is planned.

<u>No.</u>	<u>Substrate Temp. (°C)</u> <u>Victawet Film</u>	<u>Evap. Time</u> <u>(sec)</u>	<u>Thickness (A)</u>	<u>H<sub>c</sub>(oe)</u>	<u>H<sub>k</sub>(oe)</u>	<u>Disp. (deg)</u>	<u>Remarks</u>
743A	23 90	30	540	3.1	5.4	0.5	Floats off. Too thick for specimen.
744A	23 88	20	140	2.0	2.0	11.0	Floats off. Very high dispersion.
745A	265 260	20	120	3.0	3.0	1.0	Doesn't float off.
747A	23 80	23	100	2.0	1.1	very high	Floats off. Ragged wall motion.
783A	23 125	7	120	1.8	2.3	5.0	Floats off.
784A	23 150	7	160	2.0	3.0	2.5	Floats off.
787A	23 175	7	170	2.1	4.0	1.0	Floats off.
788A	23 200	7	160	1.9	3.0	0.5	Floats off.
790A	23 225	7	160	2.0	3.5	0.5	Floats off.
792A	23 225	7	300	3.0	5.0	0.5	Floats off.
789A	23 250	7	200	2.2	3.8	0.5	Doesn't float off.
791A	23 250	7	70	1.8	3.0	5.0	Doesn't float off.

3  
8

743A - 747A: Evaporation rates of 4 to 7 A/sec. (except 743A).

783A - 792A: Evaporation rates of 17 to 43 A/sec. (except 791A).

Table 3-1. Properties of victawet undercoated films.

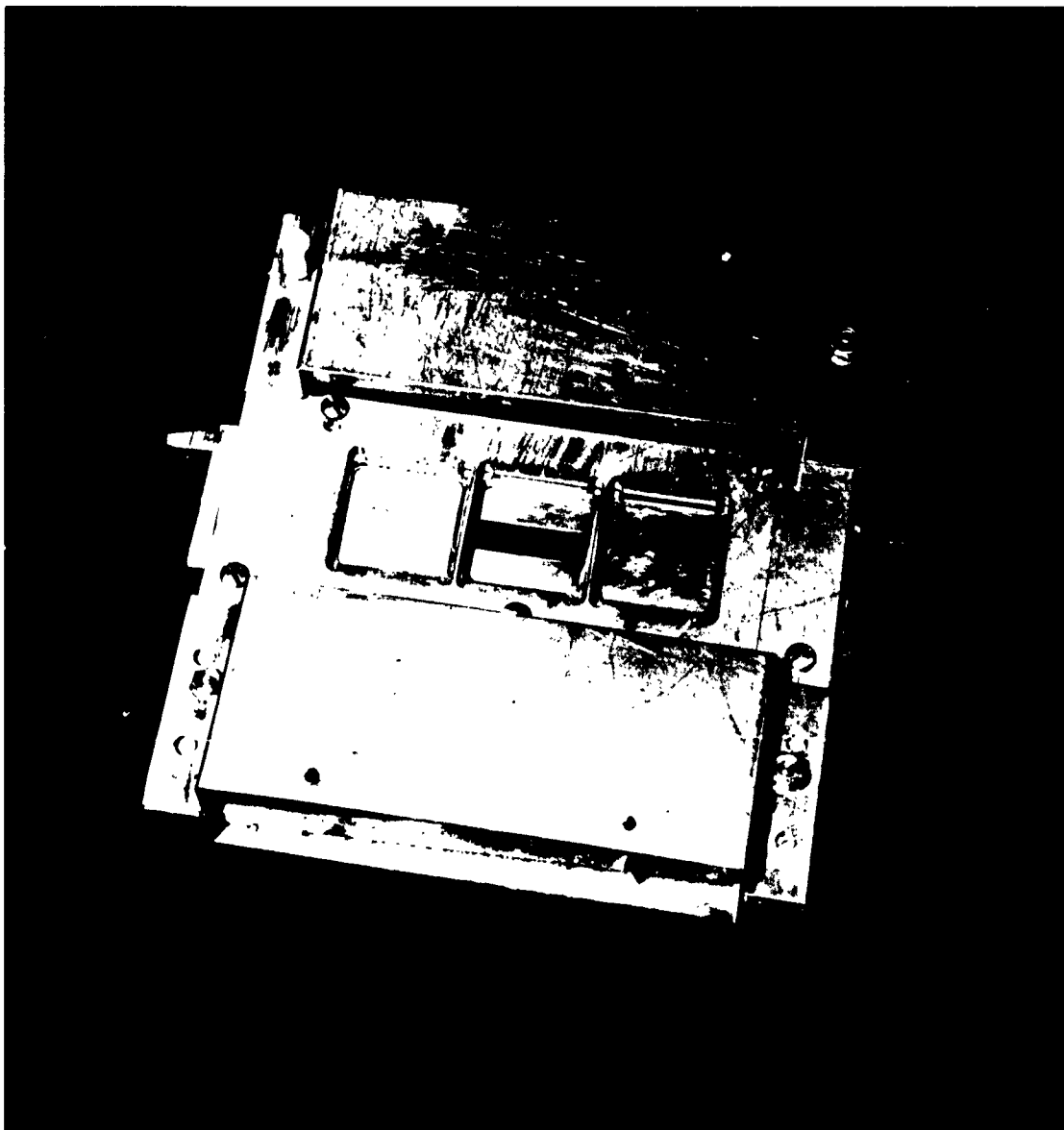


Figure 3-5a. Mask Position During Victawet Evaporation.

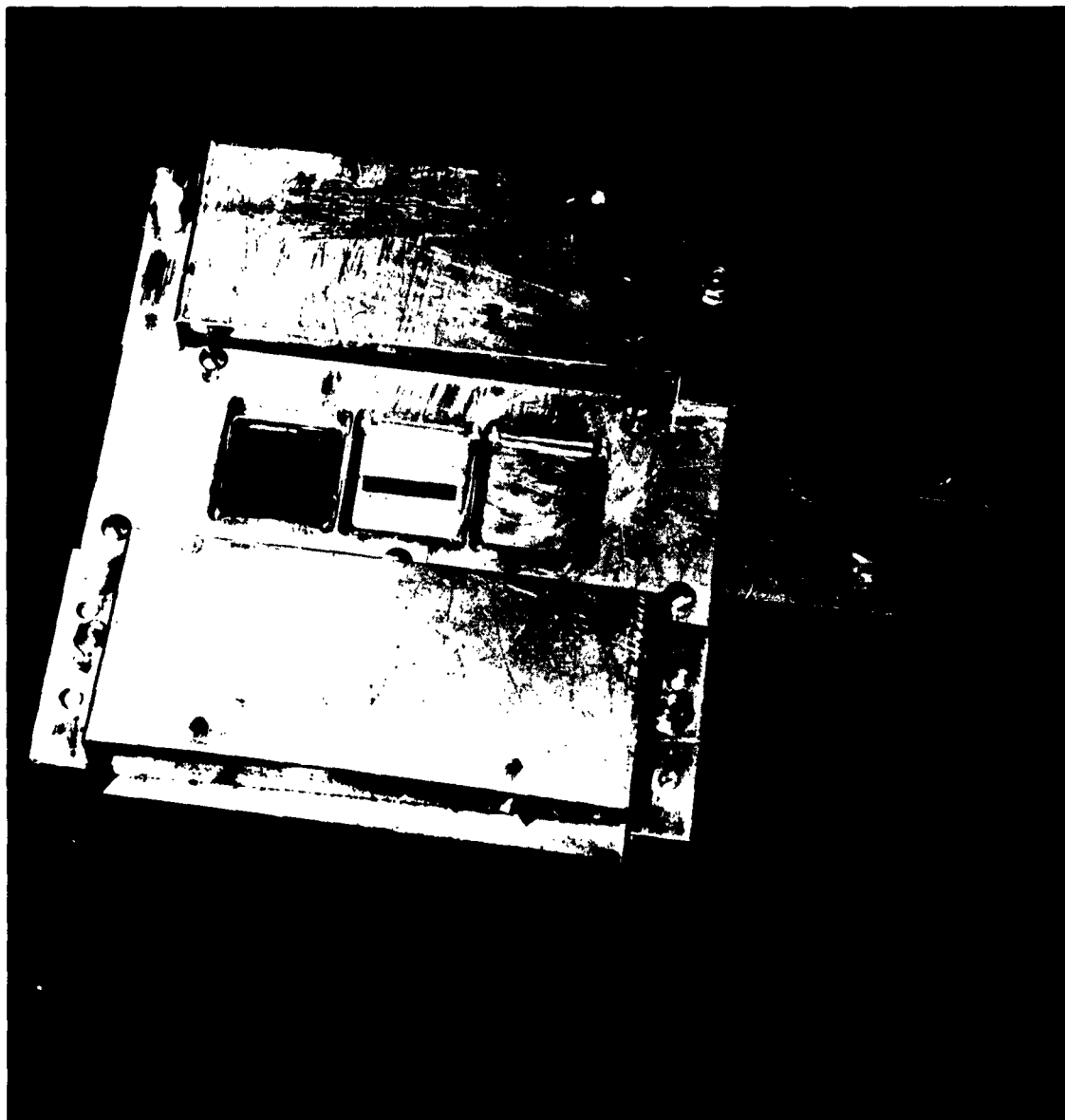


Figure 3-5b. Mask Position During Magnetic Film Evaporation.

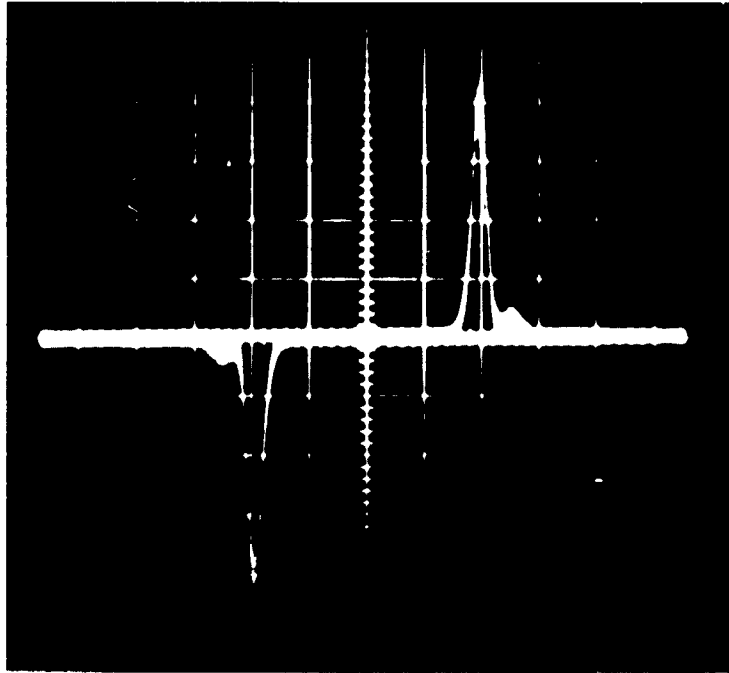


Figure 3-6a. Switching Signal of Victawet Undercoated Film -Easy Axis Switching.

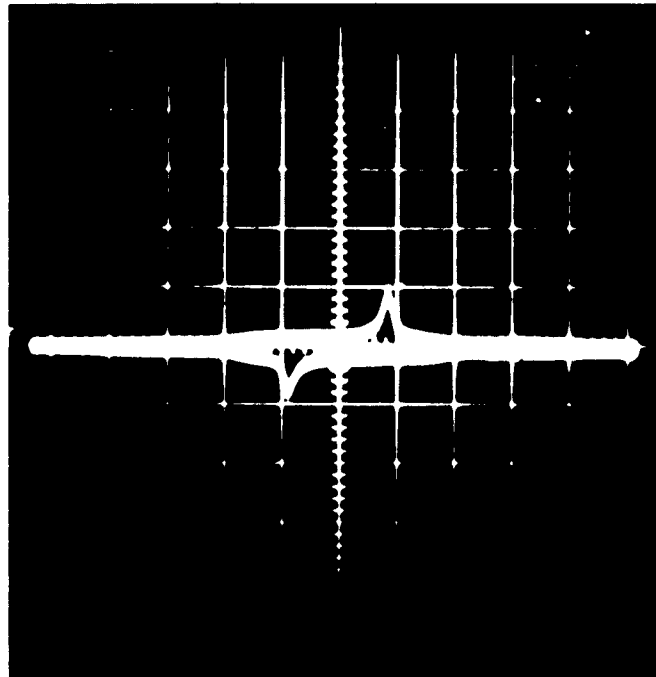


Figure 3-6b. Switching Signal of Victawet Undercoated Film - Hard Axis Switching.



Figure 3-7. Electron Micrograph of Film Segment Floated off Victawet-Coated Substrate. (200 Mesh-Grid)

### 3.4 Conclusions

Magnetization distributions in films are easily studied by electron microscopy wherein magnetization ripple<sup>(2)</sup> makes direct observation of magnetization direction possible. Direct preparation of films on specimen grids is unsatisfactory due to (1) difficulty of obtaining relatively sharp film edges, (2) unfavorable film parameters obtained, and (3) difficulty of making hysteresis and wall motion observations on such small specimens.

It has been found that coating a substrate with Victawet before film deposition enables the film to be easily floated off the substrate in a water bath. By using appropriate substrate temperatures and deposition rates films deposited on Victawet can be obtained with properties comparable to those of films deposited directly on glass. These films are relatively large and can be easily examined in hysteresis curve or wall motion apparatus before being broken up into electron microscope specimens.

Specimens with relatively sharp edges can be obtained by this floating-off and breaking-up technique. A study of magnetization distributions at film edges using this method of preparation will be undertaken.

### Bibliography

1. LFE Annual Report No. 570-A2, pg 58 - 59.
2. H. W. Fuller and M. E. Hale, J. Appl. Phys. 31, pp 238 - 248 (1960).

## 4. MAGNETIC FIELD APPARATUS FOR ELECTRON MICROSCOPY

### 4.1 Introduction

The quantitative study of magnetization switching processes in thin films requires means for observing magnetization changes as well as a means for applying a known field to a film that is adjustable in direction and magnitude. The Philips EM75B electron microscope has proved to be a valuable instrument for observing magnetization distributions in thin films, and it was desired to equip the instrument with precise field generating apparatus. A switching field in early studies was produced by a component of the objective lens field in the tilted plane of the thin film specimen,<sup>(1)</sup> but this field was uncalibrated in magnitude, and uncontrollable in direction. A large field, furthermore, was produced perpendicular to the film. Later studies utilized a rotatable soft iron yoke as an electromagnet, but the field was non-uniform, and its magnitude was non-linearly and hysteretically related to the energizing current; the dipolar field produced large beam deflections, furthermore, that necessitated large continual adjustment of the specimen position with changes in field magnitude.<sup>(2)</sup>

The principle design objectives for the new field-generating apparatus were:

- (a) Uniform field in plane of film adjustable in magnitude and direction;
- (b) Capable of precise calibration, and magnitude of quadrature field components linearly related to energizing current;
- (c) Ability to rotate direction of constant-magnitude field;
- (d) Minimal image deflection with change in field magnitude.

The chosen design consists of two pairs of coils producing quadrature fields. Each pair produces a quadrupole field that would in principle not deflect the electron beam at all. In practice a small deflection of one grid opening for each one or two oersteds of field occurs; the residual deflection is useful for rapidly determining the direction of the applied field (deflection is perpendicular to the field direction).

### 4.2 Field Generating Coils

4.2.1 Theory of Coil Design. Since space inside the microscope was limited (with objective pole pieces removed) it was decided to make each coil of only one turn of wire. The geometry of the coil pair is shown in Fig. 4-1, and for this configuration the magnetic field at a

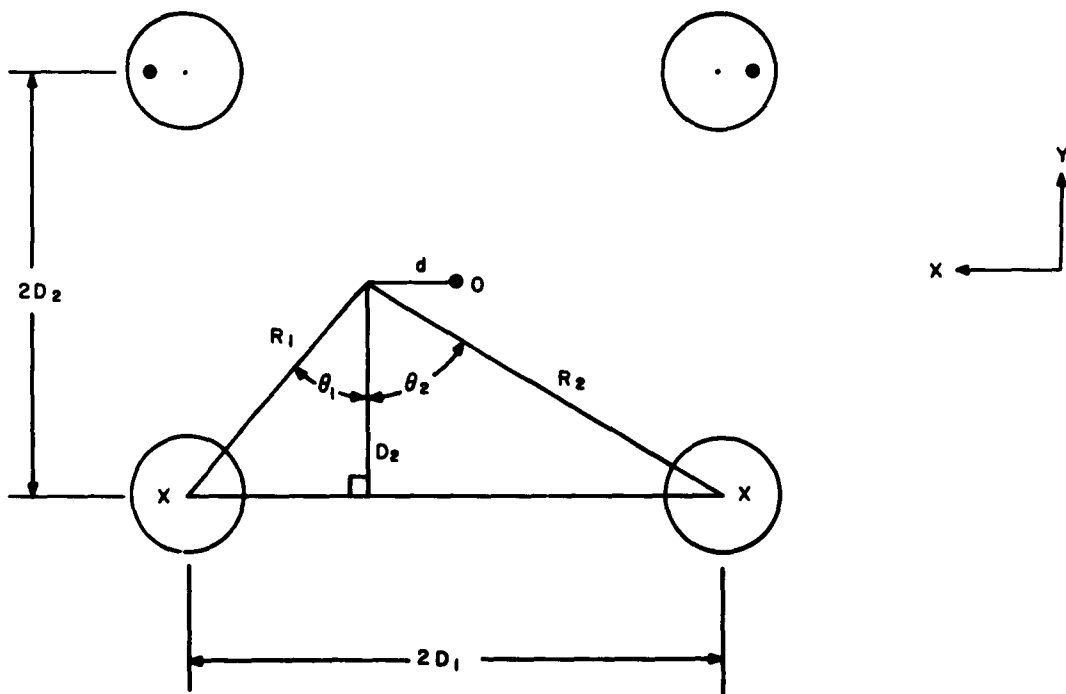


Figure 4-1. Cross-Section Geometry of Field-Generating Coil.

point a distance  $d$  from the center point (0) is in the plane of the film ( $y = 0$ ). It is assumed that the length of the four wires is much greater than  $D_1$  or  $D_2$ .

The following relations are evident by reference to Fig. 4-1:

$$\begin{aligned} D_2^2 + (D_1 - d)^2 &= R_1^2 ; \\ D_2^2 + (D_1 + d)^2 &= R_2^2 . \end{aligned} \quad (4-1)$$

Also:

$$\begin{aligned} \cos \theta_1 &= D_2/R_1 ; \\ \cos \theta_2 &= D_2/R_2 . \end{aligned} \quad (4-2)$$

By symmetry it is clear that the  $y$  component of the field along the line  $y = 0$  is zero, and thus only an  $x$  component of field from the four wires acts on the film.

We may thus write

$$H = 2I/2\pi R_1 \cos \theta_1 + 2I/2\pi R_2 \cos \theta_2 , \quad (4-3)$$

and using Eq. 4-2,

$$H = \frac{ID_2}{\pi} (1/R_1^2 + 1/R_2^2) . \quad (4-4)$$

Using Eq. 4-1 in Eq. 4-4 gives the result

$$H(d) = \frac{ID_2}{\pi} \left[ \frac{2(D_1^2 + D_2^2 + d^2)}{(D_1^2 + D_2^2) + 2d^2(D_2^2 - D_1^2) + d^4} \right] . \quad (4-5)$$

At the center position ( $d = 0$ ),

$$H(0) = \frac{2I}{\pi} \frac{D_2}{(D_1^2 + D_2^2)} . \quad (4-6)$$

Letting  $D_2 = D$ , and  $D_1 = \alpha D$ , Eq. 4-6 becomes

$$H(0) = \frac{2I}{\pi} \frac{1}{D(1+\alpha^2)} \quad (4-7)$$

Due to the physical size of the wires the two pairs of coils must be made with different cross-sections. It is desired, however, to make  $H(0)$  the same for both, i.e.,

$$D(1+\alpha^2) = \text{constant} \quad (4-8)$$

For coil (a) let  $D = 0.25$  cm,  $\alpha = 1$ ; then  $D(1+\alpha^2) = 0.50$ . For coil (b) let  $D = 0.40$  cm, so that  $0.40(1+\alpha^2) = 0.50$ , or  $\alpha = 0.5$ . Thus for coil (a),  $D_1 = D_2 = 0.25$  cm, while for coil (b),  $D_2 = 0.40$  cm,  $D_1 = 0.20$  cm.

The width of the electron beam in the microscope is 0.10 cm at maximum. Thus the maximum variation in the field can be determined by calculating  $[H(0.05) - H(0)]/H(0)$ , which is 2% for coil (a), the worst case of the two.

Using Eq. 4-7 and the coil dimensions previously given,

$$H(0)/I = \frac{2}{\pi} \frac{1}{0.5 \times 10^{-3}} \frac{4\pi}{10^3} \frac{\text{oe}}{\text{amp}} = 1.6 \frac{\text{oe}}{\text{amp}} \quad (4-9)$$

To verify the theoretical value given by Eq. 4-9, a Bell Hall-Pak BH-202 Hall effect probe has been purchased. After suitable mounting this probe will be used to measure the field inside the quadrature coil form.

**4.2.2 Description of Coils and Assembly.** It was decided to use wire of 0.055 inches diameter so as to have a minimum of heating at currents up to 10 amperes. The coil forms were machined out of two pieces of bakelite (see Figs 4-2 and 4-3) and fitted together (see Fig. 4-4). U-shaped wire segments were carefully bent to the correct dimensions and placed on the form. Small pieces of wire were placed in the diagonal end slots and soldered in place to form the pair of coils. The entire form was then dipped in a resistance paint and baked dry. This was done to reduce effects due to surface charge in the electron microscope. Thin-walled aluminum tubes were also fitted along the electron-beam path to further reduce these effects.

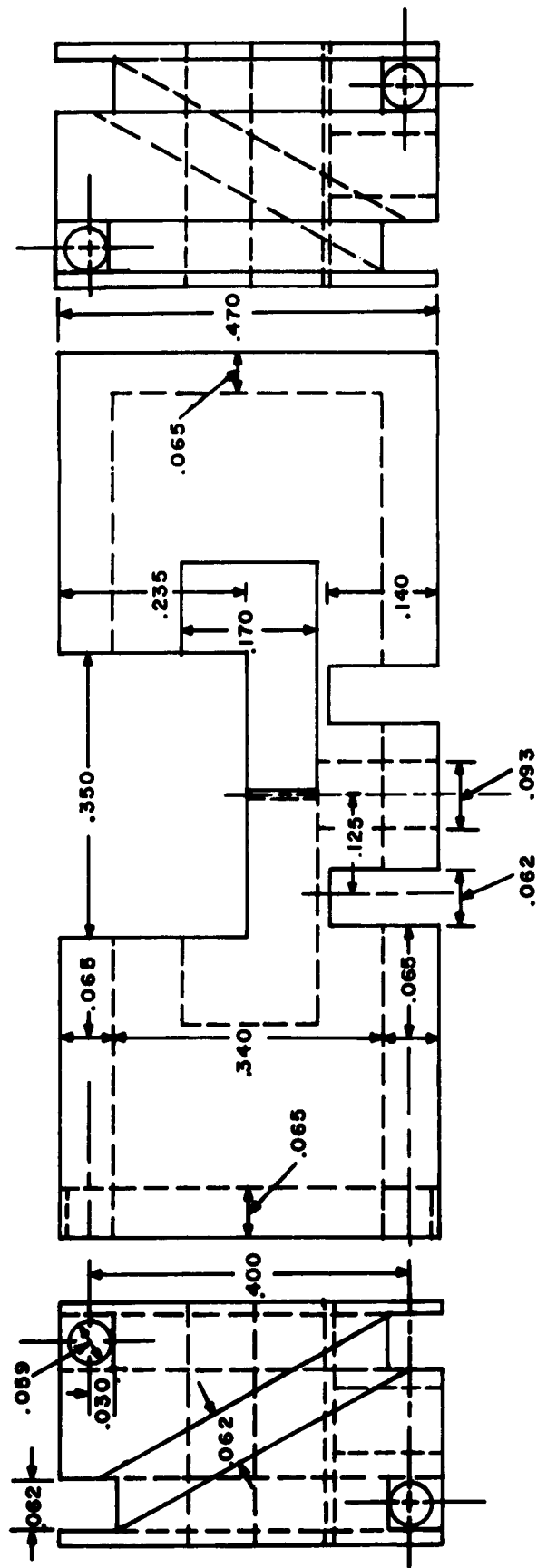
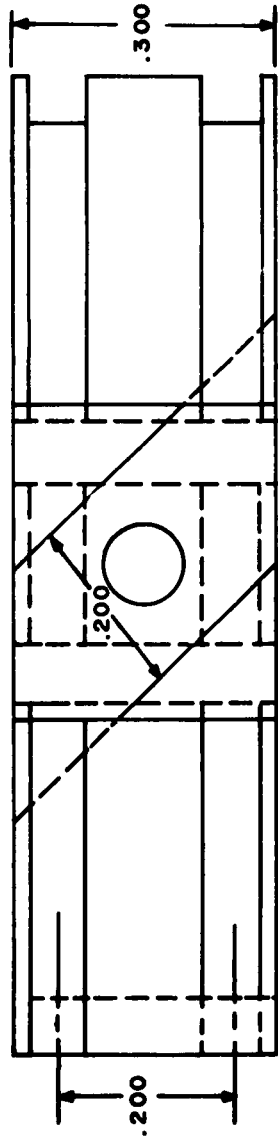


Figure 4-2a. Mechanical Drawing of Half of Coil Form. ALL DIMENSIONS  $\pm .002$

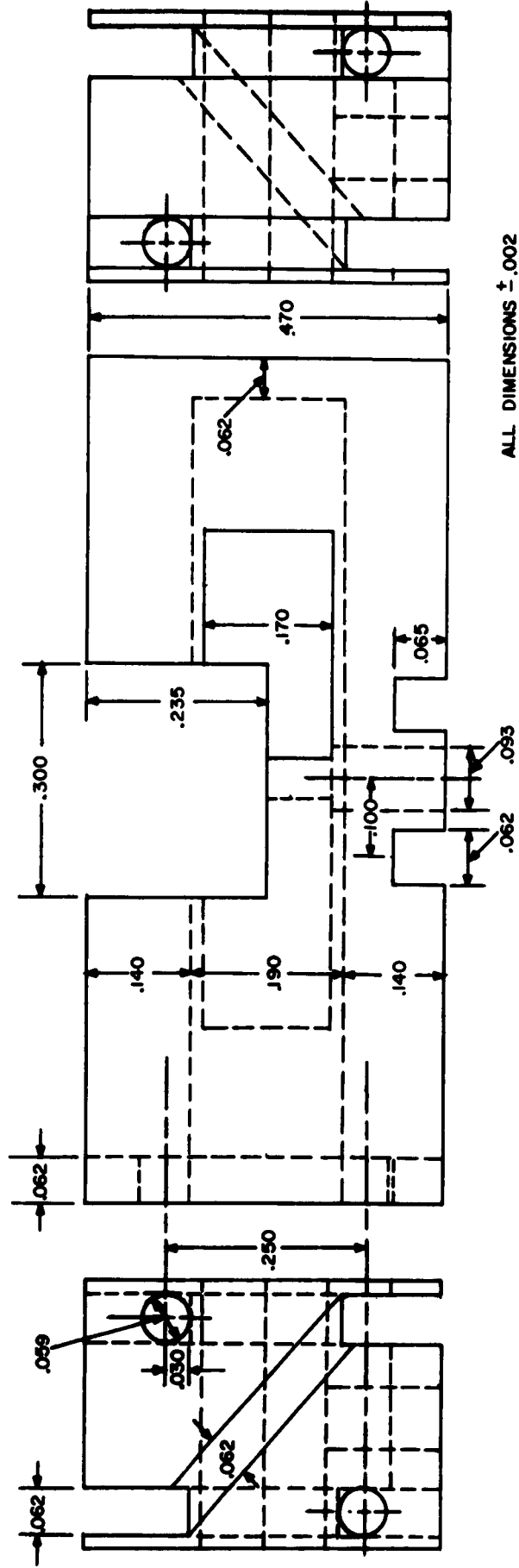
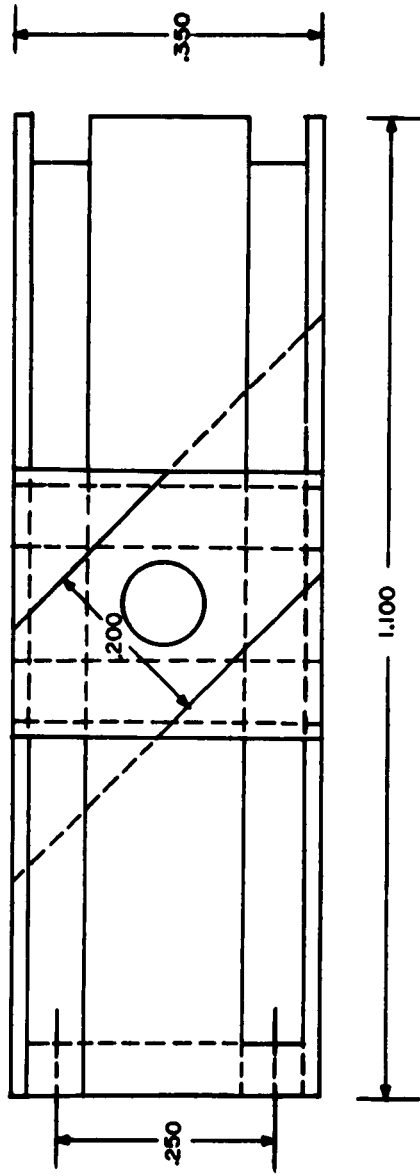


Figure 4-2b. Mechanical Drawing of Half of Coil Form.

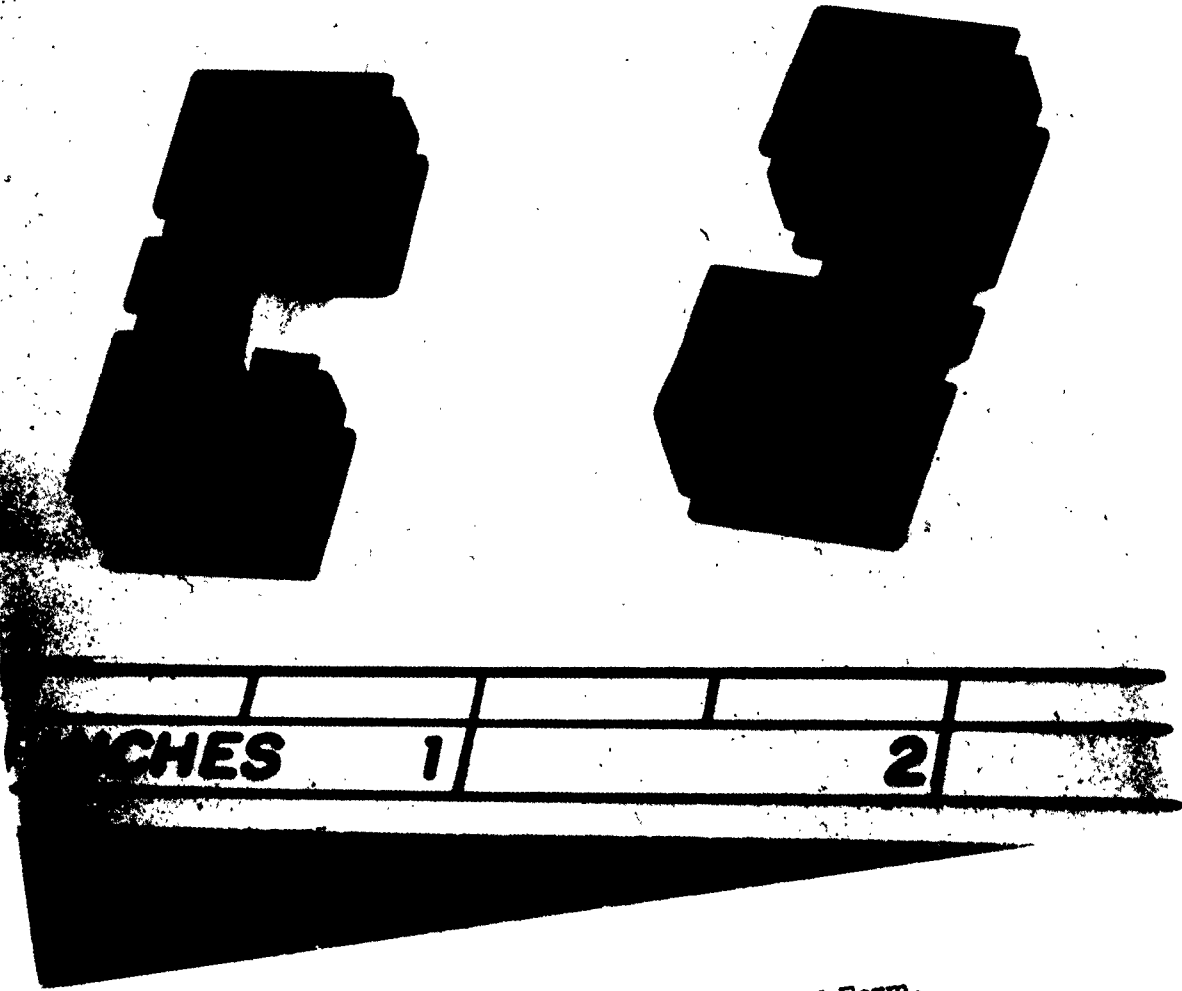


Figure 4-3. Segments of Bakelite Coil Form.

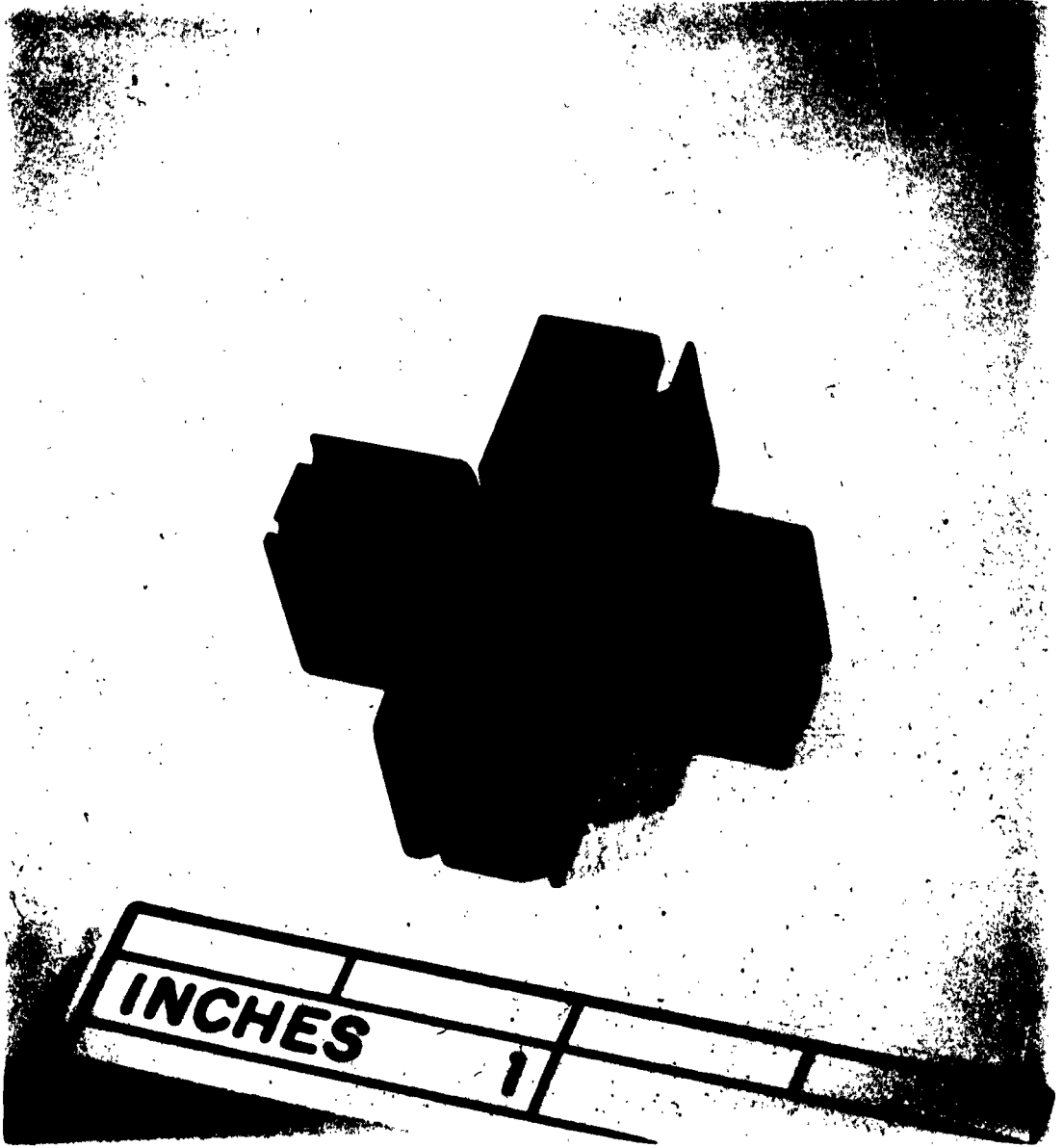


Figure 4-4. Assembled Coil Form .

The coils were placed in the specimen chamber of the electron microscope and carefully oriented. They were held in place by two friction rings which were machined to fit snugly against the circular chamber walls.

The four current lead-in wires were brought into the specimen chamber by drilling a hole through the chamber wall. Four single-lead vacuum seals were soldered, with the wires attached, into a special header to effect a vacuum-tight seal. The lead-in wires were then soldered to the previously positioned field coils. This completed the assembly of the field generating apparatus inside the electron microscope.

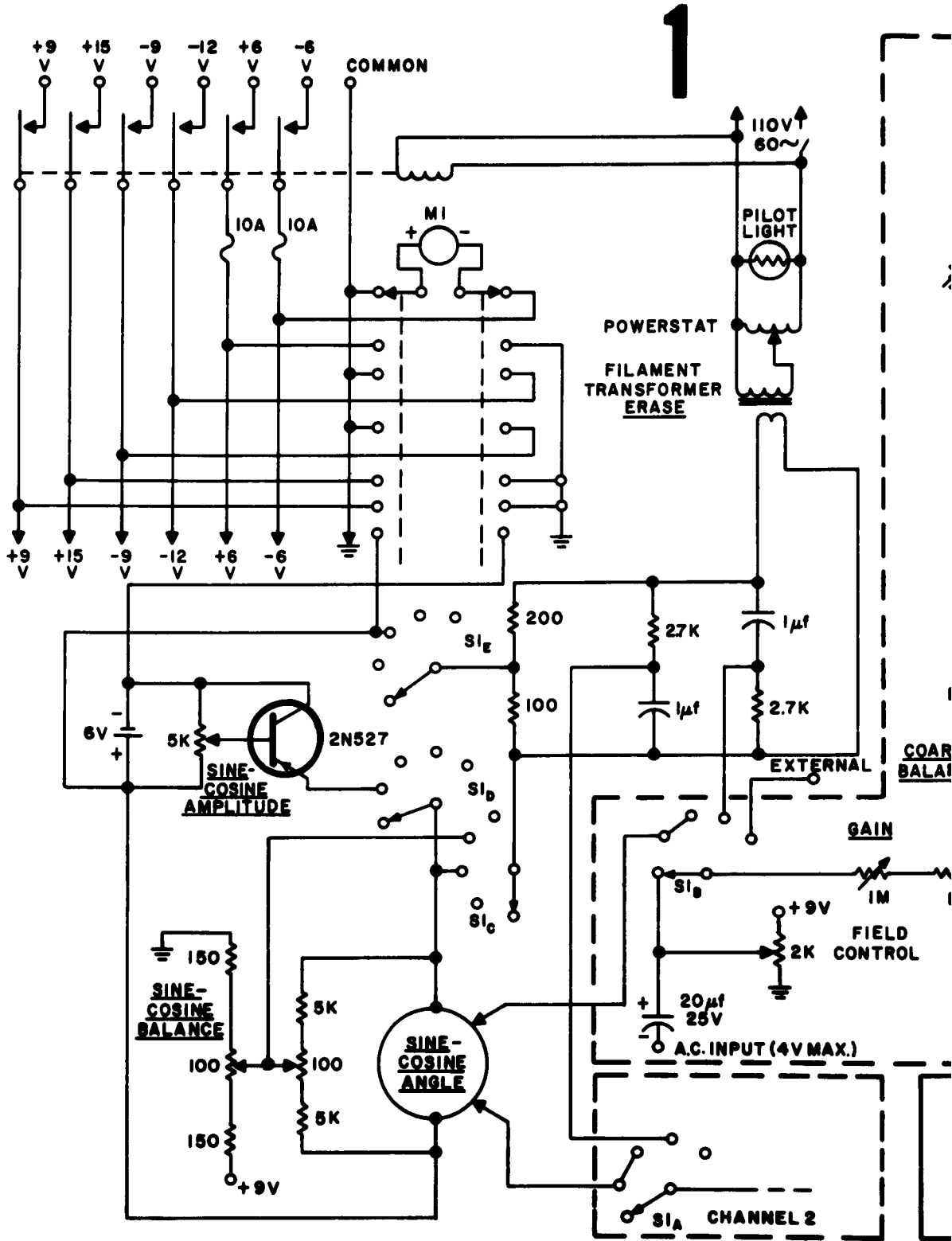
#### **4.3 Current Supply For Field-Generating Coils**

**4.3.1 Specifications.** The current supply for the field-generating coils was designed to furnish the following functions:

- a) Manual control of each coil current independently;
- b) Sine-cosine control of the coil pair such that the angle and magnitude of the magnetic field can be varied independently;
- c) An a.c. linear erase wherein both coils are fed in phase, with both angle and peak value of field independently controlled;
- d) An a.c. circular erase wherein the coils are fed 90° out of phase with the field amplitude variable;
- e) A d.c. plus a.c. ripple input function with independent control of the d.c. level and a.c. ripple;
- f) An external input where any other desired function generator can be connected.

**4.3.2 Circuit Design.** The overall circuit design is shown in Fig. 4-5. The circuit is composed of the following main elements:

- a) A multiple-control relay operated by a 110V coil that connects the transistor supply voltages to the circuit;
- b) A powerstat control and filament transformer to supply low voltage a.c. to the phase shifter and sine-cosine angle control.
- c) A phase shifter to supply two a-c signals of equal amplitude but 90° out of phase, to the dual amplifiers;
- d) A floating 6V battery to supply the sine-cosine angle control through a potentiometer and a 2N527 transistor;
- e) A sine-cosine angle control to enable generating a constant magnitude magnetic field at any angle (the control is a Computer





Instruments Corp. sine-cosine potentiometer #6974-24, with a resistance of 10K. It is paralleled with a voltage divider that enables setting the voltage so as to drive the dual amplifiers equally);

f) A five-position multi-gang switch that enables choosing one of five modes of operation. These are:

- 1) Manual: Allows independent control of each amplifier with a.c., d.c., or a combination as an input signal.
- 2) Sine-cosine: Allows independent control of field direction and amplitude, d.c. input.
- 3) Linear-erase: Allows independent control of field direction and amplitude, a.c. input.
- 4) Circular erase: Allows rotating magnetic field of controllable amplitude.
- 5) External: Allows any other signal to be applied to the input stage of the amplifier.

g) Dual d.c. amplifiers, each consisting of the following circuitry:

- 1) Three stages of current amplification by NPN transistors connected as single-ended emitter-followers. The input to the base of the input transistor is by means of a current divider network whereby the overall gain of the amplifier is controlled. Part of the current-divider network is a feedback loop from the emitter of the third stage to the base of the first. This feedback loop serves two purposes; it improves system linearity and provides a convenient method of balancing the push-pull driver stage that follows.
- 2) A push-pull driver stage consisting of a pair of complementary transistors. The transistor bases are connected to the emitter of the third single-ended stage by a resistive phase divider network.
- 3) A power stage consisting of two PNP tetrodes, each connected as an emitter-follower and driven respectively by the emitter and collector of the complementary drivers. Tetrodes are used to obtain improved linearity and low leakage current with the transistor in its cut-off state. They are also useful in equalizing the gain of the push-pull stages, as varying the biasing resistor on the back-biased base changes the gain of the tetrode.

**4.3.3 Circuit Operation.** Testing of the dual power supply revealed several design flaws in the preliminary design which were corrected. The supply was then calibrated and tested for linearity. The linearity was found to be within 3% up to 2 amp. current (see Fig. 4-6a) and within 10% at 4 amp. current (see Fig. 4-6b). This is felt to be adequate for present purposes.

#### **4.4 Conclusions**

An apparatus for producing controlled magnetic fields in the electron microscope has been designed and built. A power supply capable of supplying the field coils with current for various modes of operation has also been designed and constructed.

Preliminary tests on magnetic films in the electron microscope using the new field equipment proved to be satisfactory. It was possible to nucleate and move domain walls controllably. It is planned to use the externally controlled field to study edge effects <sup>(3, 4)</sup> and partial switching <sup>(5)</sup> in thin magnetic films.

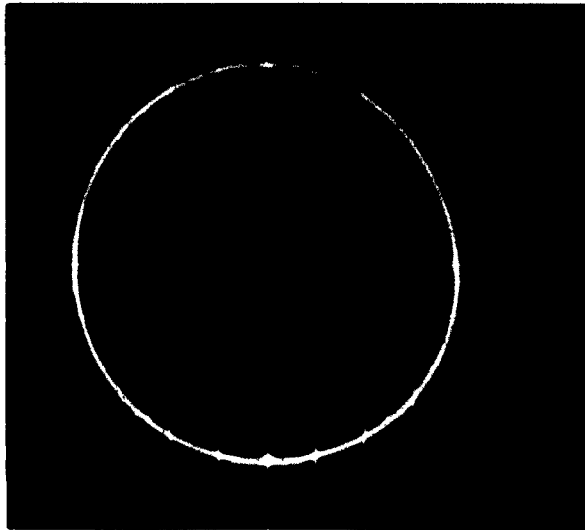


**Figure 4-6a. Dual Amplifier Output - Circular Erase Mode.  
(One Div. = One-Half Amp.)**

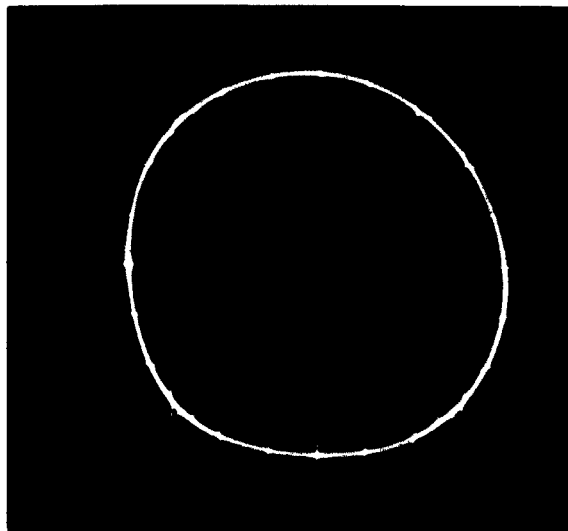


**Figure 4-6b. Dual Amplifier Output - Circular Erase Mode.  
(One Div. = One Amp.)**

### Bibliography

1. H. W. Fuller and M. E. Hale, J. Appl. Phys. 31, 238 (1960).
2. LFE Report No. 590-A1, Section 6.8.
3. LFE Report No. 570-A3, Chap. II.
4. LFE Report No. 570-A4, Chap. II.
5. LFE Report No. 570-A4, Chap. V.

## 5. PARTIAL SWITCHING IN THIN FILMS

### 5.1 Introduction

The switching process in magnetic thin films possessing uniaxial anisotropy is, generally speaking, a complex one. It may, however, be broken down into two broad categories: sequential processes and rotational processes. Neither of these types of processes necessarily govern the switching behavior of a given film for all values of switching field magnitude and angle. It has been found in many films that the switching process may be best considered as a combination of elements of the rotational and sequential models. Examples of rotational-sequential combinations have been reported in the literature when the switching field is in the easy and/or hard direction.<sup>(1, 2)</sup> In this chapter evidence will be presented to show that a rotational-sequential process may also occur when the switching field is oblique to the film's easy axis. A theoretical model of the process will be presented and experimental evidence generally confirming the theoretical expressions will be shown.

The model to be presented will, in general, yield a hysteresis loop of the type shown in Fig. 5-1. The first (or partial) switch is a rotational one with regions of the film switching rotationally. These regions alternate with unswitched regions as shown in Fig. 5-2. This sequence of switched and unswitched domains occurs because of the angular dispersion of the easy axis. The large demagnetizing fields that occur when the rotational switch takes place forces the magnetization in the unswitched domains to rotate back toward the easy axis.<sup>(3)</sup> The state thus formed is similar in many respects to the hard-axis remanent state.<sup>(1)</sup> The remaining unswitched magnetization is switched sequentially when the switching field is further increased. The two ways in which this may occur are shown in Fig. 5-3 and Fig. 5-4.

### 5.2 Theoretical

5.2.1 Rotational Model. In the model to be discussed, the switching mechanism will consist of rotational and sequential phases. The pure rotational switching model has been discussed rather fully in the literature.<sup>(4, 5)</sup> However, it may be best to present certain aspects of this theory in detail and then show where the rotational-sequential or partial switching model departs from the pure rotational one.

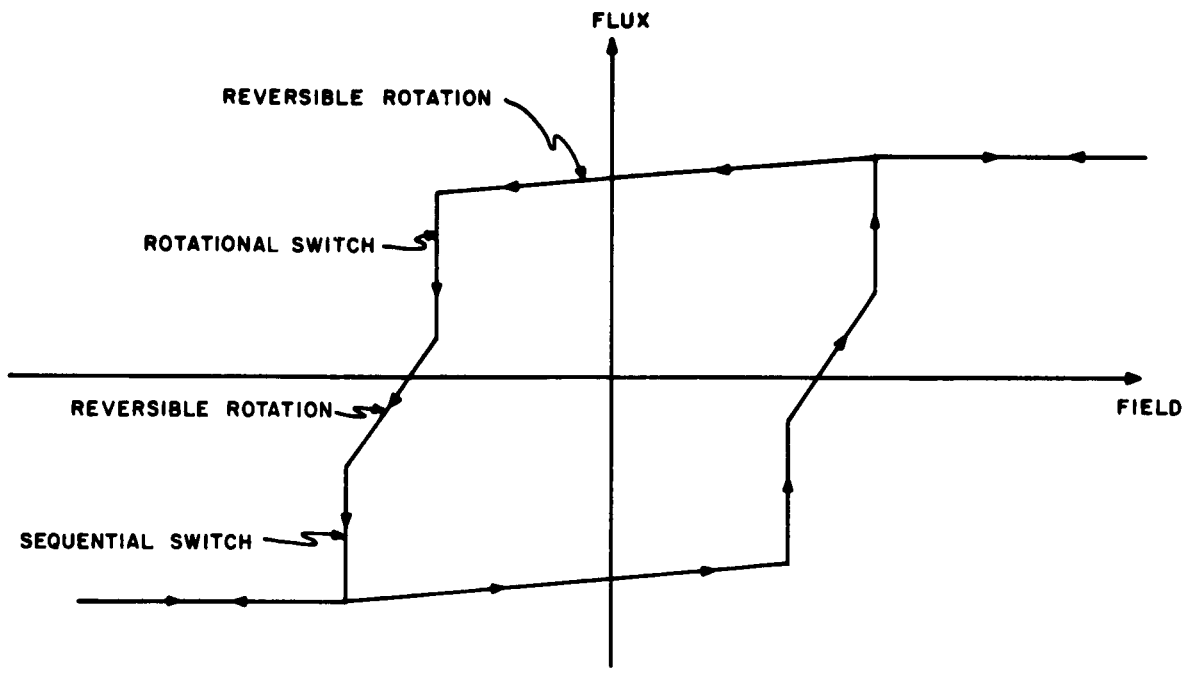


Figure 5-1. Idealized Rotational-Sequential Hysteresis Loop.

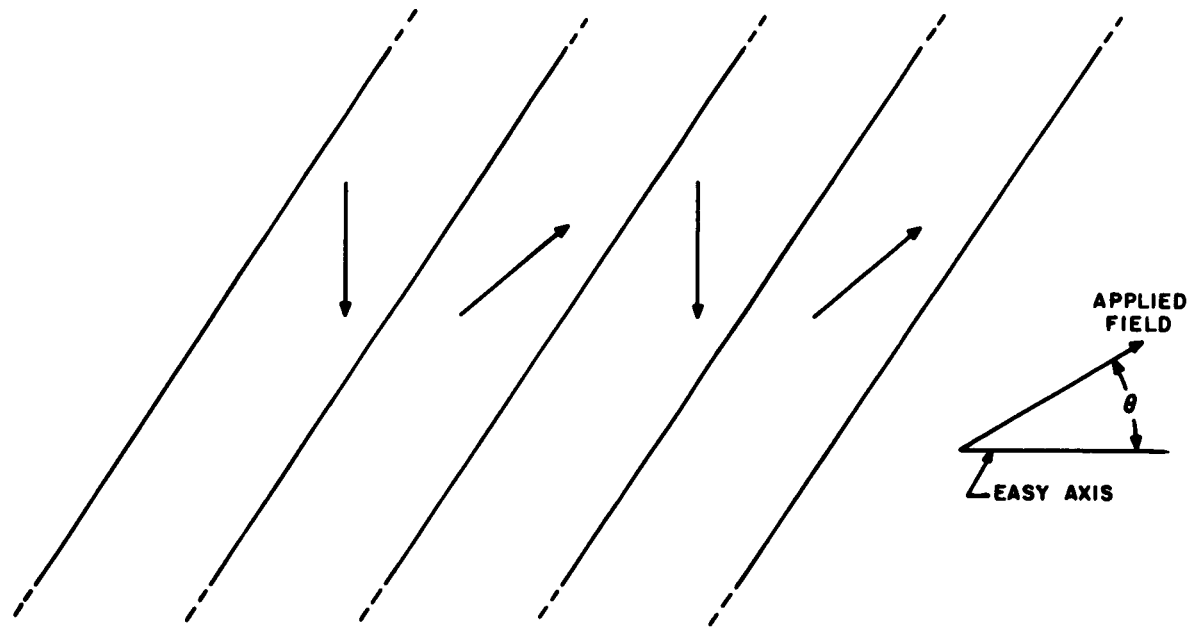


Figure 5-2. The Partially Switched State. (Arrows Indicate Magnetization Direction)

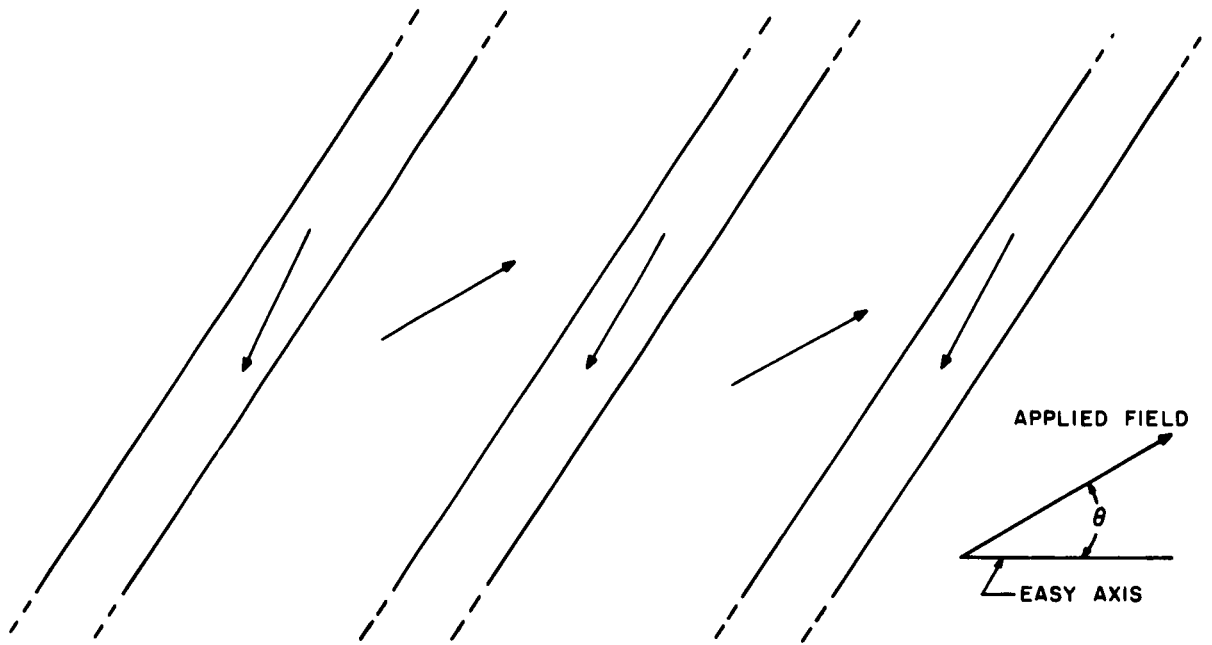


Figure 5-3. Sequential Switching of Partially Switched State by Motion of Partial Switching Walls. (Arrows Indicate Magnetization Direction)

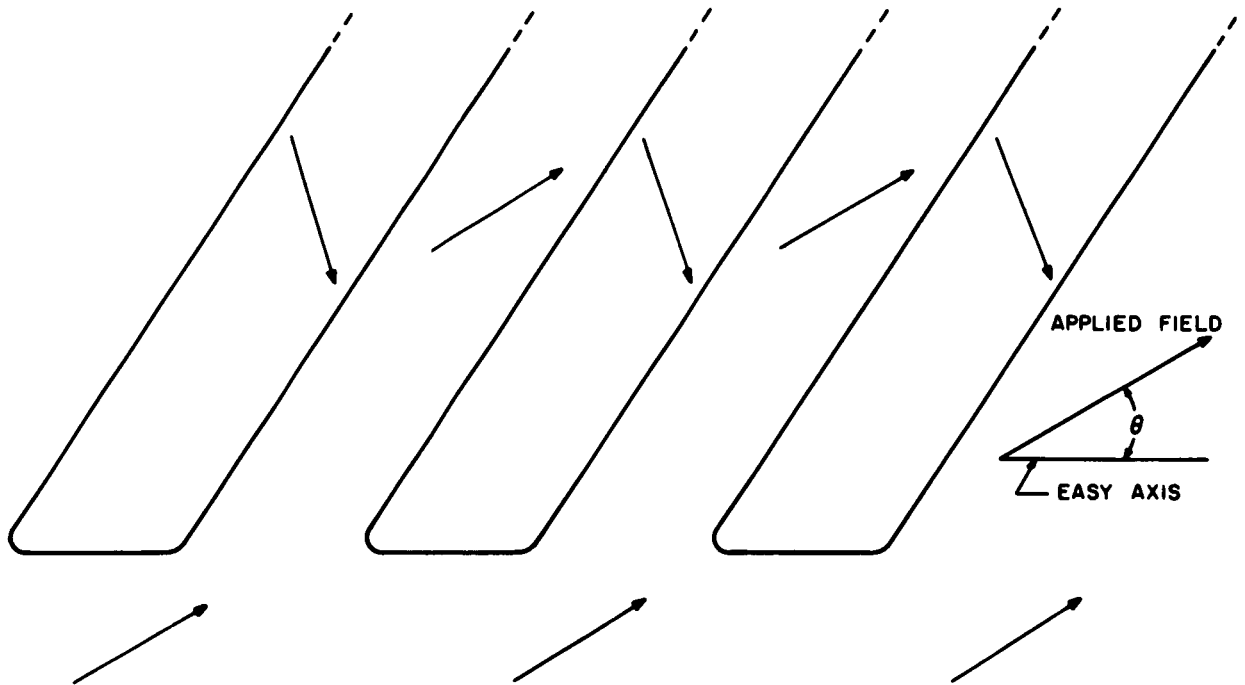


Figure 5-4. Sequential Switching of Partially Switched State by Easy Direction Wall Motion. (Arrows Indicate Magnetization Direction)

The basic elements of the pure rotational model are shown in Fig. 5-5. The switching field is applied at an angle of  $(180^\circ - \theta)$  to the easy direction in which the magnetization would lie with no applied field. As the applied field is increased in magnitude the magnetization rotates away from the easy direction toward the applied field in a coherent mode. At a certain value of applied field, depending only on the anisotropy and magnetization constants, there will be a sudden and irreversible switch of the magnetization past the hard direction. The relation desired is that between the switching field angle and magnitude when the irreversible rotation occurs.

The energy per unit volume,  $E$ , is composed of anisotropy and magnetostatic terms and may be written as

$$E = K \sin^2 \phi + MH \cos (\theta + \phi) , \quad (5-1a)$$

where  $K$  is the anisotropy constant,  $M$  is the magnetization,  $H$  is the applied field,  $\phi$  is the acute angle between the magnetization and the easy axis, and  $\theta$  is the acute angle between the applied field and the easy axis.

The irreversible rotation will occur when<sup>(5)</sup>

$$\left. \frac{\partial E}{\partial \phi} \right]_{\phi = \phi_0, H = H_r} = \left. \frac{\partial^2 E}{\partial \phi^2} \right]_{\phi = \phi_0, H = H_r} = 0, \quad (5-1b)$$

where  $\phi_0$  and  $H_r$  are the values of magnetization angle and applied field magnitude respectively when the switch occurs. Differentiating Eq. 5-1a, setting  $\phi = \phi_0$  and  $H = H_r$ , and equating to zero yields

$$K \sin 2 \phi_0 - M H_r \sin (\theta + \phi_0) = 0 , \quad (5-2a)$$

and

$$2K \cos 2 \phi_0 - M H_r \cos (\theta + \phi_0) = 0 . \quad (5-2b)$$

Transposing and dividing Eq. 5-2a by Eq. 5-2b yields

$$\tan 2 \phi_0 = 2 \tan (\theta + \phi_0) . \quad (5-3)$$

Using appropriate trigonometric substitutions, Eq. 5-3 becomes

$$\tan \phi_0 = (\tan \theta)^{1/3} . \quad (5-4)$$



Figure 5-5. The Rotational Model.

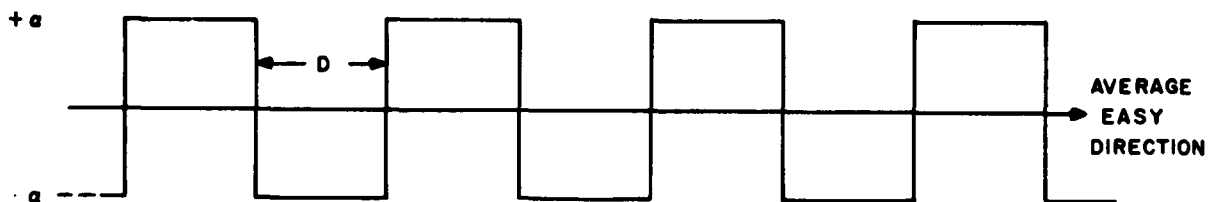


Figure 5-6. Idealized Variation of the Direction of the Easy Axis.

Substituting Eq. 5-4 into Eq. 5-2 and using various trigonometric identities yields

$$(H_k/H_r)^{2/3} = \cos^{2/3} \theta + \sin^{2/3} \theta , \quad (5-5)$$

where  $H_k$  is the rotational coercive force and is equal to  $2K/M$ . Equation 5-5 is the desired relation between the applied field angle and magnitude when the irreversible rotation occurs.

**5.2.2 Modification of Rotational Model.** The main film parameter that makes a modification of the rotational model necessary is the angular dispersion of the easy axis. For model purposes this dispersion will be assumed to have a square-wave distribution of wavelength  $2D$  in the easy direction with a magnitude of  $\alpha$  as shown in Fig. 5-6. This easy-axis dispersion means that the applied field angle  $\theta$  given in Eq. 5-5 is no longer constant over the entire film. If  $\theta$  is defined more generally as the angle between the applied field and the average easy axis, then the actual angle between the field and the easy axis is  $(\theta + \alpha)$  and  $(\theta - \alpha)$  in alternate regions of the film. The easy-axis dispersion thus appears quantitatively as a variation of the applied field angle. This in turn affects the magnitude of the applied field at which switching will occur. This modification of the rotational model is shown in Fig. 5-7 wherein Eq. 5-5 is plotted and the effect of easy-axis dispersion on switching field magnitude is shown.

Two possible cases are shown in Fig. 5-7, depending on whether  $\theta > 45^\circ$  or  $\theta < 45^\circ$ . For  $\theta < 45^\circ$  the  $(\theta + \alpha)$  state would switch at a lower applied field magnitude while for  $\theta > 45^\circ$  the  $(\theta - \alpha)$  would switch at a lower magnitude of applied field. It should be noted here that partial switching does not occur for all values of  $\theta$ . Whenever the wall motion coercive force  $H_w$  is less than the rotational coercive force  $H_r$  the complete switching process will be a sequential one. For  $\theta = 0^\circ$ ,  $H_w$  is equal to  $H_c$ , the easy-direction wall-motion coercive force. It is not, however, equal to  $H_c$  for all values of  $\theta$ . A minimum switching angle  $\theta_c$  may be defined as that angle below which the switching process will be a sequential one and above which it will be a partial rotational one. The crossover between switching processes is shown in Fig. 5-7. Figure 5-7 also indicates that the easy-axis dispersion lowers the magnitude of the switching field below the rotational switching threshold of the coherent mode.

Actually many of the predictions given in the preceding paragraph are incorrect. The main reason for this is that the demagnetizing fields that occur when the irreversible rotation starts to take place have not been included in the modified model.

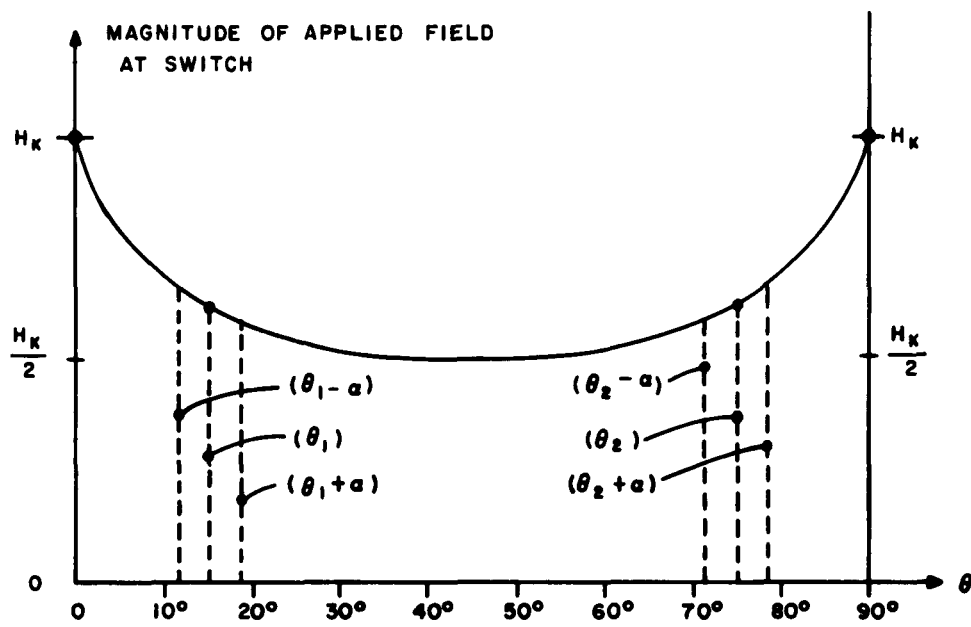


Figure 5-7. Magnitude of Rotation Switching Field as a Function of the Angle Between the Field and the Local Easy Axis. (Case 1:  $0 < 45^\circ$ , Case 2:  $0 > 45^\circ$ )

The effect that the demagnetizing field will have on the rotational part of the switching process depends mainly on  $n = (l/d)$ , the number of walls/unit length created by the switching process. The distance  $d$  is the wall spacing. The partial switching process will be somewhat different for relatively large or small  $n$ .

For the case of  $\theta < 45^\circ$  the value of  $n$  does not have a very pronounced effect on the partial switching process. As stated before the  $(\theta + \alpha)$  regions will be the ones partially switched regardless of the value of  $n$ . The demagnetizing fields will be kept small, even for large  $n$ , by a counter-rotation of the magnetization in the  $(\theta - \alpha)$  regions. The effect of large  $n$  will be mainly to increase the field magnitude at which the partial switch takes place.

For the case of  $\theta > 45^\circ$  the effect of  $n$  on the switching is more significant. For small values of  $n$  the effect of the demagnetizing field will be small. This indicates that the initial prediction of the  $(\theta - \alpha)$  regions being the ones partially switched should hold. In switching, however, the  $(\theta - \alpha)$  state will become coherent with the  $(\theta + \alpha)$  state. In this case, the effect of the coupling of regions by the demagnetizing field will tend to carry the  $(\theta + \alpha)$  state through an irreversible switch along with the  $(\theta - \alpha)$  state. That is, for low  $n$  and  $\theta > 45^\circ$  the switch should be essentially a full rotational one.

For large  $n$  the demagnetizing field will raise the field necessary for a partial switch of the  $(\theta - \alpha)$  state. If  $n$  is large enough the field necessary for a switch of the  $(\theta - \alpha)$  state will become greater than that necessary for a switch of the  $(\theta + \alpha)$  state. The effect of the demagnetizing field on the field magnitude necessary for the  $(\theta + \alpha)$  state to switch is less than its effect on the  $(\theta - \alpha)$  state switching field. This is due to the fact that a switch of the  $(\theta + \alpha)$  state can occur with a relatively low demagnetizing field due to the concurrent counter-rotation of the  $(\theta - \alpha)$  state. Thus for large  $n$  and  $\theta > 45^\circ$  the switch will be a partial rotational one, similar to the situation when  $\theta < 45^\circ$ .

**5.2.3 Demagnetizing Field Calculations.** Consider a film of thickness  $T$  under the conditions shown in Fig. 5-8. During and after the partial switching the walls may have a unipolar in addition to the usual dipolar charge distribution. If such a unipolar charge distribution is considered to be present the demagnetizing field due to the dipolar wall charge may be neglected. The film is considered as broken up into regions by walls spaced a distance  $d$  apart. These walls carry alternately a magnetic charge of  $\pm Q$  per unit area. To simplify the mathematical procedure, the walls will be considered as infinite sheets of

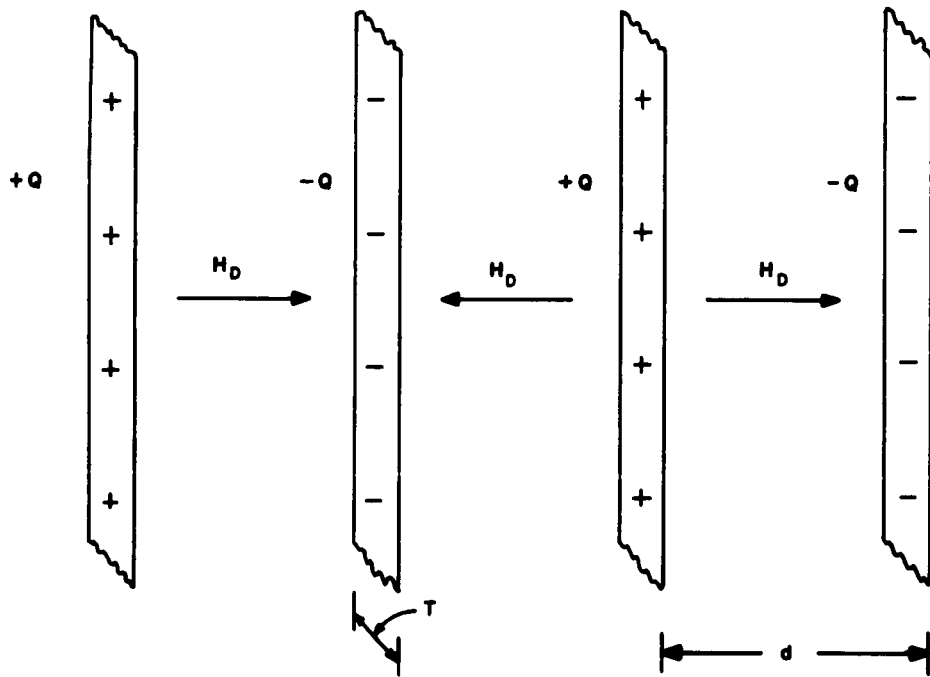


Figure 5-8. Demagnetizing Field Model.

charge for regions very close to the walls and as lines of charge elsewhere. A crossover point will be established by equating the fields resulting from these two approximations.

5.2.3.1 Infinite Sheet of Charge. The case of the infinite sheet is shown in Fig. 5-9a. Considering the Gaussian pillbox shown yields

$$H_s = \frac{1}{2} (4 \pi Q) = 2 \pi Q , \quad (5-6)$$

where  $H_s$  is the field due to the infinite sheet.

5.2.3.2 Lines of Charge. The case for lines of charge is shown in Fig. 5-9b. Considering only one line of charge yields a field  $H_l$  given by

$$H_l = 4 \pi QT / 2 \pi r = 2 QT / r , \quad (5-7)$$

where  $QT$  is the charge per unit line length and  $r$  is the distance from the line of charge.

Adding the field contributions from all the lines of charges yields the total field  $H_t$  as

$$H_t = 2 QT \sum_{k = -\infty}^{k = +\infty} \frac{(-1)^k}{kd+r} . \quad (5-8)$$

The sum in Eq. 5-8 is evaluated by the method of residues. Taking a function  $f(z)$  as

$$f(z) = \frac{1}{zd+r} = \frac{1/d}{z+r/d} , \quad (5-9)$$

the residue of  $f(z)$  at  $z = r/d$  is  $(1/d)$ .  $H_t$  is given by<sup>(6)</sup>

$$H_t = - 2 QT \text{Residue} [\pi f(z) \csc(\pi z)] ; z = \frac{r}{d} , \quad (5-10)$$

$$H_t = \frac{2 \pi QT}{d \sin(\pi r/d)} . \quad (5-11)$$

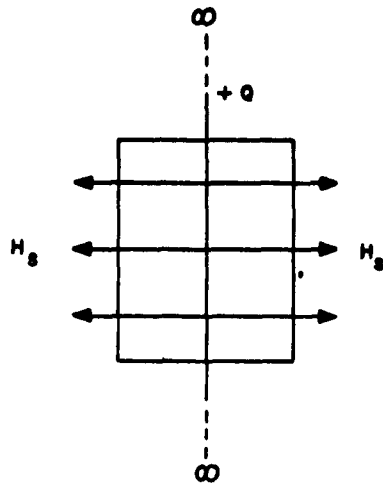


Figure 5-9a. Model for Calculation of Field of Infinite Sheet of Charge.

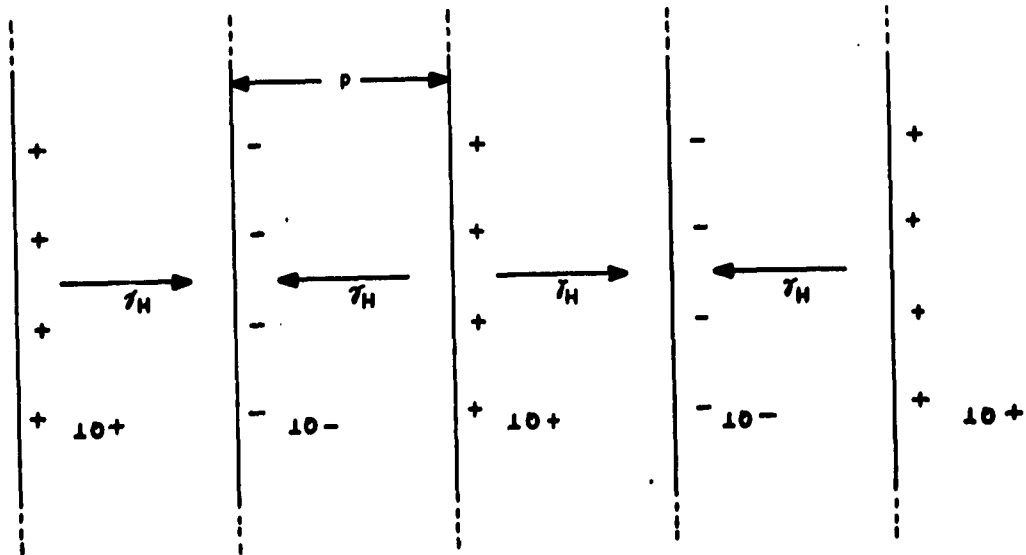


Figure 5-9b. Model for Calculation of Field of Infinite, Alternately Charged, Lines of Charge.

The crossover value,  $r = r_0$ , is found by equating Eqs. 5-6 and 5-11. This yields

$$\frac{2\pi QT}{d \sin(\pi r_0/d)} = 2\pi Q \quad (5-12)$$

Assuming  $\pi r_0/d \ll 1$  in Eq. 5-12 yields

$$r_0 = T/\pi \quad (5-13)$$

Using Eqs. 5-6, 5-11, and 5-13, the average demagnetizing field,  $H_D$ , in a region bounded by a pair of walls may be found as

$$H_D = \frac{2}{d} \int_0^{r_0} H_s dr + \int_{r_0}^{d/2} H_l dr \quad (5-14)$$

The integration yields

$$H_D = \frac{4QT}{d} \ln \frac{2ed}{T} \quad (5-15)$$

In terms of  $n = 1/d$  Eq. 5-15 becomes

$$H_D = 4nQT \ln(2e/nT) \quad (5-16)$$

The total effect of  $n$  on  $H_D$  is not completely shown by a cursory examination of Eq. 5-16.  $Q$ , the surface charge, depends on the direction of the magnetization in the domains adjacent to the wall. These magnetization directions will, in part, depend on  $H_D$ . Thus  $Q$  is itself an implicit function of  $n$ . In addition  $n$  itself will depend on the film thickness  $T$  or, inversely,  $T$  is a function of  $n$ . To emphasize these facts Eq. 5-16 may be written as

$$H_D(n) = 4nQ(n)T(n) \ln[2e/nT(n)] \quad (5-17)$$

The main fact to be noted, however, is that the switching process does depend on  $n$ , the number of walls per unit length. A relation between the demagnetizing field  $H_D$  and the number of walls  $n$  has been shown to exist.

**5.2.4 Calculation of Energy of Partially Switched Configuration.** It is of interest to develop a model that will yield the direction of the magnetization in alternate domains after the partial switch takes place. To do this it is necessary to compute the various terms in the energy expression. The basic configuration is shown in Fig. 5-10.

**5.2.4.1 Basic Relations.** Some of the basic parameters shown in Fig. 5-10 are related to those found in the discussion of the rotational model. The walls are assumed to form perpendicular to the magnetization direction in the  $(\theta + \alpha)$  state before the partial rotation occurs. Thus, from Eq. 5-4, it follows that

$$\cot \psi = [ \tan (\theta + \alpha) ]^{\frac{1}{3}} , \quad (5-18)$$

where  $\psi$  is the acute angle between the domain walls and the average easy axis. With the easy axis dispersion model shown in Fig. 5-6, it follows that  $d$ , the distance between walls, is given by

$$d = D \sin \psi , \quad (5-19)$$

where  $D$  is one-half the easy axis dispersion wavelength. With the magnetization directions in the domains defined as  $\phi_1$  and  $\phi_2$  in the switched and unswitched regions respectively, as shown in Fig. 5-10, the unipolar charge  $\pm Q$  on the walls is given by

$$Q = \pm M [ \cos \phi_1 - \cos \phi_2 ] . \quad (5-20)$$

**5.2.4.2 Wall Energy Calculations.** If  $\phi_1$  is equal to  $\phi_2$  the wall energy could be computed as that of a remanence-type Neel wall<sup>(1)</sup>. In order for the configuration to be stable, the demagnetizing energy must be of the same order of magnitude as other energy terms. Thus, an assumption that  $\phi_1 \approx \phi_2$  appears reasonable. Defining an average remanence angle  $\Phi = (\phi_1 + \phi_2)/2$ , the wall energy,  $E_w$  (per unit length in the easy direction) is approximately (7)

$$E_w = E_n \left( \frac{W}{\sin \psi} \right) \left( \frac{1}{D} \right) (1 - \cos \Phi)^2 , \quad (5-21)$$

where  $E_n$  is the energy per unit wall length of a 180° Neel wall, and  $W$  is the film width in the hard direction.

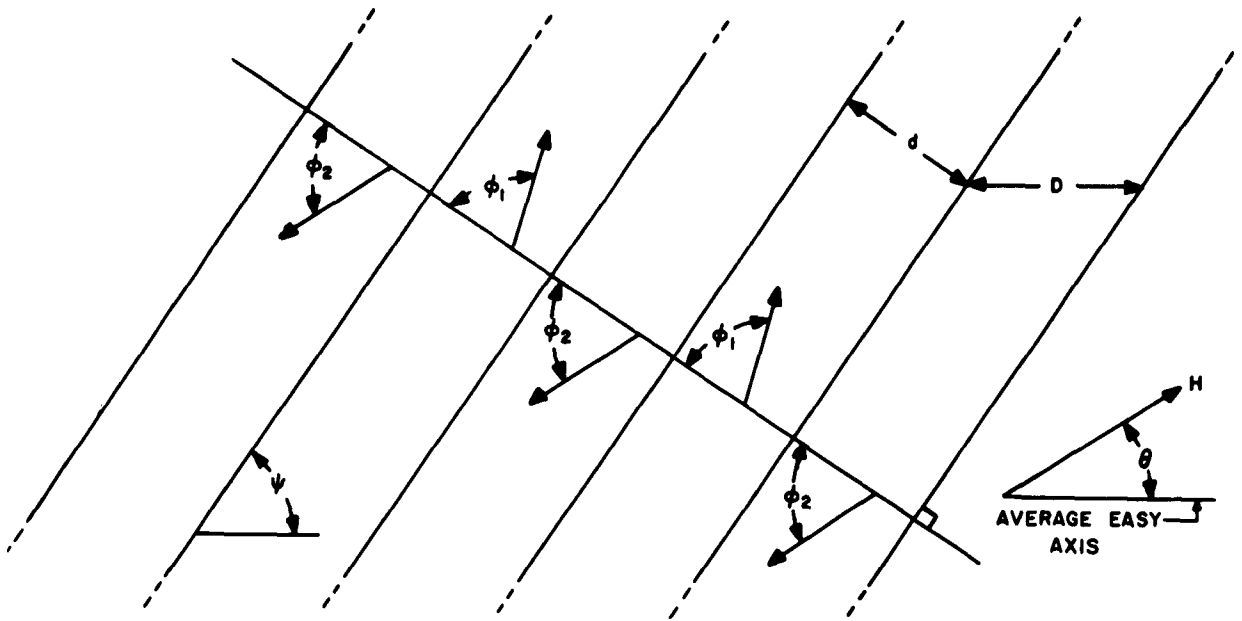


Figure 5-10. Model of Partially Switched Configuration.  
 (Arrows Indicate Magnetization Direction)

### 5.2.4.3 Anisotropy Energy Calculations

a) Switched Regions. The angle,  $\gamma_1$ , between the easy axis and the magnetization in the switched domains is given by

$$\gamma_1 = \phi_1 - \alpha + \frac{\pi}{2} - \psi . \quad (5-22)$$

The anisotropy energy,  $E_{k1}$ , of the switched domains, per unit film length in the easy direction is

$$E_{k1} = KT \left( \frac{W}{\sin \psi} \right) \left( \frac{D \sin \psi}{2D} \right) \sin^2 \gamma_1 . \quad (5-23)$$

b) Unswitched Regions. The angle,  $\gamma_2$ , between the easy axis and the magnetization in the unswitched domains is given by

$$\gamma_2 = -\phi_2 + \alpha + \frac{\pi}{2} - \psi . \quad (5-24)$$

The anisotropy energy,  $E_{k2}$ , of the unswitched domains per unit film length in the easy direction is

$$E_{k2} = KT \left( \frac{W}{\sin \psi} \right) \left( \frac{D \sin \psi}{2D} \right) \sin^2 \gamma_2 . \quad (5-25)$$

5.2.4.4 Demagnetization Energy Calculations. The average demagnetizing field has been calculated previously and is given by Eq. 5-15. In using Eq. 5-15 the values for  $d$  and  $Q$  given by Eqs. 5-19 and 5-20 must be used.

a) Switched Regions. The demagnetization energy,  $E_{D1}$ , in the switched state per unit length of film in the easy direction is given by

$$E_{D1} = -\frac{1}{2} \vec{H}_D \cdot \vec{M}_1 T \left( \frac{W}{\sin \psi} \right) \left( \frac{D \sin \psi}{2D} \right) . \quad (5-26)$$

This may be rewritten as

$$E_{D1} = \frac{1}{4} \vec{H}_D M T W \cos \phi_1 . \quad (5-27)$$

b) Unswitched Regions. The demagnetization energy  $E_{D2}$ , in the unswitched state per unit length of film in the easy direction is given by

$$E_{D2} = -\frac{1}{2} \vec{H}_D \cdot \vec{M}_2 T \left( \frac{W}{\sin \psi} \right) \left( \frac{D \sin \psi}{2D} \right) . \quad (5-28)$$

This may be rewritten as

$$E_{D2} = \frac{1}{4} H_D M T W \cos \phi_2 . \quad (5-29)$$

#### 5.2.4.5 Switching Field Energy Calculations

a) Switching Regions. The angle,  $\delta_1$ , between the applied field and the switched magnetization is given by

$$\delta_1 = \frac{\pi}{2} + \psi - \phi_1 - \theta . \quad (5-30)$$

The energy,  $E_{A1}$ , in the switched domains due to the applied switching field, computed per unit length in the easy direction is

$$E_{A1} = - \vec{H} \cdot \vec{M}_1 T \left( \frac{W}{\sin \psi} \right) \left( \frac{D \sin \psi}{2D} \right) \quad (5-31)$$

This may be rewritten as

$$E_{A1} = - \frac{1}{2} H M T W \cos \delta_1 . \quad (5-32)$$

b) Unswitched Regions. The angle,  $\delta_2$ , between the applied field and the unswitched magnetization is given by

$$\delta_2 = \frac{\pi}{2} + \psi + \phi_2 - \theta . \quad (5-33)$$

The energy,  $E_{A2}$ , in the unswitched domains due to the applied switching field, computed per unit length in the easy direction is

$$E_{A2} = - \vec{H} \cdot \vec{M}_2 T \left( \frac{W}{\sin \psi} \right) \left( \frac{D \sin \psi}{2D} \right) . \quad (5-34)$$

This may be rewritten as

$$E_{A2} = - \frac{1}{2} H M T W \cos \delta_2 . \quad (5-35)$$

5.2.4.6 Summation of Energy Terms. The various terms contributing to the energy of the partially switched configuration are given by Eqs. 5-21, 5-23, 5-25, 5-27, 5-29, 5-32, and 5-35. Summing these terms yields the total energy,  $E_T$ , per unit length in the easy direction as

$$\begin{aligned}
E_T = W \frac{E_n}{D \sin \psi} [ 1 - \cos \frac{1}{2} (\phi_1 + \phi_2) ]^2 & \quad (5-36) \\
+ \frac{1}{2} K T \cos^2 [ \psi + \alpha - \phi_1 ] + \frac{1}{2} K T \cos^2 [ \psi - \alpha + \phi_2 ] \\
+ \frac{M^2 T^2}{D \sin \psi} [ \ln \frac{2eD \sin \psi}{T} ] (\cos \phi_1 - \cos \phi_2)^2 \\
+ \frac{1}{2} H M T \sin ( \psi - \theta - \phi_1 ) + \frac{1}{2} H M T \sin ( \psi - \theta + \phi_2 ).
\end{aligned}$$

The equilibrium magnetization angles  $\phi_1$  and  $\phi_2$  are found by equating  $\partial E_T / \partial \phi_1$  and  $\partial E_T / \partial \phi_2$  simultaneously to zero. If, in addition, it is desired to find the applied field,  $H_f$ , necessary to switch the  $\phi_2$  state rotationally,  $\partial^2 E_T / \partial (\phi_2)^2$  must also be equated to zero. The resulting trio of equations are then simultaneously solved for  $\phi_1$ ,  $\phi_2$ , and  $H_f$ .

## 5.2.5 Deduction of Parameters from Partial Switching Model

### 5.2.5.1 Calculation of Equilibrium Magnetization Angles.

Before proceeding to calculate the various derivatives of Eq. 5-36, it is desirable to simplify its form somewhat. The following substitutions will be used:

$$h = H/M, \quad (5-37a)$$

$$h_k = 2K/M^2 = H_k/M, \quad (5-37b)$$

$$a = (4T/D \sin \psi) \ln \frac{2eD \sin \psi}{T}, \quad (5-37c)$$

$$\epsilon = E_n/M^2 D T \sin \psi, \quad (5-37d)$$

$$\xi_T = E_T/M^2 T W. \quad (5-37e)$$

Note that  $h$ ,  $h_k$ ,  $a$ ,  $\epsilon$ , and  $\xi_T$  are all dimensionless quantities. Substituting Eq. 5-37 in Eq. 5-36 yields

$$\begin{aligned}
2\xi_T = 2\epsilon [ 1 - \cos \frac{1}{2} (\phi_1 + \phi_2) ]^2 + & \quad (5-38) \\
\frac{1}{2} h_k \cos^2 [ \psi + \alpha - \phi_1 ] + \frac{1}{2} h_k \cos^2 [ \psi - \alpha + \phi_2 ] + \\
\frac{1}{2} a [ \cos \phi_1 - \cos \phi_2 ]^2 + \\
h \sin ( \psi - \theta - \phi_1 ) + h \sin ( \psi - \theta + \phi_2 ).
\end{aligned}$$

The pertinent equations can now be found by finding the various derivatives of Eq. 5-38 and equating them to zero. This yields

$$[\partial \xi_T / \partial \phi_1] = 0 ; \quad (5-39a)$$

$$2 \epsilon [1 - \cos \frac{1}{2} (\phi_1 + \phi_2)] \sin \frac{1}{2} (\phi_1 + \phi_2) + \\ \frac{1}{2} h_k \sin 2 [\psi + \alpha - \phi_1] - a [\cos \phi_1 - \cos \phi_2] \sin \phi_1 - \\ h \cos (\psi - \theta - \phi_1) = 0,$$

$$[\partial \xi_T / \partial \phi_2] = 0 ; \quad (5-39b)$$

$$2 \epsilon [1 - \cos \frac{1}{2} (\phi_1 + \phi_2)] \sin \frac{1}{2} (\phi_1 + \phi_2) - \\ \frac{1}{2} h_k \sin 2 [\psi - \alpha + \phi_2] + a [\cos \phi_1 - \cos \phi_2] \sin \phi_2 + \\ h \cos (\psi - \theta + \phi_2) = 0 ,$$

$$[\partial^2 \xi_T / \partial (\phi_2)^2] = 0 ; \quad (5-39c)$$

$$\epsilon [1 - \cos \frac{1}{2} (\phi_1 + \phi_2)] \cos \frac{1}{2} (\phi_1 + \phi_2) + \\ \sin^2 \frac{1}{2} (\phi_1 + \phi_2) - h_k \cos 2 [\psi - \alpha + \phi_2] - h \sin (\psi - \theta + \phi_2) + \\ a [\cos \phi_1 - \cos \phi_2] \cos \phi_2 + \sin^2 \phi_2 = 0 .$$

The simultaneous solution of Eqs. 5-39a, 5-39b, and 5-39c requires the aid of a computing machine. However, the simultaneous solution of Eqs. 5-39a and 5-39b can be found approximately by comparatively simple means. This yields the equilibrium values of  $\phi_1$  and  $\phi_2$  as a function of applied field. To illustrate the procedure used and the type of results obtained, a solution of Eqs. 5-39a and 5-39b will be presented. The following values of the primary film and applied field parameters will be used:

$$\begin{aligned}
T &= 500\text{\AA} & (5-40) \\
E_n &= 30 \times 10^{-6} \text{ erg/cm} \\
D &= 200\mu \\
H_k &= 3 \text{ oe} \\
M &= 700 \text{ e.m.u.} \\
\alpha &= 1^\circ \\
H &= 3 \text{ oe} \\
\theta &= 30^\circ
\end{aligned}$$

From these primary parameters the following secondary quantities can be found:

$$\begin{aligned}
h_r &= H_r/M = 2.2 \times 10^{-3} & (5-41) \\
h_k &= h = 4.3 \times 10^{-3} \\
\psi &= 50^\circ \\
\epsilon &= 0.8 \times 10^{-3} \\
a &= 12.7 \times 10^{-3}
\end{aligned}$$

The method used to solve Eqs. 5-39a and 5-39b is to treat the wall energy as a first order perturbation of the magnetization angles obtained by ignoring the wall energy term. The calculations involved in this process are shown in Table 5-1. The resulting curves are shown in Fig. 5-11. The pair of curves in Fig. 5-11 intersect at three points. These intersections are extrema of Eq. 5-38. Upon substituting the values of  $\phi_1$  and  $\phi_2$  at the extrema into Eq. 5-38 the following is found:

$$\begin{aligned}
\text{a) } \phi_1 &= 62.5^\circ & \xi_T &= 1.90 \times 10^{-3}, & (5-42a) \\
\phi_2 &= 37.5^\circ
\end{aligned}$$

$$\begin{aligned}
\text{b) } \phi_1 &= 73^\circ & \xi_T &= 1.87 \times 10^{-3}, & (5-42b) \\
\phi_2 &= 55^\circ
\end{aligned}$$

$$\begin{aligned}
\text{c) } \phi_1 &= 117^\circ & \xi_T &= 2.50 \times 10^{-3}, & (5-42c) \\
\phi_2 &= 120^\circ
\end{aligned}$$

$$\begin{aligned}
 [ 12.7 \sin \phi_1 ] \cos \phi_2 &= 6.35 \sin 2\phi_1 - 2.15 \sin (100^\circ - 2\phi_1) + 4.3 \cos (20^\circ - \phi) \\
 &- 1.6 [ 1 - \cos \frac{1}{2} (\phi_1 + \phi_2) ] \sin \frac{1}{2} (\phi_1 + \phi_2)
 \end{aligned}
 \tag{5-39a}$$

Let

$$A = 12.7 \sin \phi_1$$

$$B = 6.35 \sin 2\phi_1$$

$$C = -2.15 \sin (100^\circ - 2\phi_1)$$

$$D = 4.3 \cos (20^\circ - \phi_1)$$

$$E = -1.6 [ 1 - \cos \frac{1}{2} (\phi_1 + \phi_2) ] \sin \frac{1}{2} (\phi_1 + \phi_2)$$

$\phi_1$	A	B	C	D	$\frac{B+C+D}{A}$	$(\phi_2)'$	E	$\frac{B+C+D+E}{A}$	$(\phi_2)''$
50°	9.7	6.3	0.0	3.7	1.03	-	-	-	-
60°	11.0	5.5	0.7	3.3	.86	31°	-0.3	.84	33°
70°	12.0	4.1	1.4	2.8	.69	46°	-0.6	.64	50°
80°	12.5	2.2	1.9	2.2	.50	60°	-1.0	.42	65°
90°	12.7	0.0	2.1	1.5	.28	74°	-1.4	.17	80°
100°	12.5	-2.2	2.1	0.7	.05	87°	-1.7	-.09	95°
110°	12.0	-4.1	1.9	0.0	-.18	100°	-2.0	-.35	110°

Table 5-1a. Calculation of  $\phi_2$  for given  $\phi_1$ .

$$[ 12.7 \sin \phi_2 ] \cos \phi_1 = 6.35 \sin 2\phi_2 + 2.15 \sin (100^\circ + 2\phi_2) - 4.3 \cos (20^\circ + \phi_2) - 1.6 [ 1 - \cos \frac{1}{2} (\phi_1 + \phi_2) ] \sin \frac{1}{2} (\phi_1 + \phi_2) \quad (5-39b)$$

Let

$$A = 12.7 \sin \phi_2$$

$$B = 6.35 \sin 2\phi_2$$

$$C = 2.15 \sin (100^\circ + 2\phi_2)$$

$$D = 4.3 \cos (20^\circ + \phi_2)$$

$$E = 1.6 [ 1 - \cos \frac{1}{2} (\phi_1 + \phi_2) ] \sin \frac{1}{2} (\phi_1 + \phi_2)$$

$\phi_2$	A	B	C	D	$\frac{B+C+D}{A}$	$(\phi_1)'$	E	$\frac{B+C+D+E}{A}$	$(\phi_1)''$
30°	6.4	5.5	0.7	-2.8	.53	58°	-0.3	.48	61°
40°	8.2	6.3	0.0	-2.2	.50	60°	-0.4	.45	63°
50°	9.7	6.3	-0.7	-1.5	.42	65°	-0.6	.36	69°
60°	11.0	5.5	-1.4	-0.7	.31	72°	-0.9	.23	77°
70°	12.0	4.1	-1.9	0.0	.18	80°	-1.1	.092	85°
80°	12.5	2.2	-2.1	0.7	.06	87°	-1.4	-.048	93°
90°	12.7	0.0	-2.1	1.5	-.05	93°	-1.6	-.17	100°
100°	12.5	-2.2	-1.9	2.2	-.15	99°	-1.9	-.30	107°
110°	12.0	-4.1	-1.4	2.8	-.22	103°	-2.0	-.39	113°
120°	11.0	-5.5	-0.7	3.3	-.26	105°	-2.0	-.45	117°
130°	9.7	-6.3	0.0	3.7	-.27	106°	-2.1	-.48	119°

Table 5-lb. Calculation of  $\phi_1'$  for given  $\phi_2$ .

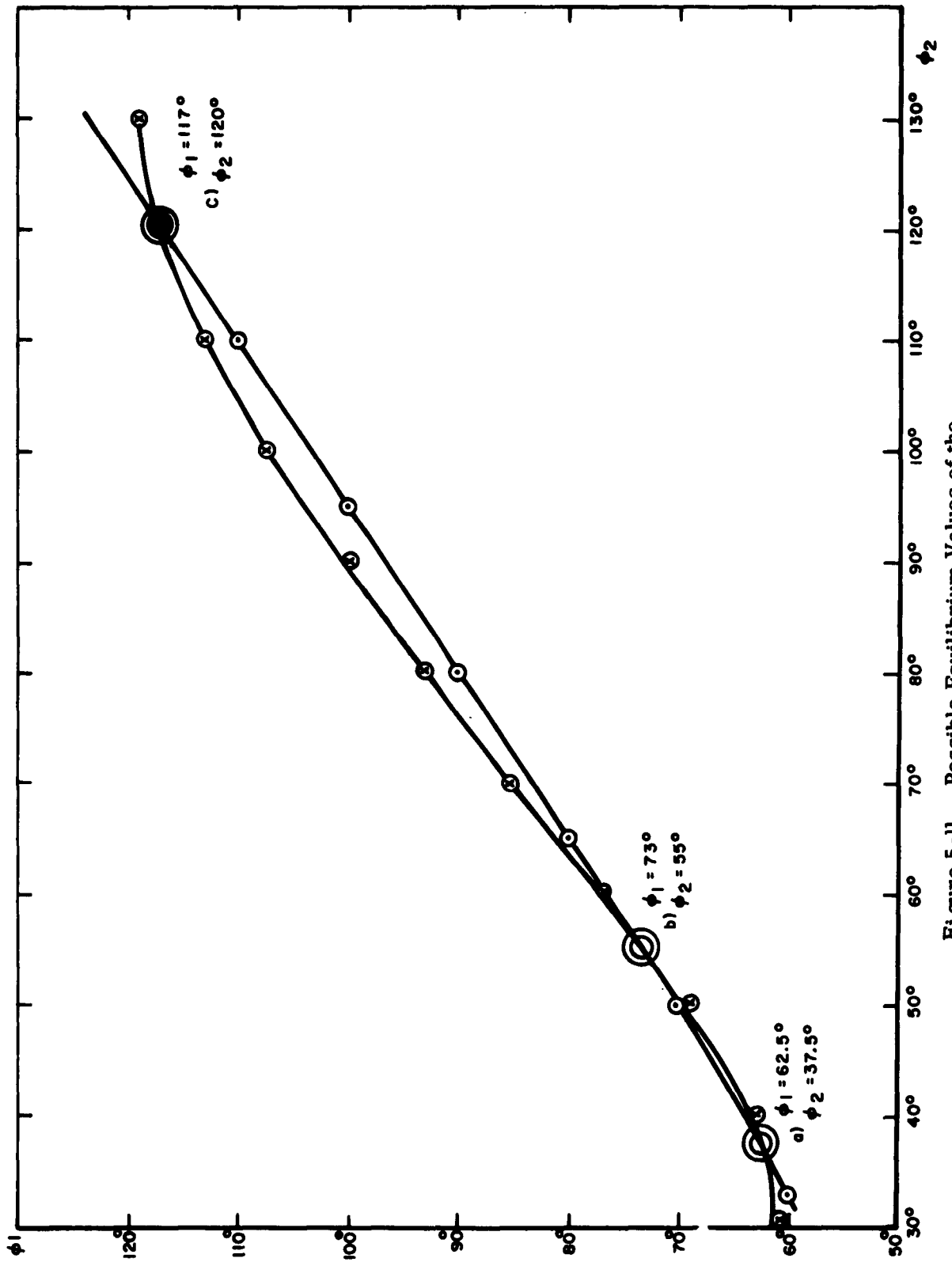


Figure 5-11. Possible Equilibrium Values of the Magnetization Angles,  $\phi_1$  and  $\phi_2$ .

The results shown in Eq. 5-42 indicate that states (a) and (c) are energy maxima while (b) is an energy minimum. The following interpretation may be placed on the above results. State (a) is related to the energy maximum that the switched magnetization went through in achieving the partially switched state. State (b) is the actual state the magnetization now is in for the given film and field parameters of Eq. 5-40. State (c) is related to the energy maximum that would have to be overcome if the magnetization in the  $\phi_2$  state is also to be switched rotationally.

The above discussion and calculations indicate how the partial switching model may be used to calculate the magnetization distribution. It is shown that the proposed model is capable of predicting, on an energy minimization basis, the type of partially switched states seen experimentally.

5.2.5.2 Calculation of Rotational Field  $H_f$  Necessary to Switch  $\phi_2$  State. To show why the  $\phi_2$  state is switched sequentially, it is necessary to compute  $H_f$ , the field necessary to switch the  $\phi_2$  state rotationally, and show that it is greater than the field necessary for sequential switching. The general solution of Eq. 5-39 for  $H_f$  requires the use of a computing machine as stated earlier. However, by assuming that the switched magnetization state,  $\phi_1$ , is parallel to the applied field when a rotational switch of state  $\phi_2$  occurs, an initial approximate solution may be obtained. This solution in turn allows further approximate solutions to be found. Using the parameters of Eq. 5-40 and setting  $\phi_1 = 110^\circ$  in Eq. 5-39a leaves

$$1.6 [1 - \cos (55^\circ + \frac{1}{2} \phi_2)] \sin (55^\circ + \frac{1}{2} \phi_2) + \quad (5-43)$$

$$12.0 \cos \phi_2 = -2.22 .$$

Using perturbation methods up to second order, the solution of Eq. 5-43 is  $\phi_2 = 111^\circ$ . Setting  $\phi_1 = 110^\circ$  and  $\phi_2 = 111^\circ$  in Eqs. 5-39b and 5-39c yields  $h_f = 5.5 \times 10^{-3}$  and  $h_f = 10.7 \times 10^{-3}$  respectively.

Repeating the above process by setting  $\phi_1 = 100^\circ$  and  $h_f = 8.1 \times 10^{-3}$  (obtained by averaging the first pair of values) in Eq. 5-39a yields  $\phi_2 = 91^\circ$ . This in turn gives  $h_f = 7.8 \times 10^{-3}$ , and  $h_f = 13.6 \times 10^{-3}$  from Eqs. 5-39b and 5-39c respectively.

Setting  $\phi_1 = 95^\circ$  and  $\phi_2 = 85^\circ$  in Eq. (39) yields  $h_f = 23.3 \times 10^{-3}$ ,  $11.0 \times 10^{-3}$  and  $14.6 \times 10^{-3}$  from Eqs. 5-39a, 5-39b, and 5-39c respectively.

It seems from the above calculations that a value of  $h_f$  of about  $13 \times 10^{-3}$  is not unreasonable. In other words  $H_f \approx 3 H_K$  for the given film and applied field parameters. However,  $H_w$ , the wall motion coercive force, is generally less than  $1.5 H_K$ . Thus it is reasonable to expect that the final switching of the  $\phi_2$  state will be a sequential, rather than a rotational, process.

**5.2.6 The Sequential Switching Process.** As stated in the previous section, the  $\phi_2$  state will be switched sequentially. The model of the sequential switching process will be broken into two distinct types, although the actual switching may be a combination of both. The two types are: (1) nucleation and motion of a domain wall in the easy direction; and (2) motion of wall pairs such as to shrink the  $\phi_2$  domains and enlarge the  $\phi_1$  domains.

To show theoretically which of the sequential processes is energetically preferred as a function of switching field magnitude and angle is a problem of major proportions. To reach even tentative conclusions, it will be necessary to make assumptions that greatly simplify the problem.

The simplest assumption to make is that the coercive force necessary to move either an easy direction wall or the walls created by the partial switching process depends only on the angle between the wall and the switching field. That is, the wall motion field  $H_w$  is assumed to be given by

$$H_w = H_c / \cos \phi , \quad (5-44)$$

where  $H_c$  is the coercive force when the wall and field directions are parallel, and  $\phi$  is the angle between the field and the wall. It will be assumed that  $H_c$  is a constant independent of the wall type under consideration. For a wall in the easy direction,  $\phi$  is equal to  $\theta$ . For the walls of the partially switched state  $\phi$  is equal to  $(\psi - \theta)$ . The curves of  $\psi$  vs  $\theta$  and  $(\psi - \theta)$  vs  $\theta$  are obtained from Eq. 5-18 and are plotted in Fig. 5-12. It is assumed that  $\alpha$  is negligible compared to  $\theta$  for  $\theta > \theta_c$ , the minimum field angle at which partial switching can occur.

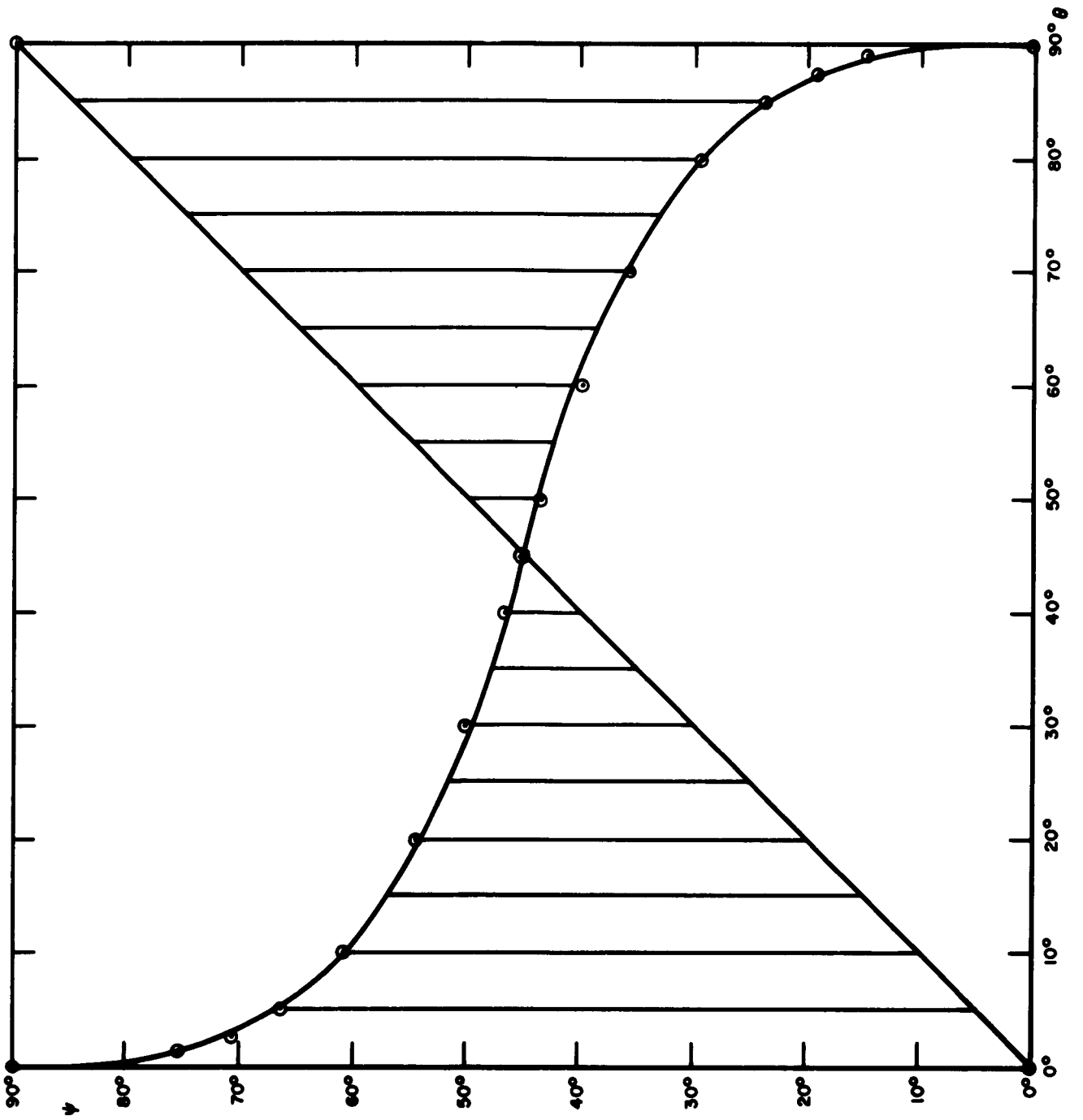


Figure 5-12. Partially Switched Wall Angle,  $\psi$ , vs. Applied Field Angle  $\theta$  Also ( $\psi - \theta$ ) vs.  $\theta$ .

In order to completely switch the  $\phi_2$  state sequentially, the applied field must be increased by an amount  $\Delta H_w$  over the initial field value  $H_w$  at which wall motion will occur.

The angular dependence of  $\Delta H_w$  will be assumed to be somewhat different than that of  $H_w$ . This is to take into account the experimental fact that  $\Delta H_w$  is greater for walls inclined to the easy axis even if the applied field is parallel to the wall in both cases. This dependence on the angle between the field and the easy axis is taken into account theoretically by assuming that

$$\Delta H_w = \Delta H_c / \cos \theta . \quad (5-45)$$

Here  $\Delta H_c$  is the additional field necessary to complete the sequential switching process when both the applied field and the domain wall are in the easy direction. It will be further assumed, for definiteness, that  $\Delta H_c = H_c/3$ .

The curves of Eqs. 5-44 and 5-45 are shown in Fig. 5-13. From Fig. 5-13, the following conclusions may be drawn:

- a) For  $\theta < 15^\circ$ , the sequential process is that of easy direction domain wall motion (if it is assumed that  $\theta_c < 15^\circ$  this also takes in the case of no partial switching).
- b) For  $15^\circ < \theta < 25^\circ$ , the process is that of easy direction wall motion, followed by and concurrent with motion of the partial switching walls.
- c) For  $25^\circ < \theta < 50^\circ$ , the process is that of motion of the partial switching walls, followed by and concurrent with motion of an easy direction wall.
- d) For  $\theta > 50^\circ$  the process consists entirely of motion of the partial switching walls.

It should be emphasized here that the above conclusions are subject of two previous conclusions, i.e., no partially switched state occurs until  $H_T < H_w$  (i.e.  $\theta > \theta_c$ ), and the switching process may be completely rotational for  $\theta > 45^\circ$  in certain cases.

This concludes the theoretical analysis of the partial switching process and subsequent sequential process. The next section will present experimental evidence of the types of switching processes under discussion.

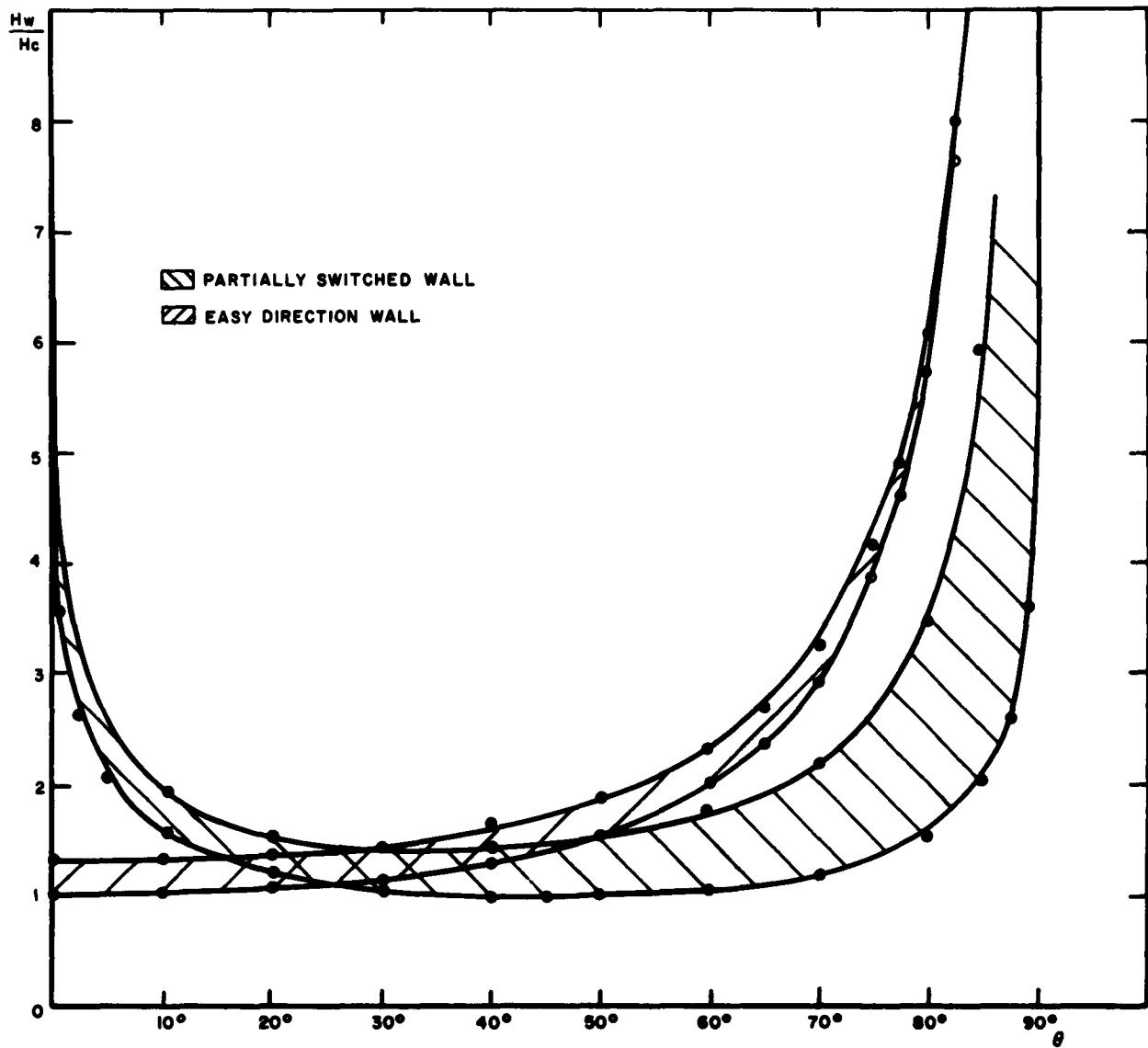


Figure 5-13. Theoretical Wall Motion Coercive Forces of Partially Switched and Easy Direction Walls vs. Applied Field Angle.

### 5.3 Experimental

Experimental data on films exhibiting partial switching was taken using two techniques. These were (1) examination of the switching output signal in a hysteresis curve tracer<sup>(8)</sup>, and (2) examination of domain walls produced during switching using Bitter solution to outline the walls.

5.3.1 Analysis of Switching Signal Data. In a hysteresis curve tracer the electrical output signal is proportional to the time rate of change of the flux. The conventional hysteresis loop is obtained by integrating this output signal.

It has been found that the partial switching phenomena can be best analyzed by presenting the output signal directly rather than its integral. Examples of the type of data taken are shown in Figs. 5-14 through 5-17 for various specimens and applied field angles.

The data presented in Fig. 5-14 confirms many of the ideas discussed theoretically. The film on which this data was taken has a thickness of  $300\text{\AA}$ , an  $H_C$  of 4.1 oe, and an  $H_K = 4.0$  oe. As Fig. 5-14b shows, the partial switching mode is clearly distinguishable at an applied field angle of  $15^\circ$ . This is to be expected for an inverted film where  $\theta_C = 0$ . The three switching signal peaks in Fig. 5-14b and Fig. 5-14c are (for increasing H) due to partial rotation, motion of paired partial rotation walls, and motion of easy direction wall.

Evidence confirming this order of events will be discussed in the next section. For this film, the switching mechanism becomes a purely rotational one for  $\theta = 45^\circ$ . This is shown in Fig. 5-14d. This type of behavior is accounted for theoretically by assuming that the number of walls/unit length of the partially switched state is relatively low. This point will be discussed more fully after additional data is presented.

The switching signal output of another film is shown in Fig. 5-15. Here  $H_K = 4.0$  oe,  $H_C = 3.6$  oe, and  $T = 360\text{\AA}$ . Since this specimen is not inverted,  $\theta_C \neq 0$ . A comparison of Figs. 5-14b and 5-15b illustrates this fact. Both of these output signals are taken at  $\theta = 15^\circ$ . Note that the distance between the rotational and sequential peaks in Fig. 5-14b is greater than the corresponding distance in Fig. 5-15b. This is what would be expected theoretically, as  $H_C/H_K = 1.0$  for the specimen of Fig. 5-14 and  $H_C/H_K = 0.9$  for the specimen of Fig. 5-15.

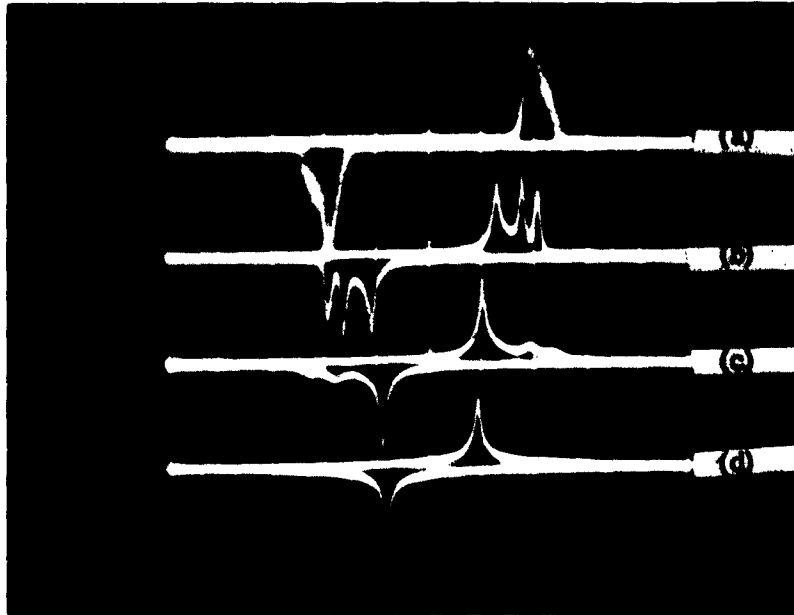


Figure 5-14. Switching Signal Output of Specimen for Various Applied Field Angles. (Hor. Scale: One Div. = Two oe.)  $H_C = 4.1$  oe,  $H_K = 4.0$  oe,  $T = 300\text{\AA}$ .

- (a)  $\theta = 0^\circ$  (easy axis)
- (b)  $\theta = 15^\circ$
- (c)  $\theta = 30^\circ$
- (d)  $\theta = 45^\circ$

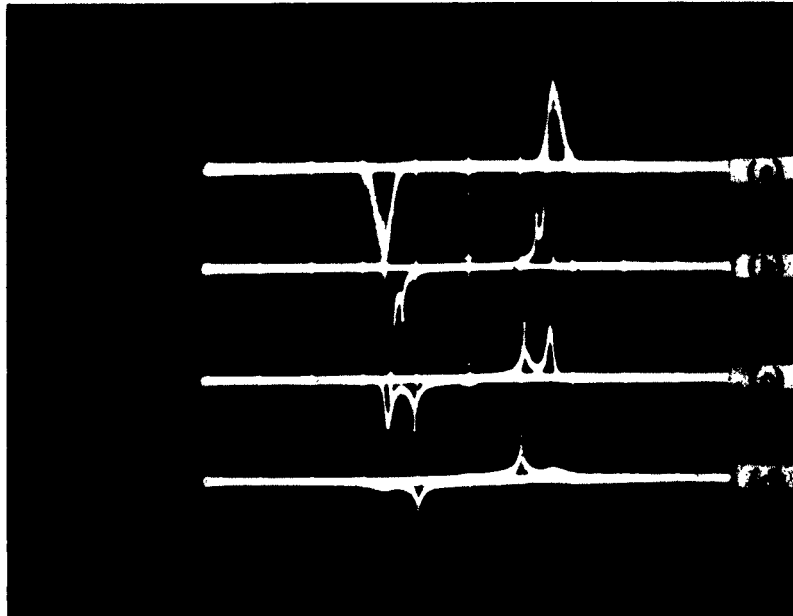


Figure 5-15. Switching Signal Output of Specimen for Various Applied Field Angles. (Hor. Scale: One Div. = One oe.)  $H_C = 3.6$  oe,  $H_K = 4.0$  oe,  $T = 360\text{\AA}$ .

- (a)  $\theta = 0^\circ$  (easy axis)
- (b)  $\theta = 15^\circ$
- (c)  $\theta = 30^\circ$
- (d)  $\theta = 45^\circ$

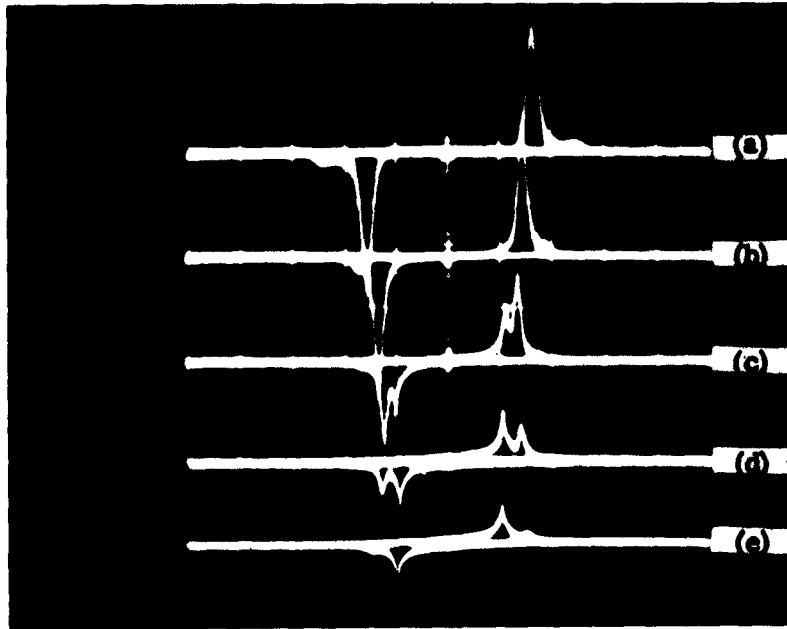


Figure 5-16. Switching Signal Output of Specimen for Various Applied Field Angles. (Hor. Scale: One Div. = Two oe.),  $H_C = 3.0$  oe,  $H_K = 3.4$  oe,  $T = 600\text{\AA}$ .

- (a)  $\theta = 0^\circ$  (easy axis)
- (b)  $\theta = 15^\circ$
- (c)  $\theta = 30^\circ$
- (d)  $\theta = 45^\circ$
- (e)  $\theta = 55^\circ$

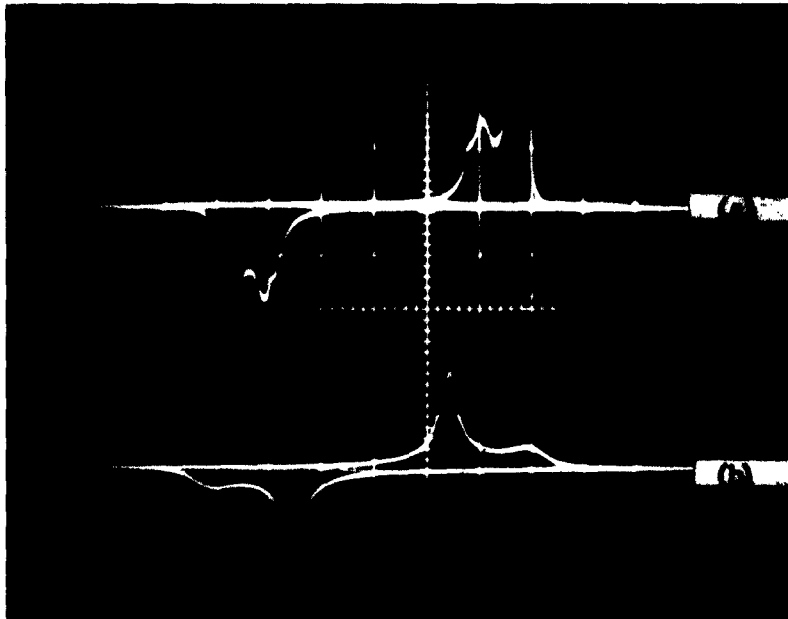


Figure 5-17. Switching Signal Output of Specimen for Various Applied Field Angles. (Hor. Scale: One Div. = One oe.)  
(a)  $\theta = 13^\circ$   
(b)  $\theta = 31^\circ$

Another point to note is that the output signal of Fig. 5-14d, taken at  $\theta = 45^\circ$ , is not quite purely rotational. This would indicate that the number of walls/unit length of the partially switched state increases as  $T$  increases from  $300\text{\AA}$  to  $360\text{\AA}$ .

To further test the hypothesis that the number of walls/unit length of the partially switched state increases with film thickness, the data of Fig. 5-16 was taken. Here  $H_k = 3.4$  oe,  $H_c = 3.1$  oe, and  $T = 600\text{\AA}$ . Here it is found that the switching does not become a rotational one until  $\theta = 60^\circ$ . This again indicates an increase of walls/unit length with film thickness. Further data taken on films of  $900 - 1000\text{\AA}$  showed a rotational-sequential switching pattern until an angle of  $70^\circ - 80^\circ$  was reached. From this data and the theoretical model presented, it appears that the number of walls/unit length of the partially switched state is an increasing function of film thickness.

While Fig. 5-14 shows rather clearly that the sequential switch involves two processes, the same conclusion cannot be drawn from Figs. 5-15 or 5-16. This can be accounted for by theorizing that the coercive forces associated with partially switched and easy direction wall motion are so nearly equal that their output signals merge into one. Another possibility is that the merging is between the rotational signal and the partially switched wall motion signal.

This latter possibility is shown in Fig. 5-17a, taken at  $\theta = 13^\circ$ . Close examination of this signal shows that the sequential signal of lower coercive force is almost indistinguishable from the rotational output signal. In Fig. 5-17b, taken at  $\theta = 31^\circ$ , the switching process seems to consist of a partial rotational followed by only one type of sequential process. This is in qualitative agreement with the theoretical ideas presented in Section 5.2.6.

It might be noted here that all films on which data is presented in this section and the one following were vacuum deposited from a melt composition of 80% Ni/ 17% Fe/ 3% Co in the form of strips 1" long and 1/8" wide. By the use of external magnetic films the films were deposited such as to have their easy axis in the short direction.

**5.3.2 Analysis of Bitter Patterns:** A clear picture of the switching processes under discussion may be seen by observing the formation and motion of domain walls by the use of Bitter or powder pattern techniques.

An example of the partially switched state is shown in Fig. 5-18 as observed by dark-field microscopy. The specimen of Fig. 5-18 is the same as that of Fig. 5-14. When the applied field magnitude is further increased the walls move as shown in Fig. 5-19. Another example of wall pairing in another specimen is shown in Fig. 5-20 as observed by phase-contrast microscopy. A further increase in applied field causes the formation and motion of an easy direction wall which completes the switching process; this easy-direction wall motion process is shown in Fig. 5-21 for another specimen.

The processes illustrated by Figs. 5-18 through 5-21 are consistent with the theoretical process and the interpretation drawn from the switching signal data of Figs. 5-14 through 5-17.

#### 5.4 Conclusions

For many films the switching process cannot be classified simply as a rotational or wall motion process. This fact is especially apparent when the switching process is observed as a function of the angle between the applied field and the easy axis.

A theoretical model was presented that shows the initial switching process to be a partial rotation of alternate regions of the film. This partially rotated state is "locked-in", as far as further rotational switching is concerned, until the applied field magnitude is greatly increased. The switching is completed, therefore, by a sequential, or wall motion, process. This process may consist of motion of the partially switched walls, or nucleation and motion of an easy direction wall. In certain cases, both sequential processes may occur.



**Figure 5-18. Example of the Partially Switched State, Dark Field Illumination. (Mag. = 180 X)**



**Figure 5-19. Example of Motion of Paired Partially Switched Walls, Dark Field Illumination. (Mag. = 180 X)**



Figure 5-20. Example of Motion of Paired Partially Switched Walls, Phase Contrast Illumination. (Mag. = 150 X)



**Figure 5-21. Example of Easy Direction Wall Motion, Dark Field Illumination. (Mag. = 115 X)**

## APPENDIX

In certain cases, it may be of interest to calculate the energy of the partially-switched state after some motion of the partially-switched walls has taken place. For this case, the configuration is shown in Fig. 5-22. The result given for the infinite sheet-of-charge case in Eq. 5-6 still applies, but a new result analagous to Eq. 11 is necessary.

For one line of charge, the result is given by Eq. 5-7 as

$$H_1 = 2QT/r . \quad (5-A1)$$

Summing over all the charged wall yields

$$H_f = 2QT \sum_{k=-\infty}^{k=+\infty} \frac{1}{2kd+r} - \frac{1}{2kd+(a+r)} . \quad (5-A2)$$

Using the method of residues<sup>(6)</sup> which states that

$$\sum_{k=-\infty}^{+\infty} f(k) = - \sum \text{Res} [ \pi f(z) \cot \pi z ] , \quad (5-A3)$$

where the second sum is over the poles of  $f(z)$ , Eq. 5-A2 becomes

$$H_f = \frac{\pi QT}{d} \left[ \cot \frac{\pi r}{2d} - \cot \frac{\pi (a+r)}{2d} \right] . \quad (5-A4)$$

With suitable trigonometric manipulation, Eq. 5-A4 becomes

$$H_f = \frac{\pi QT}{d} \frac{1}{\sin \frac{\pi r}{d} + 2 \sin \frac{2\pi r}{2d} \cot \frac{\pi a}{2d}} . \quad (5-A5)$$

The modification of the partially-rotated state due to motion of the partially switched walls can be taken into account theoretically by substituting Eq. 5-A5 for Eq. 5-11. Other slight changes to take the now unequal widths of the switched and unswitched states into account in calculating anisotropy and magnetization energy terms are straightforward. All calculations are analagous to those given in the text.

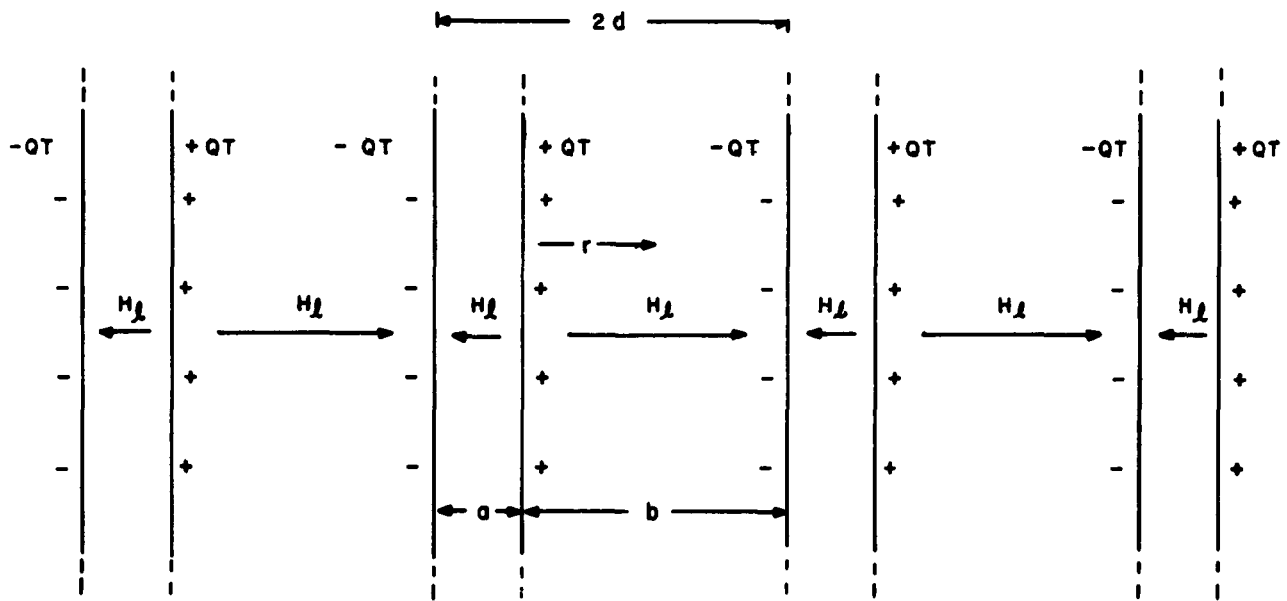


Figure 5-22. Model for Calculation of Field of Infinite, Alternately Charged, Paired Lines of Charge.

### Bibliography

1. R. J. Spain and H. Rubinstein, J. Appl. Phys. 32, 288 (1961).
2. R.J. Spain, Proc. Inter. Conf. on Magnetism and Crystallography at Kyoto, Japan (1961), to be published.
3. S. Methfessel, S. Middlehoek, and H. Thomas, J. Appl. Phys. 32, 1959 (1961).
4. E. C. Stone and E. P. Wohlfarth, Phil. Trans. Roy. Soc. (London) A240 599(1948).
5. D. O. Smith, J. Appl. Phys. 29, 264 (1958).
6. P. M. Morse and H. Feshbach "Methods of Theoretical Physics" (McGraw - Hill, New York 1953) pg. 413-414.
7. LFE Annual Report #570-A2, pg. 58-59.
8. Ibid pg. 24-39.

LIST OF RECIPIENTS FOR #048137

- 001 Assistant Sec. of Def. for Res. and Eng.  
Information Office Library Branch  
Pentagon Building  
Washington 25, D.C.
- 002 Armed Services Technical Information Agency  
Arlington Hall Station  
Arlington 12, Virginia
- 003 Chief of Naval Research  
Department of the Navy  
Washington 25, D.C.  
Attn: Code 437, Information Systems Branch
- 004 Chief of Naval Operations  
OP-07T-12  
Navy Department  
Washington 25, D.C.
- 005 Director, Naval Research Laboratory  
Technical Information Officer/Code 2000  
Washington 25, D.C.
- 006 Commanding Officer, Office of Naval Research  
Navy #100, Fleet Post Office  
New York, New York
- 007 Commanding Officer, ONR Branch Office  
346 Broadway  
New York 13, New York
- 008 Commanding Officer, ONR Branch Office  
495 Summer Street  
Boston 10, Massachusetts
- 010 Bureau of Ships  
Department of the Navy  
Washington 25, D.C.  
Attn: Code 607A NTDS

- 011 Bureau of Naval Weapons  
Department of the Navy  
Washington 25, D. C.  
Attn: RAAV Avionics Division
- 012 Bureau of Naval Weapons  
Department of the Navy  
Washington 25, D. C.  
Attn: RMWC Missile Weapons Control Div.
- 013 Bureau of Naval Weapons  
Department of the Navy  
Washington 25, D. C.  
Attn: RUDC ASW Detection & Control Div.
- 016 Bureau of Ships  
Department of the Navy  
Washington 25, D. C.  
Attn: Communications Branch Code 686
- 019 Naval Ordnance Laboratory  
White Oaks  
Silver Spring 19, Maryland  
Attn: Technical Library
- 020 David Taylor Model Basin  
Washington 7, D. C.  
Attn: Technical Library
- 022 Naval Electronics Laboratory  
San Diego 52, California  
Attn: Technical Library
- 024 University of Illinois  
Control Systems Laboratory  
Urbana, Illinois  
Attn: D. Alpert
- 025 University of Illinois  
Digital Computer Laboratory  
Urbana, Illinois  
Attn: Dr. J. E. Robertson

- 027 Air Force Cambridge Research Laboratories  
Laurence C. Hanscom Field  
Bedford, Massachusetts  
Attn: Research Library, CRX2-R
- 028 Technical Information Officer  
U. S. Army Signal Research & Dev. Lab.  
Fort Monmouth, New Jersey  
Attn: Data Equipment Branch
- 031 National Security Agency  
Fort George G. Meade, Maryland  
Attn: R-4, Howard Campaigne
- 032 U. S. Naval Weapons Laboratory  
Dahlgren, Virginia  
Attn: Head, Computation Div., G. H. Gleissner
- 033 National Bureau of Standards  
Data Processing Systems Division  
Room 239, Bldg. 10  
Attn: A. K. Smilow  
Washington 25, D. C.
- 034 Aberdeen Proving Ground, BRL  
Aberdeen Proving Ground, Maryland  
Attn: J. H. Giese, Chief Computation Lab.
- 053 Commanding Officer  
ONR Branch Office  
John Crerar Library Bldg.  
86 East Randolph Street  
Chicago 1, Illinois
- 054 Commanding Officer  
ONR Branch Office  
1030 E. Green Street  
Pasadena, California
- 055 Commanding Officer  
ONR Branch Office  
1000 Geary Street  
San Francisco 9, California

- 057 National Bureau of Standards  
Washington 25, D.C.  
Attn: Mr. R. D. Elbourn
- 058 Naval Ordnance Laboratory  
Corona, California  
Attn: H. H. Weider
- 059 George Washington University  
Washington, D.C.  
Attn: Prof. N. Grisamore
- 062 New York University  
Washington Square  
New York 3, New York  
Attn: Dr. H. Kallmann
- 069 Lockheed Missiles and Space Company  
3251 Hanover Street  
Palo Alto, California  
Attn: W. F. Main
- 070 Lockheed Research Laboratory  
3251 Hanover, 52-40, Bldg. 202  
Palo Alto, California  
Attn: M. E. Browne
- 081 Stanford University  
Stanford, California  
Attn: Electronics Lab., Prof. John G. Linvill
- 091 University of California - LA  
Los Angeles 24, California  
Attn: Dept. of Engineering, Prof. Gerald Estrin
- 092 University of Maryland  
Physics Department  
College Park, Maryland  
Attn: Prof. R. E. Glover
- 093 Columbia University  
New York 27, New York  
Attn: Dept. of Physics, Prof. L. Brillouin

- 101 Naval Research Laboratory  
Washington 25, D. C.  
Attn: Security Systems  
Code 5266, Mr. G. Abraham
- 118 National Physical Laboratory  
Teddington, Middlesex  
England  
Attn: Dr. A. M. Uttley, Superintendent,  
Autonomics Division
- 133 Diamond Ordnance Fuze Laboratory  
Connecticut Ave. & Van Ness Street  
Washington 25, D. C.  
ORDTL-012, E. W. Channel
- 136 Westinghouse Electric Research Laboratories  
Beulah Road, Churchill Boro.  
Pittsburgh 35, Pennsylvania  
Attn: Magnetics and Solid State Department, G. Shirane
- 139 Harvard University  
Cambridge, Massachusetts  
Attn: School of Applied Science, Dean Harvey Brook
- 146 Wright Air Development Division  
Electronic Technology Laboratory  
Wright-Patterson AFB, Ohio  
Attn: Lt. Col. L. M. Butsch, Jr. ASRUEB
- 148 Laboratory For Electronics, Inc.  
1079 Commonwealth Avenue  
Boston 15, Massachusetts  
Attn: Dr. H. W. Fuller
- 149 Standord Research Institute  
Computer Laboratory  
Menlo Park, California  
Attn: H. D. Crane
- 151 General Electric Company  
Schnectady 5, New York  
Attn: Library, L. M. E. Dept., Bldg. 28-501

- 152 The Rand Corp.  
1700 Main Street  
Santa Monica, California  
Attn: Numerical Analysis Dept., Willis H. Ware
- 175 Stanford Research Institute  
Menlo Park, California  
Attn: Dr. Charles Rosen, Applied Physics Lab.
- 180 Director, USAF Project R A N D  
Via U. S. Air Force Liaison Office  
The Rand Corporation  
1700 Main Street  
Santa Monica, California
- 189 Transitron Electronic Corporation  
168-182 Albion Street  
Wakefield, Massachusetts  
Attn: Dr. H. G. Rudenberg, Director R & D
- 192 Texas Technological College  
Lubbock, Texas  
Attn: Paul G. Griffith, Dept. of Electrical Engineering
- 197 L. G. Hanscom Field/AF-CRL-CRRB  
Bedford, Massachusetts  
Attn: Dr. H. H. Zschirnt
- 202 Department of the Army  
Office of the Chief of Research & Development  
Pentagon, Room 3D442  
Washington 25, D. C.  
Attn: Mr. L. H. Geiger
- 233 General Electric Research Lab.  
P. O. Box 1088  
Schenectady, New York  
Attn: V. L. Newhouse, Applied Physics Section
- 234 The George Washington University  
Logistics Research Project  
707 22nd Street, N. W.  
Washington 7, D. C.  
Attn: Joseph Fennell

- 238 Harshaw Chemical Company  
1945 East 97th Street  
Cleveland 6, Ohio  
Attn: Mr. A. E. Middleton
- 295 University of Pennsylvania  
Moore School of Electrical Engineering  
200 South 33rd Street  
Philadelphia 4, Pennsylvania  
Attn: Miss Anna Louise Campion
- 331 Applied Physics Laboratory  
John Hopkins University  
8621 Georgia Avenue  
Silver Spring, Maryland  
Attn: Document Library
- 333 Bureau of Supplies and Accounts, Chief  
Navy Department  
Washington, D. C.  
Attn: Code W3
- 339 U. S. Naval Avionics Facility  
Indianapolis 18, Indiana  
Attn: Librarian, Code 031.2
- 341 Prof. E. L. Hahn  
Department of Physics  
University of California  
Berkeley 4, California
- 343 Auerbach Electronics Corporation  
1634 Arch Street  
Philadelphia 3, Pennsylvania
- 344 National Aeronautics & Space Administration  
Goddard Space Flight Center  
Greenbelt, Maryland  
Attn: Chief, Data Systems Div., C. V. L. Smith
- 351 Federal Aviation Agency  
Bureau of Research and Development  
Washington, 25, D. C.  
Attn: RD-375 Mr. Harry Hayman

- 352 **Commanding Officer**  
**U. S. Army Signal Research & Development Lab.**  
**Fort Monmouth, New Jersey**  
**Attn: SIGFM/EL/PEP/R. A. Gerhold**
- 353 **Commander Rome Air Development Center**  
**Griffis Air Force Base**  
**New York**  
**Attn: RCLMA/J. Dove**
- 354 **McDonnell Aircraft Corporation**  
**Missile Engineering Division**  
**Municipal Airport**  
**St. Louis, Missouri**  
**Attn: Manager, Adv. Digital Techniques, R. E. Acker**
- 366 **Chief, Bureau of Ships**  
**Code 671A2**  
**Washington, D. C.**  
**Attn: LCDR. E. B. Mahinske, USN**
- 373 **Lincoln Laboratory**  
**Massachusetts Institute of Technology**  
**Lexington 73, Massachusetts**  
**Attn: Library**
- 536 **Institute for Defense Analysis**  
**Communications Research Division**  
**Von Neumann Hall**  
**Princeton, New Jersey**